Context-dependent regulatory variants in Alzheimer's disease

Authors

Ziheng Chen[1,2,3], Yaxuan Liu[2,3], Ashley R. Brown[2,3], Heather H. Sestili[2,3], Easwaran Ramamurthy[2,3], Xushen Xiong[4,5†], Dmitry Prokopenko[6,7], BaDoi N. Phan[2,3], Lahari Gadey[2,3], Peinan Hu[8], Li-Huei Tsai[4,9,10], Lars Bertram[11,12], Winston Hide[6,13], Rudolph E. Tanzi[6,7], Manolis Kellis[4,5], Andreas R. Pfenning[2,3*]

Affiliations

1 Department of Biological Sciences, Carnegie Mellon University, Pittsburgh, PA 15213, USA
2 Computational Biology Department, Carnegie Mellon University, Pittsburgh, PA 15213, USA
3 Neuroscience Institute, Carnegie Mellon University, Pittsburgh, PA 15213, USA
4 Broad Institute of MIT and Harvard, Cambridge, MA 02142, USA
5 Computer Science and Artificial Intelligence Laboratory, Massachusetts Institute of Technology, Cambridge, MA 02139, USA
6 Harvard Medical School, Boston, MA 02115, USA
7 Genetics and Aging Research Unit, The Henry and Allison McCance Center for Brain Health, Department of Neurology, Massachusetts General Hospital, Boston, MA 02114, USA
8 Department of Genetics and Genome Sciences, School of Medicine, Case Western Reserve University, Cleveland, OH 44106, USA
9 Picower Institute for Learning and Memory, Massachusetts Institute of Technology, Cambridge, MA 02139, USA
10 Department of Brain and Cognitive Sciences, Massachusetts Institute of Technology, Cambridge, MA 02139, USA
11 Lübeck Interdisciplinary Platform for Genome Analytics, Institutes of Neurogenetics and Cardiogenetics, University of Lübeck, Lübeck, Germany
12 Department of Psychology, University of Oslo, Oslo, Norway
13 Department of Pathology, Beth Israel Deaconess Medical Center, Boston, MA 02215, USA
† Present address: The Second Affiliated Hospital & Liangzhu Laboratory, Zhejiang University School of Medicine, Hangzhou 311121, China
* Correspondence: apfenning@cmu.edu

Abstract

Noncoding genetic variants underlie many complex diseases, yet identifying and interpreting their functional impacts remains challenging. Late-onset Alzheimer's disease (LOAD), a polygenic neurodegenerative disorder, exemplifies this challenge. The disease is strongly associated with noncoding variation, including common variants enriched in microglial enhancers and rare variants that are hypothesized to influence neurodevelopment and synaptic plasticity. These variants often perturb regulatory sequences by disrupting transcription factor (TF) motifs or altering local TF interactions, thereby reshaping gene expression and chromatin accessibility. However, assessing their impact is complicated by the context-dependent functions of regulatory sequences,

underscoring the need to systematically examine variant effects across diverse tissues, cell types, and cellular states.

Here, we combined *in vitro* and *in vivo* massively parallel reporter assays (MPRAs) with interpretable machine-learning models to systematically characterize common and rare variants across myeloid and neural contexts. Parallel profiling of variants in four immune states *in vitro* and three mouse brain regions *in vivo* revealed that individual variants can differentially and even oppositely modulate regulatory function depending on cell-type and cell-state contexts. Common variants associated with LOAD tended to exert stronger effects in immune contexts, whereas rare variants showed more pronounced impacts in brain contexts. Interpretable sequence-to-function deep-learning models elucidated how genetic variation leads to cell-type-specific differences in regulatory activity, pinpointing both direct transcription-factor motif disruptions and subtler tuning of motif context. To probe the broader functional consequences of a locus prioritized by our reporter assays and models, we used CRISPR interference to silence an enhancer within the *SEC63-OSTM1* locus that harbors four functional rare variants, revealing its gatekeeper role in inflammation and amyloidogenesis. These findings underscore the context-dependent nature of noncoding variant effects in LOAD and provide a generalizable framework for the mechanistic interpretation of risk alleles in complex diseases.

Main

Late-onset Alzheimer's disease (LOAD), the most prevalent neurodegenerative disorder worldwide, exhibits strong heritability[1]. Its genetic architecture comprises multiple components, including the strong influence of the *APOE* ε4 allele[2], common variants with weaker effects, and rare variants. Genome-wide association studies (GWAS)[3–6] have identified numerous common variants (minor allele frequency (MAF) ≥ 0.01) that are enriched for functions in immune cells, particularly microglia and macrophages. This genetic landscape implicates neuroinflammation and mirrors the broad observed failure of microglial functions in LOAD brains[7,8]: impaired surveillance[9,10], reduced amyloid-β[11,12] and tau clearance[13,14], dysregulated injury response[15,16], and altered inflammatory regulation[17,18]. Notably, top risk genes such as *BIN1* and *TREM2* encode proteins crucial for maintaining myeloid homeostasis; dysfunction in these genes perturbs processes like endocytosis[19,20], lipid metabolism[19,21], and cytokine signaling[19,22], thereby accelerating neurodegeneration[23,24]. Human single-nucleus transcriptomic studies further delineate distinct microglial activation states, and several of these states display more prominent LOAD-associated gene expression signatures, suggesting state-specific genetic effects[25,26]. Although fine-mapping efforts are increasingly narrowing down GWAS signals[27–31] in the immune context, pinpointing the exact causal variants and their functional mechanisms remains a major challenge.

In contrast to GWAS, whole-genome sequencing (WGS) of 2,247 individuals from 605 multiplex LOAD families uncovered 13 loci with consistent association of rare variant (MAF < 0.01) clusters, such as *CTNNA2, KIF2A, SYTL3, CLSTN2, NALCN,* and *FNBP1L*, whose products are pivotal for synaptic function and neurodevelopment[32]. This suggests that neuron-intrinsic genetic risk constitutes a previously

underappreciated dimension of LOAD. Nevertheless, limited statistical power for individual rare variants within these clusters obscures the identity of the causal alleles, and their precise functional consequences therefore remain unknown. Thus, directly measuring the effects of individual rare alleles and benchmarking them against common variants is essential to establish their relative impact and underlying mechanisms. Furthermore, immune-versus-neural cell-type divergence underscores the importance of analyzing genetic variants in disease-relevant cell types and states. Consequently, there is a critical need for systematic, large-scale functional measurements that directly compare common and rare variants, coupled with detailed mechanistic interpretations in disease-relevant cellular contexts.

Both the GWAS and WGS studies suggest that LOAD is predominantly driven by noncoding variants[3–6,32]. Noncoding genetic variants contribute to the risk of many complex diseases by disrupting gene regulation, often through interference with transcription factor (TF) binding at cis-regulatory elements (CREs) such as enhancers and promoters[33–35]. The activity of these CREs can be highly cell-type-specific and even state-specific, shaped by the availability and dynamics of distinct TFs[36–39]. This specificity implies that the effects of genetic variants on CRE function, and consequently on disease risk, are likewise context-dependent[40,41]. LOAD GWAS variants show significant enrichment in microglia and macrophage enhancers, potentially disrupting immune enhancer activities[42,43]. A well-characterized CRE is the microglia-specific enhancer ~25 kb upstream of *BIN1* that harbors the lead LOAD risk variant rs6733839. CRISPR-mediated deletion of this enhancer in human iPSC-derived microglia selectively lowers *BIN1* mRNA and protein levels, suggesting rs6733839 may modulates LOAD risk by altering microglial *BIN1* expression[43]. Although epigenomic modeling that integrates open chromatin, histone marks, and three-dimensional contacts now permits prediction of variant impacts on these CREs, current models still struggle to resolve the resulting transcriptional and cellular consequences because of the versatile, combinatorial nature of TF function.

Quantifying the functional consequences of non-coding genetic variation is intrinsically difficult: regulatory elements act in highly context-specific manner and typically elicit subtler phenotypic changes than coding mutations[44]. Massively parallel reporter assays (MPRAs) overcome many technical barriers by coupling thousands of synthesized cis-regulatory elements (CREs) to barcoded reporter constructs, positioned either upstream or downstream of a minimal promoter, to measure transcription factor-driven enhancer activity [45]. Allelic MPRAs directly contrasting CREs that differ by a single nucleotide, now provide a robust, high-throughput read-out of allele-specific regulatory effects[30,31,46–48]. Traditional *in vitro* MPRAs achieve excellent transfection efficiency and statistical power, yet they only approximate—rather than fully replicate—the *in vivo* cellular identity of their target cell type. Recent *in vivo* tissue MPRAs, including our AAV-based systemic platform (sysMPRA)[49], extended this paradigm to native contexts such as adult brain tissue, enabling measurement of regulatory dynamics within complex cellular environments[49,50]. Thoughtful selection of the experimental system therefore remains critical for accurately inferring variant function. Additionally, while MPRA effectively quantifies variant impacts on transcription, elucidating downstream effects on

endogenous gene expression remains limited. To bridge this gap, methods such as CRISPR interference (CRISPRi)[51] and CRISPR-based excision[43] have been employed to perturb enhancers, enabling profiling of affected gene expression implicated in LOAD, though still at a relatively limited scale[28,30,43]. Collectively, these experimental advances establish a versatile toolkit for disentangling the consequences of regulatory variants across diverse cellular contexts.

Complementing these experimental approaches, computational methodologies continue to evolve to interpret how genetic variants influence context- and cell-type-dependent gene expression. Early computational frameworks relied on position weight matrices representing individual TF motifs[52]. Over the past decade, sequence-to-function models such as DeepSEA[53], Enformer[54], ChromBPNet[55], DeepAllele[56] and GET[57] have advanced the field by using deep neural networks to learn combinatorial regulatory codes directly from DNA. Although predicting gene expression from sequence alone remains difficult, these architectures now deliver state-of-the-art accuracy on chromatin-feature prediction. Within this deep-learning landscape, convolutional neural networks (CNNs)—neural networks that apply learnable filters to scan sequence features such as TF motifs—continue to excel at regulatory genomics tasks, including cell-type-specific enhancer classification[58] and genetic variant effect inference[27]. Although transformer-based, self-supervised "genomic large language models" aspire to achieve zero-shot prediction by learning the "DNA language"—that is, by modeling genome-wide sequence context and long-range dependencies—*ab initio*–supervised CNNs and their derivatives[54] currently deliver superior predictive performance, greater computational efficiency, and—crucially—enhanced interpretability for uncovering underlying biology[59,60]. Recently, multimodal foundation models such as AlphaGenome[61] have emerged, aiming to unify multiple biological data modalities for predicting variant effects; however, these larger models remain limited in their ability to capture cell-type-specific and state-specific nuances, a task at which simpler CNN architectures still outperform[62,63]. Together, these advances in deep learning provide a powerful, yet still evolving, framework for mechanistically informed prediction of variant effects on gene regulation.

To clarify how non-coding risk alleles shape LOAD in immune and neural contexts, we curated 599 LOAD-associated variants (186 rare variants, MAF < 0.01; 106 low-frequency variants, 0.01 ≤ MAF < 0.05; and 307 common variants, MAF ≥ 0.05) from GWAS and WGS, selecting those that overlap open chromatin in microglia, macrophages, or neurons (Fig. 1a). Variants were grouped by chromatin accessibility in resting and activated immune cells into immune-specific enhancers, ubiquitously active elements, and regions with limited accessibility (Fig. 1b); most reside in intronic, intergenic, or promoter-proximal positions, consistent with distal-enhancer activity.

In this study, we established an integrated experimental and computational framework that combines context-dependent *in vitro* and *in vivo* MPRA, interpretable CNN models, and CRISPRi perturbation (Fig. 1c). Leveraging a validated THP-1 macrophage model that recapitulates canonical immune states together with mouse brain tissue from the cortex, hippocampus, and striatum that captures native neural context, this approach (i)

quantifies the regulatory impact of hundreds of LOAD-associated variants, (ii) prioritizes functionally impactful alleles, (iii) dissects their cell-type- and state-specific mechanisms, and (iv) enables in-depth functional analysis of a disease-risk–associated enhancer harboring functional rare variants. Together, this framework connects noncoding genetic variation to context-dependent regulatory mechanisms and, ultimately, to the key genes and molecular pathways involved in LOAD.

Results

Characterization of THP-1 macrophages as an innate-immune-cell model for LOAD

Mononuclear phagocytes, including microglia, macrophages, and monocytes, are implicated in the genetic predisposition to LOAD[5,6,27,42,64]. Microglia, the resident macrophages of the central nervous system, continuously survey the brain parenchyma[9,10], clear amyloid-β (Aβ)[11,12] and tau aggregates[13,14], respond to neural injury[15,16], and modulate neuroinflammation[17,18], all of which are processes dysregulated in LOAD[7,8]. Although microglia are the primary brain-resident immune cells, perivascular macrophages and recruited monocyte-derived macrophages also participate in plaque clearance and secrete proinflammatory cytokines[65–68]. In microglia-depleted mouse models of LOAD, it was found that monocyte-derived macrophages repopulated the entire brain and could functionally substitute microglia, marked by amyloid plaque association as well as *Trem2*-expression[69]. Moreover, peripheral inflammation could induce microglia immune memory through epigenetic reprogramming, modifying LOAD pathology[70]. Together with microglia, peripheral immune cells are also increasingly recognized as LOAD modulators[27,71].

To model mononuclear phagocytes and LOAD-associated microglial states[25,26], we adopted THP-1 cells as a macrophage model, leveraging their transcriptomic similarity to primary microglia and macrophages[72] and their ease of genetic and pharmacological manipulation. In contrast, HMC3 microglia showed limited transcriptomic resemblance to primary microglia and were therefore used only as a secondary model in this study. Using chromatin accessibility (ATAC-seq) and transcriptome profiling (RNA-seq), we characterized THP-1 macrophages throughout differentiation and upon stimulation with interferon-β (IFN-β), interferon-γ (IFN-γ), or lipopolysaccharide plus IFN-γ (LPS+IFN-γ), modeling antiviral, M1-polarized, and hyperinflammatory states, respectively (Supplementary Tables 1 and 2).

Upon differentiation from monocytes, THP-1 macrophages demonstrated upregulated immune responses and reduced cell-cycle activity, confirming successful differentiation (Extended Data Fig. 1a). IFN-β and IFN-γ treatments predominantly increased chromatin accessibility at promoters and enhancers, activating gene expression, whereas LPS+IFN-γ triggered broader chromatin remodeling that both opened and closed regulatory regions, leading to concurrent gene activation and repression (Extended Data Fig. 1b,c, 2a,c). IFN-β activated viral defense and leukocyte chemotaxis pathways; IFN-γ induced genes involved in bacterial/lipid sensing and protein trafficking; LPS+IFN-γ not only elicited robust interferon responses but also pronounced inflammatory responses (Extended Data Fig. 1d, 2b). Marker genes for microglia and

macrophages (e.g., *TREM2*, *IBA1*) remained robustly expressed and exhibited state-specific modulation in each state (Extended Data Fig. 2d). Previous studies have shown that THP-1 macrophages exhibit transcriptomic similarity to both primary and stem-cell-derived microglia[72]; we further demonstrate that they also share epigenomic profiles with stem-cell-derived microglia (Extended Data Fig. 1e). These results demonstrate that we are able to capture gene expression and open chromatin profiles associated with different inflammatory states of mononuclear phagocytes.

Human single-nucleus transcriptomic studies of post-mortem brain tissue and cortical biopsies from living individuals have identified ~12 distinct microglial states in LOAD[25,26]. We next examined how THP-1 macrophages under different treatments might recapitulate these states. LPS+IFN-γ treatment induced marker genes of inflammatory microglial states identified in human post-mortem brains, MG10, MG2, and MG8 (ordered by descending inflammatory strength). Marker genes of the MG10 state, indicative of strong inflammation, exhibited the highest upregulation (Extended Data Fig. 2e). Inflammatory microglia are closely associated with amyloid plaques[25,26]. Sun et al. demonstrated that amyloid-β fibrils induce inflammatory responses in iPSC-derived microglia[25]. Notably, LPS+IFN-γ stimulation of THP-1 macrophages recapitulated the late (24 h) inflammatory response induced by amyloid-β fibrils (Extended Data Fig. 2f), demonstrating the pathological relevance of LPS+IFN-γ-driven inflammation. Disease-associated microglia (DAM) signatures, distributed across MG3, MG4, and MG10, were all upregulated by LPS+IFN-γ stimulation, further underscoring its disease relevance (Extended Data Fig. 2e). Additionally, antiviral state marker genes (MG11) were robustly upregulated by both IFN-β and LPS+IFN-γ, consistent with LPS-mediated endogenous IFN-β production (Extended Data Fig. 2e). These findings reflect that the THP-1 macrophages can recapitulate several key microglial states observed in the brains of LOAD human subjects.

Inflammatory and antiviral microglial states in human brains are enriched for LOAD GWAS variants[25,26]. We performed stratified linkage disequilibrium score regression (S-LDSC) and observed significant enrichment of LOAD GWAS variants in open chromatin from THP-1 macrophage states, comparable to that in primary microglia, macrophages, and iPSC/hESC-derived microglia, whereas no significant enrichment was detected in neurons (Extended Data Fig. 1f). Collectively, these data illustrate that THP-1 macrophages can recapitulate key microglial marker gene expression, activation states, and epigenomic features linked to LOAD, providing a practical model for dissecting LOAD-associated immune mechanisms.

Context-dependent MPRA identified LOAD-risk enhancers across neural and immune contexts

To systematically evaluate common and rare LOAD variant effects on cis-regulatory activities, we designed MPRA constructs with barcoded 227-bp synthetic CREs carrying reference or alternate alleles downstream of a minimal promoter, which captures enhancer-like activities (Fig. 2a). CREs were open chromatin peak-centered (variants close to open chromatin peak summit), variant-centered (distal variants), or motif-shuffled (disrupting local TF motifs), providing multiple readouts of variant effects (Fig.

2a; Supplementary Table 3). We assayed the library of 1600 CREs in four immune states (resting, IFN-β, IFN-γ, LPS+IFN-γ) by transfecting both THP-1 macrophages and the alternative microglia model HMC3, with HEK293T cells included as a non-immune control. To capture neural activity *in vivo*, the same library was delivered noninvasively to the brains of four mice via retro-orbital injection of AAV.PHP.eB virus. We dissected out and measured the regulatory activity of CREs in three brain regions: cortex, hippocampus, and striatum (Fig. 2b). Using median absolute deviation (MAD) scores as a measure of enhancer activity, we found high reproducibility between replicates (Pearson's $r \approx 0.8$-0.9 *in vitro*, $r \approx 0.6$-0.7 *in vivo*; Extended Data Fig. 3a). Activity profiles clustered by cell type, strongly correlated within immune or neural contexts but moderately across them, highlighting distinct regulatory landscapes and additional interspecies differences (Fig. 2c; Supplementary Table 4).

Approximately 13% of tested CREs (P.MAD ≤ 0.05) showed significant enhancer activity in macrophages or brain tissue (Extended Data Fig. 3b, Supplementary Table 4). Immune and ubiquitous CREs were more frequently active in THP-1 macrophages, consistent with ATAC-seq annotations, whereas in brain tissue, immune but not ubiquitous CREs retained activity (Fig. 2d). Many of those ubiquitous CREs were at promoters, which may not operate as efficiently in assays in which the candidate CRE is cloned in downstream of the TSS[73,74]. This assay limitation likely explains why immune, rather than ubiquitous, CREs appeared more active in brain tissue. Elastic net regression on TF motifs explained a substantial proportion of variance in enhancer activities ($R^2 = 0.90$, $P = 0.001$, *in vitro*; $R^2 = 0.48$, $P = 0.001$, *in vivo*; permutation test) despite higher noise in *in vivo* measurements, underscoring the central role of motif composition in shaping enhancer activity; notably, TFs linked to neural development and differentiation, including *MEF2B*, *CRX*, *CLOCK*, *NR2E1*, and *POU3F4*, emerged as key contributors to brain enhancer specificity (Fig. 2e). We further identified both cell type-specific as well as broadly active enhancer (Fig. 2f); for example, a distal enhancer at the *BIN1* locus (rs13025765/rs13025717) was selectively active in macrophages, while a segment of the *NRN1* promoter (rs192104059) showed brain-specific activity.

Among interferon stimulations, LPS+IFN-γ (hyperinflammatory) produced the most distinct enhancer responses. In THP-1 macrophages, 146 CREs (10%) showed significant activity changes in response to LPS+IFN-γ treatment, nearly half of which overlapped differentially accessible chromatin regions, while IFN-β and IFN-γ alone affected only three and one CREs, respectively (Fig. 2c; Supplementary Table 5). Similarly, in HMC3 microglia, 97 CREs responded to LPS+IFN-γ (Supplementary Table 5). Notably, LPS+IFN-γ induced widespread enhancer repression while activating only a small subset of enhancers, highlighting the role of repressive TFs in inflammatory responses (Fig. 2g). The nearest genes to these LPS+IFN-γ-responsive CREs were enriched in immune activation pathways, underscoring their functional relevance (Fig. 2h). Motif analysis revealed that the AP-1 family motif *FOSL2* and *ELK1* gained positive regulatory influence under LPS+IFN-γ, whereas *NRF2 (NFE2L2)* acted as a negative regulator, pointing to dynamic TF remodeling during inflammation (Extended Data Fig. 3c). These results reveal that LOAD risk variants converge on cell type-specific and inflammation-sensitive enhancers, providing reliable measurement of their regulatory

effects. Our MPRA assay provides a comprehensive annotation of which LOAD-associated variants containing CREs are active across different brain regions and monocyte cell states.

Context-dependent MPRA identified regulatory LOAD variants across immune and neural contexts

Having mapped a high-confidence atlas of enhancer activity across immune and neural contexts, we next asked how LOAD variants modulate those activities. Screening 599 candidate variants with 855 pairs of constructs, we identified expression-modulating alleles (emVars; FDR < 0.05) in THP-1 macrophages and HMC3 microglia under four immune states and in cortex, hippocampus, and striatum *in vivo* (Extended Data Fig. 4a, 4b, Supplementary Table 6). The variants' effects display cell-type-specific patterns (Extended Data Fig. 4c). When variant effects were aggregated across immune states or brain regions, emVars within active enhancers segregated into brain-specific, immune-specific, and nonspecific clusters (Fig. 3a), underscoring a sharp cell-type divergence in regulatory impact. Consistent with previous open chromatin partitioning (Fig. 1b), immune-specific emVars were enriched in immune CREs, brain-specific emVars preferentially resided in regions of low chromatin accessibility, and nonspecific emVars were over-represented in ubiquitous CREs, although these trends were not statistically significant (χ^2 test, $p = 0.3$; Extended Data Fig. 4d).

This divergence prompted us to investigate whether the genetic origins of LOAD variants are associated with their observed regulatory effects. Common LOAD variants identified by GWAS are enriched in microglial enhancers[3–6,29,42,43,75], whereas rare variants from patient-family sequencing studies often map to neural-development and synaptic-plasticity genes[32]. We therefore tested the hypothesis that common variants are more likely to exert effects in immune cells, whereas rare variants have greater functional consequences in neural contexts. Consistent with this prediction, in THP-1 macrophages, common variants produced larger expression changes than rare variants, whereas in brain tissue, this pattern was reversed (Fig. 3b), with the strongest effects observed among the most common variants (MAF ≥ 0.29; Extended Data Fig. 4e). Although modest, our findings support a model where common LOAD variants primarily influence immune regulation, while rare variants more frequently modulate neural functions.

To investigate the mechanisms driving this cell-type divergence, we next examined TF-motif enrichment near emVars, comparing it directly to motif enrichment within open chromatin regions in THP-1 macrophages and brain tissue. Motifs enriched in open chromatin were also preferentially enriched near emVars within the same cellular context, with consistent representation across TF families. Brain-active emVars were predominantly associated with motifs from TF families involved in neural development and function, including TALE-type homeodomain, HOX-related, NK-related, and Fos-related families (Fig. 3c). In contrast, emVars active in THP-1 macrophages were enriched for immune-related TF families such as ETS-related, IRF, STAT, and NF-κB. Together, these analyses highlight distinct, cell-type-specific regulatory codes through which LOAD-associated variants exert their effects.

We next directly tested whether the TF-motif contexts surrounding these variants functionally modulate enhancer activities. Given that LOAD variants are often predicted to disrupt immune-related TF motifs, we analyzed a set of motif-shuffled enhancers in which a 25-bp window surrounding each variant was fully shuffled to disrupt the predicted immune-related TF-motif context, a design we refer to as motif-context shuffling. Because single-nucleotide variants typically weaken, rather than abolish, TF-binding sites, we hypothesized that complete motif ablation would elicit larger transcriptional shifts. In both THP-1 macrophages and HMC3 microglia, most motif-context shuffling events caused significant disruption of enhancer activity (FDR < 0.05, Supplementary Table 7) and produced markedly larger changes in reporter expression than single-nucleotide substitutions, with the strongest effects observed at motif contexts containing STAT, MEF2, IRF, AP-1, and SPI1 motifs (FDR < 0.05, Fig. 3d). Motif-context shuffling either increased or decreased transcription, though certain TF-motif contexts showed consistent directional biases. For example, IRF-, STAT-, and AP-1-related motif contexts preferentially decreased transcription upon disruption in THP-1 macrophages, highlighting their roles as transcriptional-activating contexts (Fig. 3e). These findings provide strong evidence that variants are associated with functionally active TF-motif contexts.

TFs involved in immune-signaling pathways, such as the interferon response, are often transiently activated; thus, variants disrupting these TF-binding sites may exert regulatory effects only under specific immune conditions. To explore this possibility, we analyzed variant effects separately in antiviral (IFN-β), M1-polarized (IFN-γ), and hyperinflammatory (LPS+IFN-γ) states in both THP-1 macrophages and HMC3 microglia. We detected significant state-specific emVars (FDR < 0.05) in all conditions except IFN-β-stimulated HMC3 cells. Under hyperinflammatory stimulation, we identified seven state-specific emVars in THP-1 macrophages and four in HMC3 cells (Fig. 3f, Supplementary Table 8). Notably, rs10838702-T (*SPI1*) and rs17515931-T (*CLU*) reduced transcription exclusively under hyperinflammatory conditions, whereas rs62427420-G (*SEC63*) reduced transcription only in resting cells. Several variants exhibited more complex patterns: rs73972710-T (*CTDP1*), rs73000577-C (*UBA5*), and rs636317-C (*MS4A4E*) increased transcription in both resting and stimulated states, but showed stronger activation upon stimulation, whereas rs549746751-A (*GET3*) exerted opposing effects depending on the immune state. These examples reflect regulatory scenarios in which variants disrupt TF binding that is active only in a specific state, alter the strength of binding in a state-dependent manner, or engage distinct TFs acting on the same sequence under different immune conditions.

In summary, our MPRA identifies both cell-type-specific and immune-state-specific effects of LOAD-associated variants on enhancer activity. Context-dependent disruption of regulatory activity is associated with key TF-binding motifs and with the variant's allele frequency (common versus rare).

Deep-learning models interpret cell-type- and immune-state-specific variant effects

To interpret how LOAD genetic variants influence regulatory codes in MPRA, we trained CNN regression models on ATAC-seq data from multiple cell types, including stimulated and unstimulated THP-1 macrophages, hESC/iPSC-derived microglia, THP-1 monocytes, mouse cortex and striatum, and HEK293(T) cells. These models accurately predicted chromatin accessibility in holdout data from matched or related cell types (Spearman's $\rho \approx 0.8$), while predictions across divergent cell types yielded moderate performance (Spearman's $\rho \approx 0.5$), highlighting the cell type specificity of the regulatory codes they captured (Fig. 4a).

Using SHAP[76]-based importance scores and TF-MoDISco[77], we show that the models learned key cell type-specific TF motifs. Immune-related motifs (SPI, C/EBP, RUNX) were enriched in macrophage and microglia models, while neural motifs (EGR, MEF2, RFX) were enriched in brain models (FDR < 0.05; Fig. 4b). Only models trained on stimulated cells learned immune state-specific motifs, with IRF, NF-κB, CREB/ATF, and BATF promoting chromatin accessibility, and ZEB reducing accessibility in interferon-treated cells. To dissect TF roles in hyperinflammatory responses, we trained a model specifically on differentially accessible chromatin regions from LPS+IFN-γ-treated THP-1 macrophages (Extended Data Fig. 5a). This model revealed NF-κB, IRF/STAT, and CTCF motifs as drivers of chromatin opening, while, surprisingly, SPI and C/EBP motifs were linked to chromatin closure (Fig. 4b). SPI1 (PU.1) was previously found to be a microglial transcriptional repressor in late-stage LOAD[78] that is marked by neuroinflammation[79], suggesting a potential repressive role in hyperinflammatory responses. Together, these results demonstrate that the models successfully learned distinct transcription factor codes that underlie cell type- and state-specific patterns of chromatin accessibility.

We evaluated the models on LOAD variant-containing sequences in the MPRA library and found that immune-trained models discriminated against immune CREs from low-ATAC sequences, while brain-trained models favored ubiquitous over immune CREs, reflecting distinct regulatory codes (Fig. 4c). The models recapitulated the TF motif enrichments seen in the matched ATAC-seq datasets, capturing both cell-type- and state-specific activity as well as elements inducible by LPS-plus-IFN-γ stimulation (FDR < 0.05; Extended Data Fig. 3d,e). Overall, these findings highlight that these models capture the generalizable regulatory codes, making them valuable tools for interpreting cell type- and state-specific enhancer function.

We then applied *in silico* mutagenesis to assess allelic effects of LOAD variants (Supplementary Table 9), facilitated by generating a null distribution from negative sequences and estimating prediction uncertainty via Monte Carlo dropout in our CNN. The models effectively distinguished variants with strong versus weak regulatory effects in MPRA assays performed in THP-1 macrophages, with a similar trend observed for brain tissue, demonstrating concordance between predictions and experimental data (Fig. 4d). By integrating predicted accessibility changes and SHAP importance scores, which were significantly correlated (Spearman's $\rho = 0.8$; Extended Data Fig. 5b), the models identified variants that exhibit effects across cell types as well as variants with effects biased toward the immune or neural contexts ($P < 0.1$; Fig. 4e). Among the

strongest outliers were rs636317 (*MS4A4E*) and rs755951 (*PTK2B*), both of which alter CTCF motifs. Immune-biased variants were identified near *EPHA1*, *MS4A4A*, *BIN1*, *PICALM*, and *PTK2B*, all key microglial regulators, while brain-biased hits included variants near *SORL1*, *SNAP25*, and *NAPG*, central to synaptic vesicle trafficking and amyloid precursor protein processing. Interestingly, some variants showed consistent directional effects across cell types, while others displayed opposing effects (Extended Data Fig. 5c). These results suggest that the models can identify significant regulatory variants that align with MPRA data and capture their context-dependent effects.

To determine cell-type-specific effects of each allele, we performed linear regression on predicted allelic differences, including cell type (immune versus neural) as a covariate to isolate context-dependent effects. This analysis highlighted two major classes of variants: (i) those with a consistent direction but stronger effects in one cell type, and (ii) those with opposite effects between immune and neural contexts (Fig. 4f, Extended Data Fig. 5d, 5e). Surprisingly, common variants in *HLA-DRB1* and *HLA-DQA1*, typically associated with microglial function, showed stronger predicted effects in brain tissue. For example, exclusively in the neural context, the minor G allele of rs9271162 (*HLA-DRB1*) disrupts a TALE-type homeodomain binding site; the minor T allele of (*HLA-DRB1*) generates a repressive motif that reduces MEF2 binding; and the minor C allele of rs3104416 (*HLA-DQA1*) creates an EGR motif (Extended Data Fig. 5f). Notably, a substantial subset of these variants overlap with MPRA-validated emVars. For example, rs13025765 (*BIN1*), identified as an emVar in both THP-1 macrophages and brain tissue, increases accessibility in immune cells but decreases accessibility in the brain when the minor T allele is present. Together, these findings highlight the power of our models to resolve allele-specific regulatory effects with cell-type precision.

We next explored immune state-specific effects with models trained on LPS+IFN-γ-, IFN-γ-, IFN-β-treated, or resting THP-1 macrophages (Fig. 4g, Extended Data Fig. 5g). Variants with robust context-specificity were identified, such as rs13025765 (*BIN1*), which showed stronger effects under LPS+IFN-γ stimulation compared to the resting state, and rs189835276 (*SEC63*), which displayed stronger effects under all three interferon-activated conditions. Models trained on LPS+IFN-γ-responsive sequences provided mechanistic insight (Extended Data Fig. 3d). For example, the resting-state model predicted that for rs73972710 (*CTDP1*), the major C allele forms a repressive ZBT motif at rest, while the minor T allele disrupts this motif and increases transcription; upon stimulation, the model revealed a chromatin-opening advantage for the major allele, masking the resting-state repression and reducing allelic differences, matching MPRA findings (Fig. 4h; Fig. 3f). These examples demonstrate how the models uncover the regulatory mechanisms underlying the state-specific effects observed in experimental data.

Collectively, these findings demonstrate that LOAD risk variants exhibit dynamic, cell type- and immune state-specific regulatory effects and highlight the utility of deep learning models for predicting and interpreting variant-mediated disruptions in gene regulation.

Functional regulatory LOAD variants

By examining the overlap between MPRA data and machine-learning predictions, we found that both rare and common emVars predicted by models are distributed across THP-1 macrophages and brain tissue, forming "hotspots" where multiple variants converge within the same locus to modulate gene expression (Fig. 5a). Within a given locus, certain minor alleles enhance transcription, whereas others attenuate it, highlighting the complexity of gene regulation in these systems. Two previously uncharacterized hotspots, *SEC63-OSTM1* and *NELL2-DBX2*, were particularly enriched for rare variants with pronounced allelic effects in both macrophages and brain tissues; variants in a *NELL2* intron were active exclusively in brain tissue (Extended Data Fig. 6). The immune-associated BIN1 locus, the second-strongest genetic signal for LOAD risk[3–6], also emerged among the top hits. Although the disease risk is most often attributed to the coding ε4 allele of *APOE*, we observed potent noncoding variant effects at the *APOE-APOC1* and *APOC2* loci in both neural and immune contexts. Together, these findings illustrate how multiple distinct variants within the same locus can reshape the regulatory landscapes in a context-dependent manner, providing new insights into LOAD-associated genetic mechanisms.

Integrating multidimensional measurements of genetic variant effects, sequence-level regulatory activity, and motif context function, we synthesized a mechanistic model of regulatory variant actions (Fig. 5b). Variants can (i) destroy or create a core TF site, (ii) fine-tune the strength of adjacent TF motifs, or (iii) re-balance competition among neighboring activators and repressors; motif shuffling represents the extreme case of class (i). Guided by this framework, we prioritized candidate functional regulatory variants that met stringent criteria, including significant enhancer activity, allele-specific transcriptional differences, and, where applicable, disruption of a motif context (Fig. 5c, Supplementary Table 10). Notably, the majority of these prioritized variants also exhibited consistent predicted effects across our machine learning models.

After establishing a high-confidence set of functional regulatory variants, we examined their genomic context to identify the genes they regulate. Because the majority of candidate functional regulatory variants are located in non-promoter regions, we posited that they act through distal enhancers that physically contact target promoters. To nominate enhancer-gene pairs, we applied the Activity-By-Contact (ABC) model[80] to Hi-C, H3K27ac ChIP-seq, and ATAC-seq profiles from resting and LPS+IFN-γ-stimulated THP-1 macrophages[81], thereby integrating chromatin interaction frequency with enhancer activity (Supplementary Table 11). Interestingly, our analysis revealed three target genes (*TAS2R60*, *AZGP1*, *PIP*) associated with bitter taste sensory pathways, which were enriched among functional regulatory variants in THP-1 macrophages (Extended Data Fig. 4f).

The integrated MPRA-machine-learning framework uncovered a rich set of context-dependent functional regulatory variants and, through ABC modelling, associated each variant cluster with candidate target genes. Equipped with these genomic links, we next interrogated the mechanisms by incorporating model interpretation with CRISPR

perturbations to pinpoint how specific alleles rewire transcriptional programs in immune and neural states.

Mechanistic interpretation of functional regulatory variants at *BIN1*, *MS4A*, and *SEC63-OSTM1* loci

Within the functional regulatory variants that show impacts on enhancer activities, several loci stand out as multiple variants showing divergent effects (Fig. 6a). These include (i) an well-characterized BIN1 enhancer; (ii) an enhancer within the critical *MS4A* locus, whose gene products modulate *TREM2* expression and microglial state[82,83]; and (iii) a newly identified enhancer overlapping a rare variant cluster at *SEC63-OSTM1* locus. Here we show how these variants influence transcription via modulating TF activities differently in immune and neural contexts.

Fine-mapping at *BIN1* has prioritized rs6733839, an SNP within a microglia-specific enhancer near a SPI1 motif, where the minor T allele creates an MEF2 site and increases chromatin accessibility in iPSC-derived microglia, potentially elevating transcription[3–6,84]. Previous MPRA assays in HEK293T and THP-1 cells showed no significant allele-specific effects, though subtle upregulation was noted[30,31].

Here, we comprehensively evaluated rs6733839 using context-dependent, multilayered approaches (Fig. 6b). SNP-centered MPRA constructs again showed no significant allele-specific effects in THP-1 macrophages, brain tissue, or HEK293T cells. However, peak-centered constructs with rs6733839 at the 5′ or 3′ ends unexpectedly revealed T allele-driven transcriptional repression in THP-1 macrophages and HMC3 microglia-like cells. Machine learning models predicted increased chromatin accessibility for the T allele in both macrophages and brain tissue. Interestingly, immune models suggested the T allele strengthened the nearby SPI1 motif, leading to the observed repression in immune cells, while brain models predicted gain-of-function with MEF2 motif, consistent with upregulation detected in brain MPRA constructs. Synthetic enhancer tiling and motif shuffling analyses further revealed that the motif context surrounding rs6733839 operates as a context-dependent repressor, exhibiting potential combinatorial interactions with adjacent motifs (Extended Data Fig. 7). Its repression can be masked by a potent upstream activator, resulting in an overall activating outcome; however, it can also push downstream activators toward inactivity. Combined interactions with both upstream and downstream motifs result in net repression. Collectively, these data illustrate the complexity of enhancer logic, where a single motif may exert activating or repressive functions contingent on local sequence context and the composition of bound TFs. We also characterized rs13025717, a variant in the adjacent *BIN1* enhancer previously predicted to have its T allele disrupt a KLF4 motif meanwhile indirectly affecting the nearby PU.1 (SPI1) binding[84,85] (Fig. 6b). In THP-1 MPRA, the T allele reduced transcription, and models predicted decreased chromatin accessibility due to KLF4 motif loss. This variant has also been reported as a *BIN1* eQTL in monocytes and a SPI1 binding QTL in the B-lymphoblastoid cell line GM12878[85]. Another variant, rs13025765, showed opposing effects between THP-1 and brain, reflecting differential engagement of SPIB in immune cells versus RFX in neural contexts (Fig. 6b). Together,

these findings reveal how multiple BIN1 enhancer variants modulate LOAD risk through distinct TF mechanisms.

In *MS4A*, a major open chromatin region within *MS4A6E* intron 1 is accessible in both microglia and neurons but becomes less accessible under LPS+IFN-γ stimulation in THP-1 macrophages (Fig. 6c). We identified variants with context-specific motif effects: the T allele of rs10897049 strengthened an ETS motif, increasing transcription in macrophages but not in brain; the minor A allele of rs4477457 disrupted an E2F motif, reducing transcription in brain but not in macrophages; and rs10792265 created an RFX motif that may compete with E2F, reducing transcription in brain but not in THP-1 macrophages. These results highlight how individual motif disruptions can drive divergent immune- and neuron-specific transcriptional outcomes.

In the *SEC63-OSTM1* intergenic region, four rare variants within an enhancer showed distinct MPRA profiles: three reduced transcription alleles and one increased transcription (Fig. 6d). Notably, these variants are not in linkage-disequilibrium (LD), indicating independent effects. ML analyses suggest that the minor allele T of rs147038704 upregulates SPI1 motifs yet represses transcription, while rs115607757 G allele weakens a bZIP site, reducing macrophage transcription but increasing brain expression. The rs189835276 T allele disrupts an ETS motif, increasing macrophage transcription.

Chromatin analysis (Hi-C, ATAC-seq, H3K27ac ChIP-seq) of publicly available data[81] in THP-1 macrophages reveals that this active enhancer is positioned within a chromatin loop connecting the *OSTM1* promoter and a distal CTCF site at *AFG1L*; Hi-C data also show that the enhancer lies within a high-contact region with the *SEC63* promoter (Extended Data Fig. 8 a,b). These results suggest that the enhancer has the potential to regulate both *OSTM1* and *SEC63* expression. Consistently, RNA-seq confirms strong expression of *OSTM1* and *SEC63* (Supplementary Table 12).

Functionally, *SEC63* and *OSTM1* are involved in ER import and lysosomal acidification, linking them to LOAD-related ER stress, lysosomal dysfunction, and APP trafficking. To clarify the enhancer's regulatory role, we performed CRISPRi knockdowns of the enhancer as well as *SEC63* and *OSTM1* in THP-1 macrophages under both resting and hyperinflammatory conditions. Surprisingly, enhancer repression left *SEC63* and *OSTM1* unchanged but elevated the LOAD effector genes *GSAP* and *SSH1* by ~30 % (Fig. 6e). In the resting state, the perturbation up-regulated complement genes and down-regulated proliferation pathways (G2M checkpoint, E2F and MYC targets), steering macrophages toward an M1-like state (Fig. 6f). Under LPS+IFN-γ stimulation, the same knock-down amplified TNFα–NF-κB, Notch and KRAS-up signatures and further suppressed E2F targets, reinforcing inflammatory, metabolic and pro-survival pathways. Collectively, these data indicate that the enhancer functions as a gatekeeper for innate-immune signaling. *GSAP* and *SSH1* were also upregulated in amyloid-treated iPSC-microglia and LPS+IFN-γ-stimulated THP-1 macrophages (Supplementary Table 12), implicating their roles in inflammation. Notably, knockdown of *SEC63* or *OSTM1* also affected immune response pathways and cellular metabolism, with SEC63

knockdown producing broader effects, especially under inflammatory conditions, underscoring their critical roles in macrophage function (Fig. 6e, Extended Data Fig. 8c, 8d, 8e).

Together, these findings reveal how functional regulatory variants at *BIN1*, *MS4A*, and *SEC63-OSTM1* modulate transcription through distinct, cell type- and context-specific mechanisms, highlighting the critical roles of enhancer architecture and TF networks in orchestrating immune and neural programs relevant to LOAD.

Discussion

GWAS and rare variant studies continue to expand the catalogue of LOAD risk variants, yet fine-mapping these loci remains challenging. In GWAS, tightly linked variants often share indistinguishable association statistics, making it hard to nominate the true causal allele within each LD block. Conversely, WGS highlights ultra-rare variants, but their effect estimates are under-powered without complementary functional evidence. Compounding these issues, LOAD pathogenesis spans multiple cell types and tissues, so variants must be interpreted in the specific cellular contexts where they exert their effects.

Our study combined context-dependent *in vitro* and *in vivo* MPRA, deep learning models, and CRISPRi perturbations to systematically map the cell type- and state-specific regulatory effects of 599 LOAD-associated noncoding variants. By examining both common and rare variants across human myeloid cell lines, brain tissue, and diverse immune states, we uncovered striking heterogeneity in functional outcomes. We found several variants exhibiting opposing effects across cell types, underscoring the importance of testing variants in disease-relevant tissue, cellular, and immune conditions. This integrated framework highlights how noncoding variation shapes distinct immune and neural regulatory programs, offering mechanistic insights into the genetic architecture of LOAD.

Although previous GWAS and epigenomic studies highlighted the enrichment of LOAD risk variants in microglial and macrophage enhancers, most functional work has focused narrowly on common variants or immune contexts, leaving rare variants and neural settings largely unexplored. Here, we systematically compare common and rare LOAD variants across immune and neural contexts using reporter assays and deep learning. We show that common variants tend to exert stronger regulatory effects in immune cells, whereas rare variants tend to affect transcription more significantly in the brain context. These findings support our hypothesis that common LOAD variants identified by GWAS and enriched in microglial enhancers[3–6,29,42,43,75] are more likely to affect immune regulatory programs, whereas rare variants identified through patient-family sequencing studies—often mapped to genes involved in neural development and synaptic plasticity[32]—are more likely to exert their effects in a neural context. Although the rare variants we tested are frequently located in regions with low ATAC signal, their potential gain-of-function roles or activities during developmental stages—when chromatin is generally more accessible—should be considered. Additionally, during aging, cells can undergo epigenomic erosion[29,86], a process in which closed chromatin

becomes more accessible and active regulatory elements lose activities leading to loss of cell identity, potentially enabling these variants buried in closed chromatin to exert effects later in life. The role of rare variants remains underappreciated in LOAD research, and identifying and understanding their functional impact is only the beginning.

By integrating MPRA and machine learning interpretations, we identified regulatory "hotspots" where multiple variants converge to modulate gene expression. Mechanistically, variants disrupt or strengthen TF binding sites, fine-tune motif strength, or rebalance competition among adjacent activators and repressors. Leveraging multidimensional measurements, we nominated functional regulatory variants and link enhancers to their target genes, including an unexpected enrichment of sensory genes, implicated in early LOAD deficits, in THP-1 macrophages.

Detailed analyses of representative loci revealed mechanisms underlying cell type-specific variant effects (Fig 6, Extended Data Fig. 7). At *BIN1*, prior MPRA studies using SNP-centered constructs failed to detect allele-specific effects; however, by employing longer, peak-centered constructs, we uncovered a reproducible repressive effect of the rs6733839 T allele in macrophages, mediated by SPI1 rather than the previously predicted MEF2 motif. Motif tiling further revealed complex interactions between the variant's local context and neighboring motifs. Similarly, the rs13025717-T allele in another *BIN1* enhancer was previously shown to reduce transcription in HEK293T MPRAs. In our THP-1 macrophage MPRAs, we observed T allele-driven repression only in SNP-centered constructs, while peak-centered constructs showed no effect. Model predictions pointed to SP/KLF motif disruption in immune, but not neural, contexts. These findings, along with the results of Ernst et al.[45] and Klein et al.[73], highlight how variant positioning and CRE length critically influence the detection and interpretation of regulatory effects, underscoring the need for diverse MPRA designs to capture motif interactions.

In parallel with the recent work of Bond et al.[31], we examined variant effects under immune stimulation. We showed that LPS+IFN-γ, which mimics the hyperinflammatory state relevant to LOAD, elicited the most pronounced chromatin remodeling (ATAC-seq) and enhancer-activity shifts (MPRA) in THP-1 macrophages. Notably, at the resting THP-1 macrophages, rs73972710 (*CTDP1*), the major C allele forms a repressive ZBT motif at rest, whereas the minor T allele disrupts this motif and elevates transcription; upon LPS+IFN-γ stimulation, the major allele gains higher motif scores that mask the resting-state repression and reduces allelic differences, a pattern captured by both our models and MPRA readouts (Fig. 3f, 4h). Beyond *CTDP1*, several variants at other LOAD risk loci—including the immune-regulatory *MS4A* cluster, which multiple fine-mapping studies have implicated in disease susceptibility[27,28,30,85,87]—showed comparable allele-by-stimulation interactions, further underscoring the importance of assaying variants in disease-relevant cellular states. These cases, along with our immune-state profiling of macrophages demonstrate that the magnitude of LOAD-associated variant effects is dynamically tuned by cellular states, such as the inflammatory states implicated in the disease. Context dependence therefore extends

beyond cell-type specificity to a temporal dimension in which immune activation scales variant impact. Evaluating candidate variants within disease-relevant immune milieus is thus essential for revealing their full pathogenic potential.

At the *SEC63-OSTM1* intergenic enhancer, we identified four functional regulatory rare variants with independent, allele-specific transcriptional effects in THP-1 macrophages mediated through immune motifs. Although Hi-C analysis implicated enhancer interactions with the nearby genes *SEC63* and *OSTM1*, CRISPRi-mediated enhancer perturbation unexpectedly increased expression of distant LOAD effector genes, notably *GSAP* and *SSH1*, while enhancing pro-inflammatory signaling pathways without altering *SEC63* or *OSTM1* transcript levels. γ-Secretase activating protein (*GSAP*) promotes amyloid-β production via interactions with the γ-secretase complex and amyloid precursor protein (*APP*)[88], whereas Slingshot-1 (*SSH1*), an actin phosphatase, attenuates Nrf2-mediated antioxidant responses, with its loss ameliorating Aβ and tau pathology[89]. Thus, increased expression of *GSAP* and *SSH1* likely exacerbates complementary pathogenic mechanisms in LOAD—amyloid deposition and oxidative stress—indicating the enhancer typically serves as a suppressor of these detrimental pathways. Remarkably, although *GSAP* and *SSH1* reside on chromosomes distinct from the enhancer, both genes exhibited altered expression following enhancer perturbation and were upregulated in the inflammatory macrophages, likely reflecting secondary consequences of enhanced innate immune activation. These findings highlight a notable instance wherein distal noncoding regulatory elements modulate LOAD-associated networks through non-canonical or higher-order interactions, linking noncoding genetic variation to amyloidogenesis, oxidative stress, and neuroinflammation.

These mechanistic insights were enabled by several technical advances that improved both the sensitivity and resolution of our measurements. Transcriptomic and epigenomic profiling of cytokine-stimulated THP-1 macrophages ensured that variant effects were assayed in immune states relevant to LOAD pathophysiology. We optimized electroporation-based delivery of MPRA libraries into THP-1 cells, which are typically challenging to transfect, enabling reproducible detection of stimulus-responsive enhancer activities. Building on previous work by Brown et al.[49], which demonstrated systemic AAV-mediated MPRA delivery across the blood-brain barrier (sysMPRA), we achieved increased reproducibility and larger library sizes using pseudo-barcoding strategies that aggregate barcodes with similar representation to establish robust expression estimates across individual animals. In parallel, we adapted convolutional neural networks from Ramamurthy et al.[27] to predict chromatin accessibility using 500 bp sequences, achieving consistent performance across cell types and datasets, including those generated in different laboratories. To quantify machine learning-predicted variant effects with confidence, we applied both cell-type-matched null distributions and dropout-based uncertainty estimation. Together, these innovations enabled high-confidence, context-specific dissection of noncoding variant function at scale, laying the foundation for systematic interpretation of regulatory architecture in LOAD.

Several limitations warrant mention. THP-1 and HMC3 cells, while experimentally tractable, are surrogates for primary human microglia and macrophages and do not fully capture the complexity of the brain immune milieu. Although we have previously demonstrated an overall conservation of the 'regulatory code' between rodent and primate[90,91], our *in vivo* MPRAs in mice may introduce cross-species regulatory differences. Moreover, synthetic CREs, though powerful, may overlook contributions from long-range chromatin contacts, topological features, or promoter-like elements. We also note that some variants, such as rs563571689 at the last nucleotide of *APOE* exon 1, are predicted to alter splicing without affecting MPRA output, highlighting the importance of complementary assays to capture the full regulatory landscape. While we identified variants with effects specific to brain tissue rather than immune cells, we lacked the statistical power to resolve region-specific effects within the brain. Furthermore, variants with cell type-restricted regulatory functions may be masked in bulk-tissue MPRAs due to their limited representation in the sampled population. Continued method development is needed to achieve single-cell resolution within the native tissue context. Emerging droplet-based single-cell[92,93] and spatially resolved[62] MPRA platforms offer a promising path to pinpoint subtle, context-specific effects, such as those acting in neural subtypes or immune activation states not represented in our current *in vitro* systems.

Our findings open key avenues for future research, including systematic enhancer-gene mapping, investigation of variant effects in motif-motif interactions, functional studies of hotspot genes, and defining the cellular states where variants become active to guide therapeutic strategies. Together, these efforts will deepen our understanding of noncoding genetic risks and advance the development of precision therapies for LOAD.

Methods

Cell Culture and Animals

THP-1 Macrophage Differentiation

THP-1 monocytes (ATCC TIB-202) were cultured in RPMI-1640 supplemented with 10% fetal bovine serum (FBS) at 37°C in 5% CO_2, with a density of under 1 million cells/mL. Differentiation into macrophages was induced by treating cells with 100 nM phorbol 12-myristate 13-acetate (PMA, Sigma-Aldrich) for 72 h, followed by a 24 h resting period in PMA-free medium.

HMC3 Microglia-like Cell Culture

HMC3 microglia-like cells (ATCC CRL-3304) were cultured in Microglial Cell Medium Kit (Accegen, ABI-TM009) and maintained at 37°C with 5% CO_2. Cells were passaged before reaching confluence and seeded at appropriate densities for downstream assays.

HEK293T Cell Culture

HEK293T cells (AAVpro(R), Clontech, Cat. No. 632273) were cultured in Dulbecco's Modified Eagle Medium (DMEM) supplemented with 10% fetal bovine serum (FBS) and

maintained at 37°C with 5% CO_2. Cells were passaged into fresh medium before reaching confluence and seeded at appropriate densities for downstream assays.

Stimulation of THP-1 Macrophages and HMC3 Microglia
To model diverse immune states, THP-1 macrophages were stimulated for 4 h and HMC3 microglia for 24 h with interferon-β (IFN-β, 20 ng/mL; R&D Systems), interferon-γ (IFN-γ, 20 ng/mL; PeproTech), or lipopolysaccharide (LPS, 100 ng/mL; InvivoGen) plus IFN-γ (20 ng/mL) to induce antiviral, M1-like, and hyperinflammatory states, respectively. For ATAC-seq characterization of THP-1 macrophages, THP-1 macrophages were additionally stimulated for 24 h to assess longer-term transcriptional and chromatin accessibility changes. Stimulated cells were harvested for RNA-seq, ATAC-seq, and MPRA assays.

Animals
All procedures were approved by the Carnegie Mellon University Institutional Animal Care and Use Committee (IACUC). Experiments were conducted on 10-week-old C57BL/6J mice (Jackson Laboratory, strain 000664; n = 4, 2 males and 2 females). Animals were housed under specific-pathogen-free conditions in individually ventilated cages (≤ 5 mice per cage) containing corncob bedding and nestlet enrichment. The animal room was maintained at 20-22 °C with 45 % relative humidity and a 12 h:12 h light-dark cycle. Autoclaved standard chow (LabDiet 5001) and UV-irradiated water were provided *ad libitum*. Detailed surgical procedures are described in the section 'Plasmid Library Transduction of Mouse Brain Regions via AAV Viruses'.

ATAC-seq Experiments

Cell Preparation and Lysis
THP-1 monocytes were centrifuged and pelleted, lysed using pre-chilled Buenrostro lysis buffer[94], homogenized with a Dounce homogenizer on ice, and then debris was removed by filtration through a 70 µm mesh. Similarly, THP-1-derived macrophages, adhered to 6-well plates, were lysed with pre-chilled Buenrostro lysis buffer on ice for 10 minutes. Nuclei were dislodged using cell scrapers, filtered through a 70 µm mesh, and pelleted by centrifugation at 500 xg for 5 minutes at 4°C.

Nuclei Isolation and DNA Tagmentation
Isolated nuclei were resuspended in nuclease-free water. DAPI-stained nuclei were quantified to approximately 50,000 using a Countess II cell counter (Thermo Fisher Scientific). These nuclei underwent DNA tagmentation using the Illumina Tagment DNA TDE1 Enzyme and Buffer Kits, incubated at 37°C with shaking at 300 rpm for 30 minutes.

Library Preparation and Amplification
Tagmented DNA was purified using the Qiagen MinElute PCR Purification Kit. The sequencing library was then prepared using NEBNext High-Fidelity PCR Master Mix and primers (Eurofins Genomics) following the Illumina Nextera tagmentation format as previously published[95], with the optimal number of amplification cycles determined via

qPCR side reactions to be an average of 9 cycles. Final PCR products were purified using the NEB Monarch Nucleic Acid Purification Kit (# T1030).

ATAC-seq Library Sequencing
MPRA sequencing libraries were pooled and sequenced on the Illumina NovaSeq™ 6000 platform at GENEWIZ from Azenta Life Sciences using paired-end 150 bp reads. The libraries achieved an average sequencing depth of 68 million reads per sample.

ATAC-Seq Data Processing
FASTQ files were processed using the ENCODE ATAC-Seq Pipeline. Paired-end sequencing reads from biological replicates in fastq format were analyzed with the pipeline's default settings. The Irreproducible Discovery Rate (IDR) optimal peaks, derived from these analyses, were utilized for both differential analyses and machine learning model training.

Differential Analysis of THP-1 Macrophages upon Stimulation
Common open chromatin regions were identified by merging IDR optimal peaks from both resting and stimulated THP-1 macrophages within a 200 bp proximity. This merging was performed using the bedtools suite with the command: bedtools sort -i {input} | bedtools merge -d 200 -i - > {output}. Read counts at each peak for each cell type were quantified using the featureCounts function from the Rsubread package, utilizing the bam files and bed files of common chromatin peaks. Differential accessibility analysis was executed using the DESeq2[96] package, with filtering criteria set to include peaks that had at least one read in a minimum of two replicates. Peaks with significantly different accessibility were determined using a false discovery rate (FDR) threshold of <0.05. Differentially accessible promoter regions were annotated using the hg38 human genome assembly, focusing on known genes within a 500 bp range of the identified open chromatin regions.

Variants Enrichment Analysis: stratified LD Score Regression (S-LDSC)
To pinpoint cell types enriched for LOAD risk, we applied stratified LD score regression (S-LDSC)[97] on open chromatin data from various sources. We obtained open chromatin promoter, enhancer and dyadic peaks for 111 reference epigenomes from the Epigenome Roadmap database[36]. These peaks were merged using bedtools[98] and treated as background peaks. Following the original S-LDSC methodology, testing LOAD variants in enrichment in the open chromatin peak of the candidate cell type relative to the Roadmap background. Enrichment p-values were then adjusted across all tests using the Benjamini-Hochberg FDR correction, with enriched cell types defined by a q-value below 0.05. This analysis was performed separately for using different GWAS summary statistics[3–6].

RNA-seq Experiments

RNA-seq library preparation and sequencing
Total RNA was isolated with the RNeasy Mini Kit (Qiagen) and RNA integrity was verified on an Agilent 4200 TapeStation. For THP-1 characterization, three biological

replicate batches of THP-1 macrophages (± stimulation) and THP-1 monocytes were processed for unstranded poly(A)+ RNA-seq. For CRISPRi samples, total RNA was harvested 4 h after ±stimulation; two biological replicate batches were prepared for (i) poly(A)+ stranded RNA-seq and (ii) rRNA-depleted stranded RNA-seq. All libraries were sequenced by GENEWIZ from Azenta Life Sciences (paired-end 2 × 150 bp).

Poly(A)+ libraries

Total RNA (500 ng per sample) was quantified on a Qubit 2.0 Fluorometer (Thermo Fisher Scientific) and integrity assessed on a 4200 TapeStation (Agilent). External RNA Controls Consortium spike-ins (ERCC Mix 1, Thermo Fisher Scientific, cat. 4456740) were added to the normalized RNA before library construction.

Strand-specific libraries. Polyadenylated RNA was enriched and strand-specific libraries were prepared with the NEBNext Ultra II Directional RNA Library Prep Kit for Illumina (New England Biolabs) according to the manufacturer's guidelines. mRNA was fragmented for 8 min at 94 °C, first-strand cDNA was synthesized, and dUTP was incorporated during second-strand synthesis. After end repair/A-tailing, indexed adapters were ligated and libraries were amplified by limited-cycle PCR.

Unstranded libraries. RNA-seq libraries lacking strand information were generated with the NEBNext Ultra II RNA Library Prep Kit for Illumina (New England Biolabs). Poly(A)+ RNA was captured with Oligo(dT) beads and fragmented for 15 min at 94 °C, followed by first- and second-strand cDNA synthesis. Subsequent end repair/A-tailing, adapter ligation, and limited-cycle PCR amplification mirrored the strand-specific workflow.

Library size profiles were confirmed on the TapeStation, and concentrations were determined by Qubit and KAPA Library Quantification qPCR. Equimolar pools were sequenced on an Illumina NovaSeq 6000 in paired-end mode (2 × 150 bp), targeting ~30 million read pairs per sample.

rRNA-depleted libraries

Total RNA (500 ng) was treated with TURBO DNase (Thermo Fisher Scientific) and rRNA removed using the QIAseq FastSelect-rRNA HMR Kit (Qiagen). Strand-specific libraries were prepared with the same NEBNext Ultra II kit. rRNA-depleted RNA was fragmented for 8 min at 94 °C, followed by first- and dUTP-labelled second-strand synthesis, 3′ adenylation, adapter ligation and limited-cycle PCR (second-strand amplification suppressed by dUTP). Library size was verified on the TapeStation and quantified by Qubit 4.0 and KAPA qPCR. Equimolar pools were clustered on an Illumina NovaSeq X and sequenced in paired-end mode (2 × 150 bp).

RNA-seq Data Processing

Raw paired-end reads were trimmed of adapter sequences and quality-checked using FastQC[99]. Reads were then aligned to the human reference genome (Ensembl GRCh38) using STAR[100]. Gene-level counts were obtained with featureCounts (Subread package) using '--largestOverlap -s 0' parameters for unstranded RNA-seq and using '--largestOverlap -s 2' for stranded RNA-seq. The resulting count matrices

were imported into R, filtered to remove low-expressed genes, and analyzed with DESeq2[96], adjusting for batch effects where applicable. lfcShrink using Approximate posterior estimation for GLM coefficients (apeglm)[101] was used to shrink log2 (fold change) for genes with low read counts. Independent Hypothesis Weighting (IHW)[102] was used for multiple testing corrections. Gene annotations were retrieved via biomaRt to map Ensembl gene IDs to standard gene symbols.

Gene Set Enrichment Analysis (GSEA)
Hallmark gene sets were obtained from the msigdbr package by filtering for "H" category (Hallmark). Genes were ranked based on a statistical measure derived from their differential expression results 'unshrunk log2FoldChange / lfcSE'. After removing duplicates and low-confidence entries, fgsea was performed on the ranked list, examining Hallmark pathways of size 15-500 genes. Significant pathways (adjusted $p < 0.05$) were visualized in bar plots of Normalized Enrichment Scores.

Microglia-state concordance
Marker sets for 12 human microglial states and the gene list differentially expressed in amyloid-fibril-treated iPSC microglia were downloaded from Sun et al.[25]. For each THP-1 state or CRISPR-i perturbation, gene-level $\log_2$-fold-changes ($\log_2$FC) were calculated versus matched controls. Distributions of marker-gene $\log_2$FCs were compared with the non-marker background using two-sided Mann-Whitney U tests; Benjamini-Hochberg correction was applied, and terms with $q < 0.05$ were deemed significant.

MPRA Plasmid Library Design

Prioritization of late-onset Alzheimer's disease (LOAD) Genetic Variants
To prioritize LOAD-associated variants for evaluation with both machine learning models and reporter assays, we first assembled a collection of sentinel LOAD GWAS variants from Jansen et al.[4] and Kunkle et al.[6] that met a significance threshold of 5×10^-8. We then broadened this collection by including variants in linkage disequilibrium with the sentinel variants, using HaploReg (v4.1)[103], which leverages data from the 1000 Genomes Project[104]. Applying an LD r^2 threshold of 0.5 resulted in an expanded set of 1,209 variants. Additionally, we gathered variants from the Cure Alzheimer CIRCUITS consortium, including those from fine-mapping studies[29] and patient family studies[32]. The complete set of LOAD genetic variants was subsequently overlapped with open chromatin datasets from immune and neural cells (as shown in Fig. 1b). R package annotatr[105] was used to generate genomic annotations for variants. Finally, LOAD GWAS and fine-mapping variants were filtered to retain those within 113 bp of open chromatin peak summits, while all variants from patient family studies were preserved.

Design of cis-regulatory elements (CREs)
A total of 599 unique common and rare variants from LOAD GWAS and WGS were incorporated into 227 base pair synthetic CREs. Variants overlapping open chromatin peak summits in microglia and monocytes, which represent regions most likely to serve as TF binding sites, were prioritized. When a variant overlapped a peak in immune cells

or neurons, the summit served as the center of the enhancer. For variants not overlapping open chromatin peaks, SNP-centered enhancers were designed. Additional constructs were generated for variants positioned distal (83 bp) to peak summits and for those with multiple alternate alleles. In addition, 25 base pair motif-shuffled versions of the CREs were produced as positive controls to disrupt TF binding, particularly for variants predicted to affect immune- and neuron-related factors in haploR[52,106] (MEF2, SPI1, IRF, STAT, NF-κB, AP-1).

MPRA Experiments

Plasmid Library Assembly

A pool of 24,000 unique 300-nt oligonucleotides (Twist Bioscience, San Francisco, CA, USA) was PCR-amplified (12 cycles; 66 °C annealing) with KAPA HiFi HotStart Polymerase (Roche) using primer (5′-GGCTACCGTCTCACATGGAGTCTGAACCTGTGTGCTA-3′) and primer (5′-GGCTACCGTCTCGACCACTACGATGCTCTTCCGATCT-3′). Amplicons were verified on a D1000 ScreenTape system (Agilent) and purified with the Monarch PCR & DNA Cleanup Kit (NEB).

The MPRA backbone (pAAV-Hsp68-nls/mCherry-MPRAe) was linearized by PCR (35 cycles; 72 °C annealing) with Q5 High-Fidelity DNA Polymerase (NEB) using primer (5′-GGCTACCGTCTCCCATGTTTCTCCATTTGGCGC-3′) and primer (5′-GGCTACCGTCTCGTGGTACTTAGCATCTCAC-3′). The product was gel-separated and extracted with the Monarch Gel Extraction Kit (NEB).

Purified insert and the linearized vector were assembled at a 2:1 molar ratio using the NEB Golden Gate Assembly Kit (BsmBI-v2) under the following thermal program: 42 °C for 1 h, 60 °C for 5 min, then 4 °C hold. 4 uL of the assembly reaction was electroporated into 100 µL of ElectroMAX 10-beta T1 E. coli (Thermo Fisher Scientific). Transformants were expanded in 3 L Terrific Broth at 37 °C, and plasmid DNA was purified with the QIAGEN Plasmid Plus Giga Kit.

Plasmid Library Transfection of Stimulated THP-1 Macrophages

On the day of transfection, the culture supernatant was collected for later use. The cells were detached from the dish with Invitrogen Accumax at 37 °C for 30 min. Transfection was performed using the Nucleofection P3 Primary Cell 4D-Nucleofector kit (Lonza Bioscience). In each electroporation, 2 µg of the MPRA plasmid library was used to transfect 3 million THP-1 macrophages. Cells from five electroporations were pooled and seeded in 6-well plates, then incubated at 37 °C for 1 hour to allow attachment. Next, the medium containing the nucleofection reagent was replaced with the previously collected supernatant, and interferons were added. 4 hours post-electroporation, cells were lysed directly in the wells, and lysates were snap-frozen and stored at -80 °C for RNA extraction. A replicate of each condition was scraped from the plates, snap-frozen in a separate tube, and stored at -80 °C for genomic DNA extraction.

Plasmid Library Transfection of THP-1 Monocytes

THP-1 monocytes in suspension were pelleted by centrifugation at 300 × g for 5 min. Transfection was conducted using a LONZA Nucleofector 4D device with the SG Cell

Line 4D-Nucleofector kit. In each electroporation, 1.5 µg of the MPRA plasmid library was used to transfect 3 million THP-1 monocytes. 4 hours post-electroporation, the cells were pelleted, washed with DPBS, and lysed. The resulting lysates were snap-frozen and stored at -80 °C. In parallel, a portion of each cell pellet was snap-frozen in a separate tube for genomic DNA extraction.

Plasmid Library Transfection of HMC3 Microglia and HEK293T Cells
3 million HMC3 or HEK293T cells were seeded in 100 mm dishes 24 hours before transfection. For each dish, 18 µg of the MPRA plasmid library was transfected using 54 µL of Promega FuGene 6. At 24 hours post-transfection, HEK293T cells were washed with DPBS and lysed in the dish for total RNA extraction, and HMC3 cells were treated with interferons. 24 hours after interferon treatment, HMC3 cells were washed with DPBS and lysed in the dish for total RNA extraction. Immediately before cell lysis, 25% of each sample was scraped from the plate, snap-frozen in a tube, and stored at -80 °C for genomic DNA extraction.

Plasmid Library Transduction of Mouse Brain Regions via AAV Viruses
The plasmid pool was packaged into adeno-associated virus PHP.eB (AAV-PHP.eB) following Brown et al.[49]. Adult C57BL/6J mice (n = 4; two males, two females; 10 weeks old) were anesthetized with 3-4 % isoflurane in oxygen until respiration slowed and the pedal-withdrawal reflex was lost. Each mouse was maintained in 1-2% isoflurane and received two retro-orbital injections of 2 × 10^12 vector genomes (vg) in 85 µl phosphate-buffered saline (PBS), administered 48 h apart. Immediately after each injection, 0.5 % proparacaine hydrochloride ophthalmic solution was applied to the treated eye for comfort, and the animals were monitored continuously for signs of pain or distress.

4 weeks after the second injection, mice were deeply re-anesthetized with isoflurane to the point of absent reflexes and euthanized by decapitation in compliance with institutional guidelines. The cortex, hippocampus and striatum were rapidly micro-dissected from 300 µm coronal brain sections on an ice-chilled stage and snap-frozen on a −80 °C cooling block for subsequent extraction of total RNA and genomic DNA.

cDNA MPRA Sequencing Library Preparation
cDNA libraries were prepared according to the sysMPRA[49] protocol. Cell pellets or frozen tissues were used to extract total RNA following the standard protocol of the Qiagen RNeasy kit, including on-column DNase digestion. The resulting RNA samples were further treated with Invitrogen TURBO DNase to remove residual genomic DNA, followed by a cleanup step using the Qiagen MinElute kit. First-strand cDNA was synthesized using Invitrogen SuperScript IV reverse transcriptase and a customized plasmid-sequence-specific primer. MPRA sequencing libraries were then prepared by PCR amplification (26 cycles) with NEBNext High-Fidelity 2X PCR Master Mix and Nextera primers. The PCR products were purified with the NEB Monarch Nucleic Acid Purification kit, quantified using Qubit, and assessed for purity on a TapeStation.

Genomic DNA MPRA Sequencing Library Preparation

Genomic DNA was extracted from cell pellets or frozen tissues using the Qiagen DNeasy Blood & Tissue Kit. MPRA sequencing libraries were then generated by PCR amplification (26 cycles) with NEBNext High-Fidelity 2X PCR Master Mix and the same plasmid-sequence-specific primers from Brown et al.[49]. For cell-derived samples, 20 ng of genomic DNA was used as the template; for brain tissue, 200 ng of genomic DNA was used. The PCR products were purified using the NEB Monarch Nucleic Acid Purification kit, quantified by Qubit, and evaluated on a TapeStation for product purity.

MPRA Library Sequencing

MPRA sequencing libraries were pooled with ATAC-seq libraries to increase library diversity and sequenced on the Illumina NovaSeq™ 6000 platform at GENEWIZ from Azenta Life Sciences using paired-end 150 bp reads. The cDNA libraries achieved an average sequencing depth of 16 million reads per sample, while the genomic DNA (gDNA) libraries received an average of 4 million reads per sample.

MPRA Data Analysis

Read Mapping and Preprocessing

The paired-end sequencing reads of the cDNA and DNA prepared from each sample were mapped to generate a read count matrix according to both 10 bp sequences at 5' end and 3' end of the enhancer and the 8 bp barcodes associated with each enhancer. 21 enhancers that have barcode read counts underrepresented in the DNA read count matrix were filtered out in the analysis. The read count matrix was transformed into an enhancer table and allele table. The enhancer table contains one unique enhancer per row and individual barcode counts for each sample in separate columns. The allele table has each ALT-allele:REF-allele comparison or MOTIFDISRUPT:REF allele comparison in each row and barcodes unique to each allele in a specific sample in each column.

Pseudo-barcodes for Sparse Data

The read count matrices generated from brain tissue and THP-1 monocytes were found to be more sparse than other cell models, which introduces noise to quantification. We transformed the sparse matrices to dense matrices by merging the read counts of similarly represented barcodes into pseudo-barcodes. The barcode read count matrices of brain tissue samples and THP-1 monocytes were transformed to create pseudo-barcodes. First, we sorted 15 barcodes of each enhancer according to the sum of read counts across brain tissue or THP-1 monocytes, and then summed the read counts of every three barcodes in the sorted order to generate five pseudo-barcodes for each enhancer. Pseudo-barcodes showed an improved DNA correlation (Spearman correlation around 0.75) between biological replicates and between sparse data and dense data. The enhancer table and allele table of pseudo-barcodes were used to analyze the mouse brain tissue and THP-1 monocyte, and the original barcodes were used for other cell types.

Quantification of Enhancer Activities

We used the quantitative analysis function of *MPRAnalyze*[107] to estimate transcriptional

activity for each candidate regulatory element (CRE), leveraging the paired cDNA and DNA read counts from 15 barcodes pre-designed for each CRE. For each cell type, we applied the regression design dnaDesign = ~Barcode + Replicate, rnaDesign = ~1. To harmonize enhancer activity measurements across in vitro and in vivo models, we employed a conservative median absolute deviation (MAD)-based score (P.MAD.Score < 0.05, one- and two-tailed) to identify significantly active enhancers in each context. For visualization of specific examples, we computed per-replicate transcriptional activities for each CRE.

Quantification of Allelic Differences and Motif Disruption

To compare transcriptional differences attributable to allelic variants and motif shuffling, we used the comparative analysis function of MPRAnalyze[107] with at least 4 biological replicates per condition. In these analyses, we compared constructs harboring the CRE with the major versus minor allele, as well as constructs in which the motif was shuffled. The regression design was specified as dnaDesign = ~Barcode + Replicate, rnaDesign = ~Allele, reducedDesign = ~1.

To examine the effect of interferon stimulation on allelic differences, we used the design dnaDesign = ~Barcode + Replicate, rnaDesign = ~Allele + Stimulation + Allele:Stimulation, reducedDesign = ~Allele + Stimulation. For aggregated analyses across stimulated THP-1 macrophages, HMC3 microglia, and mouse brain regions, we included an additional covariate “Condition” in both the rnaDesign and reducedDesign to account for the different conditions.

Motif-based prediction of enhancer activity

MPRA sequences were scanned with FIMO v5.5.5 (MEME-Suite; http://meme-suite.org) against the HOCOMOCO v12 CORE motif library using a threshold of $P < 1 \times 10^{-4}$. For each enhancer, hits sharing the same HOCOMOCO accession (for example, MA0139) were merged by averaging log-likelihood scores, yielding a motif-by-enhancer score matrix.

Condition-specific enhancer activities (MAD Scores) from THP-1 macrophages (Resting, LPS+IFN-γ) and mouse brain tissue were joined to the motif matrix on enhancer ID; absent motifs were set to zero.

To identify motifs associated with activity, we fitted an Elastic Net model to each condition. Motif scores were z-standardized, and ElasticNetCV from scikit-learn v1.4.0 (https://scikit-learn.org) was run with the default l_1 ratio of 0.5 and the package’s built-in grid of 100 logarithmically spaced α values (five-fold cross-validation, max_iter = 10^5, random_state = 0). After selecting the best hyper-parameters, we refitted the model once and estimated the significance of the in-sample R^2 by permuting the response vector 1,000 times; the empirical P-value equals the fraction of permuted R^2 values greater than or equal to the observed R^2. Model fit was reported as R^2 and its permutation-based P. Non-zero coefficients were retained for downstream interpretation.

Motif-enrichment analysis

For each cell type we extracted 25-bp sequences centred on MPRA-validated expression-modifying variants (emVars). Motif enrichment was assessed with AME v5.5.6 (MEME-Suite) using the HOCOMOCO v12 core mouse–human TF motif collection. Enrichment was calculated with the Wilcoxon rank-sum test (--method ranksum) and average log-odds scoring (--scoring avg); only the top 25 % of motif hits in the target set were considered (--hit-lo-fraction 0.25). The THP-1 emVar sequences served as the control set for brain emVars (and vice-versa) via the --control option. Motifs with an E-value < 10 and Benjamini-Hochberg–adjusted q < 0.05 were deemed significantly enriched.

Machine Learning Model Training and Prediction

Data Preprocessing for Machine Learning

NarrowPeak files of IDR optimal peaks of each cell type were expanded to a uniform width of 500 bp centered on the peak summit. Peak intensities were directly extracted from column 7 of the NarrowPeak files. To create a balanced dataset for machine learning, genomic mononucleotide distribution-matched negative sequences were generated using BiasAway with the command: biasaway g --foreground {foreground} --nfold 1 --bgdirectory {background} --seed 19951124. Each positive sequence was paired with a GC-content matched negative sequence, ensuring no overlap with positive sequences. Signal values for negative sequences were set to zero. The dataset comprising both positive and negative sequences was then partitioned into training, validation, and test sets based on genomic location, assigning sequences from chromosome 4 to the validation set and sequences from chromosomes 8 and 9 to the test set.

Convolutional Neural Network Training

DNA sequences were one-hot encoded into 4x500 matrices and processed using Tensorflow v2.7. The architecture of the neural network comprised sequential layers: “Input, Conv1D, Dropout, Conv1D, Dropout, MaxPooling1D, Flatten, Dense, Dropout, Dense, Dropout, Dense, and Output”. The hyperparameters used are listed in the Supplementary Table 13.

Predicting Chromatin Accessibility Using Machine Learning Models

Candidate sequences, derived from open chromatin peaks, were standardized to 500 bp centered on the peak summit. Peaks from differential analyses were either expanded or trimmed to 500 bp, centered on their middle point. Both forward and reverse complementary sequences of each input were one-hot encoded into 4x500 matrices. These matrices were then fed into the trained convolutional neural network. The model computed the predicted signal value for each input by averaging the peak signals of the forward and reverse complementary sequences.

Model Interpretation

To interpret model predictions at base-pair resolution, we employed SHapley Additive exPlanations (SHAP)[76] on both validation datasets and genomic sequences with genetic

variants. The SHAP values were input in TF-MODISCO-Lite[77] and match TF motifs in the HOCOMOCO V12 Core motif database. The enriched motifs with q value > 0.05 were reported.

Allelic-specific Differences in Predicted ATAC Accessibility and SHAP Contribution Scores

For each candidate variant, we extracted paired 500-bp genomic sequences centered on the variant position, differing solely at the major- or minor-allele nucleotide. Each allele-specific sequence was evaluated using the trained model in both forward and reverse-complement orientations. Strand-specific predictions were averaged to yield a single ATAC-seq accessibility score per allele, and the allelic effect was quantified as the difference between major- and minor-allele scores.

For each allele, we calculated the SHAP contribution score of each nucleotide across the 500-bp region and derived an allelic SHAP contrast by computing the major-minus-minor difference.

To establish a baseline null distribution, we selected GC-matched control sequences from non-peak genomic regions within a held-out validation set, ensuring the central nucleotide matched the major allele of the query candidate variant. We then mutate the central nucleotide to the minor allele nucleotide of the query variant. Differences in predicted accessibility and SHAP scores between these control sequence pairs defined the null distributions, reflecting expected variability in non-functional regions. All differences underwent log10 transformation. The transformed null distributions displayed substantial overlap, whereas candidate SNPs exhibited a marked rightward shift suggestive of functional relevance. Null distributions were modeled using a normal distribution, enabling computation of variant-specific P values. Variants exhibiting P values < 0.1 were prioritized and visualized using a heat map.

Estimating Prediction Uncertainty

To quantify predictive uncertainty, we adopted Monte-Carlo dropout. Specifically, we re-enabled all Dropout layers in the trained CNN and drew 64 stochastic forward passes per input, using 0.3 dropout rate to approximate sampling from the model's posterior. The resulting ensemble of outputs was summarized by the mean prediction as well as its standard deviation, skewness, and kurtosis, providing a principled estimate of both aleatoric and epistemic uncertainty. To quantify the statistical confidence of allele-specific differences in predicted ATAC accessibility, we performed two-sided Wilcoxon signed-rank tests on the 64 Monte-Carlo dropout replicates per allele and controlled the false-discovery rate with Benjamini–Hochberg correction.

CRISPR Interference Experiments

Plasmid Cloning

We constructed a dCas9-KRAB-MeCP2 plasmid by fusing the bipartite dCas9 repressor (Addgene: 122205) with a third-generation lentiviral backbone (Addgene: 83889). Fragments were PCR-amplified using NEB Q5 High-Fidelity DNA Polymerase

and assembled with the NEBuilder HiFi DNA Assembly kit. sgRNA oligonucleotides, synthesized by Eurofins Genomics, were annealed via a thermal cycler and ligated into the direct-capture Perturb-seq sgRNA backbone (Addgene: pBA904), pre-digested with Thermo FastDigest Restriction Enzymes (BstXI and BpuII02I), using NEB T4 DNA Ligase. Assembled plasmids were amplified in NEB 5-alpha competent E. coli and purified with the QIAprep Spin Mini Plasmid Prep kit.

Guide RNA Design

sgRNA spacers, designed to initiate with "G" to optimize mouse U6 promoter activity, targeted the promoters of SEC63, OSTM1, and the enhancer of interest using CRISPick (Broad Institute). Two safe-targeting and one non-targeting sgRNAs were selected from published sources[108,109]. All sgRNA sequences are provided in the Supplementary Table 14.

Lentivirus Production

HIV-based lentiviral particles were produced by transfecting 0.75 × 10^6 HEK293T cells in 2.5 mL DMEM with a total of 3 µg of lentiviral backbone and genome plasmids (Addgene: 12251, 12253, 12259; plasmid ratio 2:1:1:4 µg) using Lipofectamine 3000. Cells were cultured at 37°C for 2-4 days, after which virus-containing supernatants were filtered through a 0.45 µm PVDF filter (Millipore Sigma) and either used immediately or stored at −80°C.

Stable Cell Generation

THP-1 monocytes were infected with dCas9-virus in 1 mL RPMI1640 (10% FBS) containing 10 µg/mL polybrene (0.3 × 10^6 cells per well in a 6-well plate). After 3 days at 37°C, cells were refreshed with new media; on day 4, 15 µg/mL blasticidin was added for selection. Following 2 days of selection, stable cells were expanded in flasks with continued antibiotic maintenance.

Sample Collection for RNA-seq

Stable THP-1 cell lines were differentiated into macrophages via 3 days of PMA treatment followed by 1 day of resting. On day 4, macrophages were treated with or without LPS+IFN-γ for 4 hours, lysed in-plate, and total RNA was extracted for RNA-seq as described previously.

Enhancer-promoter Mapping

Enhancer-promoter mapping with the Activity-by-Contact model

THP-1 enhancer-promoter interactions were predicted with the Activity-by-Contact (ABC) algorithm[80]. All input data (Hi-C, ATAC-seq, and H3K27ac ChIP-seq for resting cells and for cells stimulated 4 h with LPS+IFN-γ) were obtained from the same GEO series, GSE201376 (Reed *et al.*[81], hg19). The publicly supplied 5-kb Hi-C contact matrix was used as-is, whereas the raw ATAC-seq and ChIP-seq FASTQ files were re-processed with the ENCODE ATAC-seq and ChIP-seq pipelines (hg19 alignment, default parameters). ABC scores were computed from the re-processed activity tracks

and the Hi-C contacts, and enhancer-promoter pairs with ABC ≥ 0.02 were retained as putative regulatory links.

Gene-set enrichment of ABC-linked target genes for functional regulatory variants in THP-1 macrophages

functional regulatory variants discovered by MPRA in both resting and LPS+IFN-γ-stimulated THP-1 macrophages were linked to their putative target genes CRISPRi with the ABC map (ABC ≥ 0.02 in either state). The union of genes (13 genes) from the two conditions was analyzed with enrichGO[110] (clusterProfiler v4.16.0) against the Gene Ontology Biological-Process ontology in org.Hs.eg.db. Over-representation was tested with the hypergeometric method and Benjamini-Hochberg correction; terms with adjusted $P < 0.05$ were considered significantly enriched.

Supplementary Information

Supplementary Table 1 | ATAC-seq promoter accessibility in THP-1 cells

Genome-wide differential-accessibility statistics for all promoters (±1 kb from the annotated TSS) profiled in THP-1 monocytes and in macrophages that were unstimulated or stimulated with IFN-β, IFN-γ, or LPS+IFN-γ. For each stimulus-versus-resting comparison, the table lists genomic coordinates, base-mean accessibility, $\log_2$-fold change, Wald statistic, and Benjamini–Hochberg-adjusted *P* value (*padj*).

Supplementary Table 2 | RNA-seq gene-expression profiles in THP-1 cells

Gene-level differential-expression statistics for THP-1 monocytes and macrophages exposed to IFN-β, IFN-γ, or LPS+IFN-γ, alongside the unstimulated macrophage state. For every annotated gene, the table reports transcript ID, gene symbol, base-mean expression, $\log_2$-fold change relative to the baseline, Wald statistic, and Benjamini–Hochberg-adjusted *P* value (*padj*).

Supplementary Table 3 | MPRA oligonucleotide library design

A complete list of all variants and their corresponding oligonucleotides included in the MPRA designed to test regulatory variants associated with LOAD, with functional annotations for every element.

Supplementary Table 4 | Enhancer activity in MPRAs

Enhancer activities for each cis-regulatory element (CRE) measured by MPRA, based on 15 unique barcode replicates per CRE.

Supplementary Table 5 | State-specific enhancer activities in immune-cell MPRAs

Differential enhancer activities in THP-1 macrophages and HMC3 microglia following IFN-β, IFN-γ, or LPS+IFN-γ stimulation, reported as $\log_2$-fold change and false-discovery-rate-adjusted *P* values relative to the resting state.

Supplementary Table 6 | Allelic MPRA effects (emVars)

Allelic activity differences (reference versus alternate) for all effective molecular variants (emVars) identified in the MPRA experiments, including effect size ($\log_2$-fold

change) and *padj*. Log_2-fold changes for major-versus-minor alleles need to be adjusted according to the 'REFALT_Flip' indicator listed in Supplementary Table 3.

Supplementary Table 7 | Motif-shuffled effects in MPRAs
Transcriptional differences of motif-shuffled CREs relative to the corresponding CREs harboring LOAD genetic variants.

Supplementary Table 8 | State-specific allelic effects in MPRAs
Allelic activity differences that are specific to immune stimulation in THP-1 macrophages and HMC3 microglia, with interaction statistics for allele × stimulus effects.

Supplementary Table 9 | Predicted variant effects from machine learning
Allele-specific regulatory impact scores from convolutional neural network (CNN) models and splicing-impact scores from SpliceAI for every variant assayed.

Supplementary Table 10 | Prioritized functional variants across cell types
Integrated list of high-confidence functional regulatory variants in THP-1 macrophages, mouse brain tissue, HMC3 microglia, and HEK293T cells, combining MPRA and computational predictions.

Supplementary Table 11 | ABC promoter–enhancer links for candidate variants
Activity-by-contact (ABC) model results linking candidate variants to putative target promoters in THP-1 macrophages, including ABC scores and genomic coordinates of interacting elements.

Supplementary Table 12 | CRISPRi RNA-seq in THP-1 macrophages
Differential gene-expression statistics from CRISPRi perturbations of candidate regulatory elements or their nearest-gene promoters in THP-1 macrophages, reported as log_2-fold change versus non-targeting control and Benjamini–Hochberg-adjusted *P* values.

Supplementary Table 13 | CNN architecture and training hyper-parameters
Layer-by-layer specification of the convolutional neural network used to predict ATAC-seq accessibility. Table details input shape, layer type, kernel size, stride, number of filters/units, activation function, dropout rate, optimizer, learning-rate schedule, batch size, and training epochs.

Supplementary Table 14 | CRISPRi sgRNA designs
Sequences and genomic targets of all sgRNAs used for enhancer and promoter knock-downs. For each guide RNA we list the target category (enhancer / promoter / non-targeting / safe-targeting), oligo sequences (5′→3′) and spacer sequences.

Data Availability

Illumina sequencing data were deposited in Gene Expression Omnibus (GEO) with the accession number ***.

Code Availability

Scripts for data analysis are available upon request.

Acknowledgement

We thank Spencer Gibson for piloting the Monte Carlo dropout procedure that informed our assessment of model-prediction uncertainty. We are grateful to Jianglin Zhang for validating sysMPRA in gut tissues through molecular imaging that confirmed systemic infection and assay performance. We acknowledge Xiantong Xin's efforts in piloting ATAC-seq of THP-1 monocytes. We also thank Robert van de Weerd for his careful proofreading and constructive feedback on the manuscript.

Author Contributions

Z.C. and **A.P.** conceived the study. **Z.C.** performed all experiments, analyzed the data, and wrote the first draft of the manuscript. **Y.L.** assisted with the MPRA and CRISPRi experiments, cloned CRISPR plasmids and, together with **L.G.**, produced lentiviral vectors. **A.B.** provided ATAC-seq and MPRA protocols and packaged the AAV vectors, and **B.N.P.** supplied training and protocols for AAV injection and brain microdissection. **H.S.** developed and maintained the convolutional-neural-network training pipelines, while **P.H.** advised on chromatin-interaction interpretation. **Z.C., E.R., B.N.P., X.X., D.P., L.T., L.B., W.H., R.T.** and **M.K.** contributed fine-mapped genetic-variant datasets. All authors reviewed and approved the manuscript.

Competing Interests

None.

Funding

This work was supported by Cure Alzheimer's Fund (**ARP**), PA Cure 4100087331 (**ARP**), NIH DP1DA046585 (**ARP**). **B.N.P.** was supported by an NIH F30 pre-doctoral fellowship (F30 DA053020). The funders had no role in study design, data collection and analysis, decision to publish, or preparation of the manuscript.

Reference

1. Rabinovici, G. D. Late-onset Alzheimer Disease. *Contin.: Lifelong Learn. Neurol.* 25, 14–33 (2019).
2. Liu, C.-C., Liu, C.-C., Kanekiyo, T., Xu, H. & Bu, G. Apolipoprotein E and Alzheimer disease: risk, mechanisms and therapy. *Nat. Rev. Neurol.* 9, 106–118 (2013).
3. Wightman, D. P. *et al.* A genome-wide association study with 1,126,563 individuals identifies new risk loci for Alzheimer's disease. *Nat Genet* 53, 1276–1282 (2021).

4. Jansen, I. E. et al. Genome-wide meta-analysis identifies new loci and functional pathways influencing Alzheimer's disease risk. Nat Genet 51, 404–413 (2019).
5. Bellenguez, C. et al. New insights into the genetic etiology of Alzheimer's disease and related dementias. *Nat. Genet.* 54, 412–436 (2022).
6. Kunkle, B. W. et al. Genetic meta-analysis of diagnosed Alzheimer's disease identifies new risk loci and implicates Aβ, tau, immunity and lipid processing. Nat Genet 51, 414–430 (2019).
7. Leng, F. & Edison, P. Neuroinflammation and microglial activation in Alzheimer disease: where do we go from here? *Nat Rev Neurol* 17, 157–172 (2021).
8. Miao, J. et al. Microglia in Alzheimer's disease: pathogenesis, mechanisms, and therapeutic potentials. *Front. Aging Neurosci.* 15, 1201982 (2023).
9. Nimmerjahn, A., Kirchhoff, F. & Helmchen, F. Resting Microglial *Cell*s Are Highly Dynamic Surveillants of Brain Parenchyma in Vivo. *Science* 308, 1314–1318 (2005).
10. Cserép, C. et al. Microglia monitor and protect neuronal function through specialized somatic purinergic junctions. Science 367, 528–537 (2020).
11. Ard, M. D., Cole, G. M., Wei, J., Mehrle, A. P. & Fratkin, J. D. Scavenging of Alzheimer's amyloid β-protein by microglia in culture. *J. Neurosci. Res.* 43, 190–202 (1996).
12. McGeer, P. L., Itagaki, S., Tago, H. & McGeer, E. G. Reactive microglia in patients with senile dementia of the Alzheimer type are positive for the histocompatibility glycoprotein HLA-DR. *Neurosci. Lett.* 79, 195–200 (1987).
13. Bolós, M. et al. Direct Evidence of Internalization of Tau by Microglia In Vitro and In Vivo. *J. Alzheimer's Dis.* 50, 77–87 (2015).
14. Scheiblich, H. et al. Microglia rescue neurons from aggregate-induced neuronal dysfunction and death through tunneling nanotubes. *Neuron* 112, 3106-3125.e8 (2024).
15. Welch, G. M. et al. Neurons burdened by DNA double-strand breaks incite microglia activation through antiviral-like signaling in neurodegeneration. *Sci Adv* 8, eabo4662 (2022).
16. Davalos, D. et al. ATP mediates rapid microglial response to local brain injury in vivo. *Nat. Neurosci.* 8, 752–758 (2005).
17. Muzio, L., Viotti, A. & Martino, G. Microglia in Neuroinflammation and Neurodegeneration: From Understanding to Therapy. *Front. Neurosci.* 15, 742065 (2021).
18. Gao, C., Jiang, J., Tan, Y. & Chen, S. Microglia in neurodegenerative diseases: mechanism and potential therapeutic targets. *Signal Transduct. Target. Ther.* 8, 359 (2023).
19. Sudwarts, A. et al. BIN1 is a key regulator of proinflammatory and neurodegeneration-related activation in microglia. *Mol. Neurodegener.* 17, 33 (2022).
20. Wang, S. et al. TREM2 drives microglia response to amyloid-β via SYK-dependent and -independent pathways. Cell 185, 4153-4169.e19 (2022).

21. Wang, Y. et al. TREM2 Lipid Sensing Sustains the Microglial Response in an Alzheimer's Disease Model. Cell 160, 1061–1071 (2015).
22. Zhong, L. et al. Soluble TREM2 induces inflammatory responses and enhances microglial survival. *J. Exp. Med.* 214, 597–607 (2017).
23. Dourlen, P., Kilinc, D., Landrieu, I., Chapuis, J. & Lambert, J.-C. BIN1 and Alzheimer's disease: the tau connection. *Trends Neurosci.* 48, 349–361 (2025).
24. Ulland, T. K. & Colonna, M. TREM2 — a key player in microglial biology and Alzheimer disease. Nat. Rev. Neurol. 14, 667–675 (2018).
25. Sun, N. et al. Human microglial state dynamics in Alzheimer's disease progression. Cell 186, 4386-4403.e29 (2023).
26. Gazestani, V. et al. Early Alzheimer's disease pathology in human cortex involves transient cell states. Cell 186, 4438-4453.e23 (2023).
27. Ramamurthy, E. et al. Regression convolutional neural network models implicate peripheral immune regulatory variants in the predisposition to Alzheimer's disease. *PLOS Comput. Biol.* 20, e1012356 (2024).
28. Yang, X. et al. Functional characterization of Alzheimer's disease genetic variants in microglia. Nat. Genet. 55, 1735–1744 (2023).
29. Xiong, X. et al. Epigenomic dissection of Alzheimer's disease pinpoints causal variants and reveals epigenome erosion. Cell 186, 4422-4437.e21 (2023).
30. Cooper, Y. A. et al. Functional regulatory variants implicate distinct transcriptional networks in dementia. Science 377, eabi8654 (2022).
31. Bond, M. L. et al. Deciphering the functional impact of Alzheimer's Disease-associated variants in resting and proinflammatory immune cells. *medRxiv* 2024.09.13.24313654 (2024) doi:10.1101/2024.09.13.24313654.
32. Prokopenko, D. et al. Whole-genome sequencing reveals new Alzheimer's disease–associated rare variants in loci related to synaptic function and neuronal development. *Alzheimer's Dement.* 17, 1509–1527 (2021).
33. Dunham, I. et al. An integrated encyclopedia of DNA elements in the human genome. *Nature* 489, 57–74 (2012).
34. Maurano, M. T. et al. Systematic Localization of Common Disease-Associated Variation in Regulatory DNA. Science 337, 1190–1195 (2012).
35. Heinz, S. et al. Effect of natural genetic variation on enhancer selection and function. Nature 503, 487–492 (2013).
36. Kundaje, A. et al. Integrative analysis of 111 reference human epigenomes. Nature 518, 317–330 (2015).
37. Ostuni, R. et al. Latent Enhancers Activated by Stimulation in Differentiated Cells. Cell 152, 157–171 (2013).
38. Umans, B. D. & Gilad, Y. Oxygen-induced stress reveals context-specific gene regulatory effects in human brain organoids. *Genome Res.* gr.280219.124 (2025) doi:10.1101/gr.280219.124.

39. Umans, B. D., Battle, A. & Gilad, Y. Where Are the Disease-Associated eQTLs? *Trends Genet.* 37, 109–124 (2021).
40. Fairfax, B. P. et al. Innate Immune Activity Conditions the Effect of Regulatory Variants upon Monocyte Gene Expression. Science 343, 1246949 (2014).
41. Kribelbauer-Swietek, J. F. et al. Context transcription factors establish cooperative environments and mediate enhancer communication. Nat. Genet. 56, 2199–2212 (2024).
42. Gjoneska, E. et al. Conserved epigenomic signals in mice and humans reveal immune basis of Alzheimer's disease. Nature 518, 365–369 (2015).
43. Nott, A. et al. Brain cell type–specific enhancer–promoter interactome maps and disease-risk association. Science 366, 1134–1139 (2019).
44. Ward, L. D. & Kellis, M. Interpreting noncoding genetic variation in complex traits and human disease. *Nat. Biotechnol.* 30, 1095–1106 (2012).
45. Ernst, J. et al. Genome-scale high-resolution mapping of activating and repressive nucleotides in regulatory regions. Nat. Biotechnol. 34, 1180–1190 (2016).
46. Lee, S. et al. Massively parallel reporter assay investigates shared genetic variants of eight psychiatric disorders. Cell 188, 1409-1424.e21 (2025).
47. Tewhey, R. et al. Direct Identification of Hundreds of Expression-Modulating Variants using a Multiplexed Reporter Assay. Cell 165, 1519–1529 (2016).
48. Siraj, L. et al. Functional dissection of complex and molecular trait variants at single nucleotide resolution. *bioRxiv* 2024.05.05.592437 (2024) doi:10.1101/2024.05.05.592437.
49. Brown, A. R. et al. An in vivo systemic massively parallel platform for deciphering animal tissue-specific regulatory function. *Front. Genet.* 16, 1533900 (2025).
50. Degner, K. N., Bell, J. L., Jones, S. D. & Won, H. Just a SNP away: The future of in vivo massively parallel reporter assay. *Cell Insight* 4, 100214 (2025).
51. Qi, L. S. et al. Repurposing CRISPR as an RNA-Guided Platform for Sequence-Specific Control of Gene Expression. Cell 152, 1173–1183 (2013).
52. Kheradpour, P. & Kellis, M. Systematic discovery and characterization of regulatory motifs in ENCODE TF binding experiments. *Nucleic Acids Res.* 42, 2976–2987 (2013).
53. Zhou, J. & Troyanskaya, O. G. Predicting effects of noncoding variants with deep learning–based sequence model. *Nat. Methods* 12, 931–934 (2015).
54. Avsec, Ž. et al. Effective gene expression prediction from sequence by integrating long-range interactions. Nat. Methods 18, 1196–1203 (2021).
55. Pampari, A. et al. ChromBPNet: bias factorized, base-resolution deep learning models of chromatin accessibility reveal cis-regulatory sequence syntax, transcription factor footprints and regulatory variants. bioRxiv 2024.12.25.630221 (2025) doi:10.1101/2024.12.25.630221.
56. Tu, X. et al. Deep genomic models of allele-specific measurements. bioRxiv 2025.04.09.648060 (2025) doi:10.1101/2025.04.09.648060.

57. Fu, X. et al. A foundation model of transcription across human cell types. Nature 1–9 (2025) doi:10.1038/s41586-024-08391-z.
58. Lawler, A. J. et al. Machine learning sequence prioritization for cell type-specific enhancer design. *eLife* 11, e69571 (2022).
59. Benegas, G., Ye, C., Albors, C., Li, J. C. & Song, Y. S. Genomic Language Models: Opportunities and Challenges. *arXiv* (2024) doi:10.48550/arxiv.2407.11435.
60. Patel, A. et al. DART-Eval: A Comprehensive DNA Language Model Evaluation Benchmark on Regulatory DNA. arXiv (2024) doi:10.48550/arxiv.2412.05430.
61. Avsec, Ž. et al. AlphaGenome: advancing regulatory variant effect prediction with a unified DNA sequence model. bioRxiv 2025.06.25.661532 (2025) doi:10.1101/2025.06.25.661532.
62. Leone, M. J. et al. Combining Machine Learning and Multiplexed, In Situ Profiling to Engineer Cell Type and Behavioral Specificity. bioRxiv 2025.06.20.660790 (2025) doi:10.1101/2025.06.20.660790.
63. Gosai, S. J. et al. Machine-guided design of cell-type-targeting cis-regulatory elements. Nature 634, 1211–1220 (2024).
64. Consortium, A. et al. Rare coding variants in PLCG2, ABI3, and TREM2 implicate microglial-mediated innate immunity in Alzheimer's disease. Nat. Genet. 49, 1373–1384 (2017).
65. Silvin, A. et al. Dual ontogeny of disease-associated microglia and disease inflammatory macrophages in aging and neurodegeneration. *Immunity* 55, 1448-1465.e6 (2022).
66. Goldmann, T. et al. Origin, fate and dynamics of macrophages at central nervous system interfaces. *Nat. Immunol.* 17, 797–805 (2016).
67. Utz, S. G. et al. Early Fate Defines Microglia and Non-parenchymal Brain Macrophage Development. Cell 181, 557-573.e18 (2020).
68. Siret, C. et al. Deciphering the heterogeneity of the Lyve1+ perivascular macrophages in the mouse brain. *Nat. Commun.* 13, 7366 (2022).
69. Varvel, N. H. et al. Replacement of brain-resident myeloid cells does not alter cerebral amyloid-β deposition in mouse models of Alzheimer's disease. J. Exp. Med. 212, 1803–1809 (2015).
70. Wendeln, A.-C. et al. Innate immune memory in the brain shapes neurological disease hallmarks. Nature 556, 332–338 (2018).
71. Thome, A. D. et al. Functional alterations of myeloid cells during the course of Alzheimer's disease. Mol. Neurodegener. 13, 61 (2018).
72. Quiroga, I. Y. et al. Synthetic amyloid beta does not induce a robust transcriptional response in innate immune cell culture systems. *J Neuroinflamm* 19, 99 (2022).
73. Klein, J. C. et al. A systematic evaluation of the design and context dependencies of massively parallel reporter assays. *Nat Methods* 17, 1083–1091 (2020).
74. Nguyen, T. A. et al. High-throughput functional comparison of promoter and

enhancer activities. Genome Res. 26, 1023–1033 (2016).
75. Jones, L. et al. Genetic Evidence Implicates the Immune System and Cholesterol Metabolism in the Aetiology of Alzheimer's Disease. *PLoS ONE* 5, e13950 (2010).
76. Lundberg, S. & Lee, S.-I. A Unified Approach to Interpreting Model Predictions. arXiv (2017) doi:10.48550/arxiv.1705.07874.
77. Shrikumar, A. et al. Technical Note on Transcription Factor Motif Discovery from Importance Scores (TF-MoDISco) version 0.5.6.5. arXiv (2018) doi:10.48550/arxiv.1811.00416.
78. Morabito, S. et al. Single-nucleus chromatin accessibility and transcriptomic characterization of Alzheimer's disease. Nat. Genet. 53, 1143–1155 (2021).
79. Heneka, M. T. et al. Neuroinflammation in Alzheimer disease. *Nat. Rev. Immunol.* 25, 321–352 (2025).
80. Fulco, C. P. et al. Activity-by-contact model of enhancer–promoter regulation from thousands of CRISPR perturbations. Nat. Genet. 51, 1664–1669 (2019).
81. Reed, K. S. M. et al. Temporal analysis suggests a reciprocal relationship between 3D chromatin structure and transcription. *Cell Rep.* 41, 111567 (2022).
82. Rosner, D. et al. The Alzheimer's Disease Risk Genes MS4A4A And MS4A6A Cooperate to Negatively Regulate Trem2 and Microglia states. bioRxiv 2024.11.23.625001 (2024) doi:10.1101/2024.11.23.625001.
83. Deming, Y. et al. The MS4A gene cluster is a key modulator of soluble TREM2 and Alzheimer's disease risk. *Sci. Transl. Med.* 11, (2019).
84. Nott, A. & Holtman, I. R. Genetic insights into immune mechanisms of Alzheimer's and Parkinson's disease. *Front. Immunol.* 14, 1168539 (2023).
85. Novikova, G. et al. Integration of Alzheimer's disease genetics and myeloid genomics identifies disease risk regulatory elements and genes. *Nat Commun* 12, 1610 (2021).
86. Yang, J.-H. et al. Loss of epigenetic information as a cause of mammalian aging. Cell (2023) doi:10.1016/j.cell.2022.12.027.
87. Huang, D. & Ovcharenko, I. Silencer variants are key drivers of gene upregulation in Alzheimer's disease. medRxiv 2025.04.07.25325386 (2025) doi:10.1101/2025.04.07.25325386.
88. He, G. et al. Gamma-secretase activating protein is a therapeutic target for Alzheimer's disease. Nature 467, 95–98 (2010).
89. Cazzaro, S. et al. Slingshot homolog-1–mediated Nrf2 sequestration tips the balance from neuroprotection to neurodegeneration in Alzheimer's disease. *Proc. Natl. Acad. Sci.* 120, e2217128120 (2023).
90. Kaplow, I. M. et al. Inferring mammalian tissue-specific regulatory conservation by predicting tissue-specific differences in open chromatin. *BMC Genom.* 23, 291 (2022).
91. Kaplow, I. M. et al. Relating enhancer genetic variation across mammals to complex phenotypes using machine learning. Science 380, eabm7993 (2023).

92. Zhao, S. et al. A single-cell massively parallel reporter assay detects cell-type-specific gene regulation. Nat. Genet. 55, 346–354 (2023).
93. Lalanne, J.-B. et al. Multiplex profiling of developmental cis-regulatory elements with quantitative single-cell expression reporters. Nat. Methods 21, 983–993 (2024).
94. Buenrostro, J. D., Giresi, P. G., Zaba, L. C., Chang, H. Y. & Greenleaf, W. J. Transposition of native chromatin for fast and sensitive epigenomic profiling of open chromatin, DNA-binding proteins and nucleosome position. Nat. Methods 10, 1213–1218 (2013).
95. Preissl, S. et al. Single-nucleus analysis of accessible chromatin in developing mouse forebrain reveals cell-type-specific transcriptional regulation. Nat. Neurosci. 21, 432–439 (2018).
96. Love, M. I., Huber, W. & Anders, S. Moderated estimation of fold change and dispersion for RNA-seq data with DESeq2. *Genome Biol* 15, 550 (2014).
97. Consortium, R. et al. Partitioning heritability by functional annotation using genome-wide association summary statistics. Nat Genet 47, 1228–1235 (2015).
98. Quinlan, A. R. & Hall, I. M. BEDTools: a flexible suite of utilities for comparing genomic features. *Bioinformatics* 26, 841–842 (2010).
99. Andrews, S. FastQC: A Quality Control Tool for High Throughput Sequence Data. https://www.bioinformatics.babraham.ac.uk/projects/fastqc/ (2010).
100. Dobin, A. et al. STAR: ultrafast universal RNA-seq aligner. Bioinformatics 29, 15–21 (2013).
101. Zhu, A., Ibrahim, J. G. & Love, M. I. Heavy-tailed prior distributions for sequence count data: removing the noise and preserving large differences. Bioinformatics 35, 2084–2092 (2018).
102. Ignatiadis, N., Klaus, B., Zaugg, J. B. & Huber, W. Data-driven hypothesis weighting increases detection power in genome-scale multiple testing. Nat. Methods 13, 577–580 (2016).
103. Ward, L. D. & Kellis, M. HaploReg: a resource for exploring chromatin states, conservation, and regulatory motif alterations within sets of genetically linked variants. Nucleic Acids Res 40, D930–D934 (2012).
104. Auton, A. et al. A global reference for human genetic variation. Nature 526, 68–74 (2015).
105. Cavalcante, R. G. & Sartor, M. A. annotatr: genomic regions in context. Bioinformatics 33, 2381–2383 (2017).
106. Zhbannikov, I. Y., Arbeev, K., Ukraintseva, S. & Yashin, A. I. haploR: an R package for querying web-based annotation tools. *F1000research* 6, 97 (2017).
107. Ashuach, T. et al. MPRAnalyze: statistical framework for massively parallel reporter assays. Genome Biol 20, 183 (2019).
108. Yao, D. et al. Multicenter integrated analysis of noncoding CRISPRi screens. Nat. Methods 21, 723–734 (2024).

109. Replogle, J. M. et al. Combinatorial single-cell CRISPR screens by direct guide RNA capture and targeted sequencing. *Nat Biotechnol* 38, 954–961 (2020).
110. Yu, G., Wang, L.-G., Han, Y. & He, Q.-Y. clusterProfiler: an R Package for Comparing Biological Themes Among Gene Clusters. *OMICS: A J. Integr. Biol.* 16, 284–287 (2012).

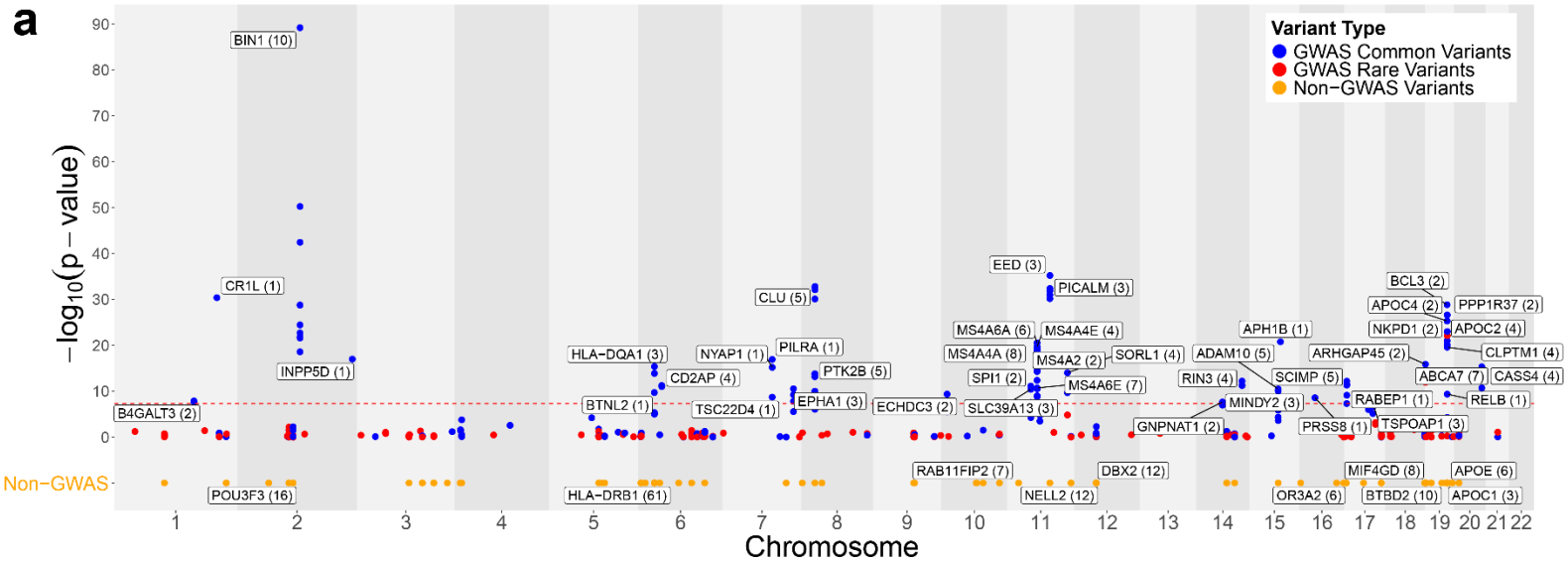
a
Variant Type
GWAS Common Variants
GWAS Rare Variants
Non−GWAS Variants
−log10(p − value)
Non−GWAS
Chromosome
BIN1 (10)
CR1L (1)
INPP5D (1)
B4GALT3 (2)
POU3F3 (16)
HLA−DQA1 (3)
CD2AP (4)
BTNL2 (1)
HLA−DRB1 (61)
NYAP1 (1)
PILRA (1)
PTK2B (5)
CLU (5)
TSC22D4 (1)
EPHA1 (3)
ECHDC3 (2)
EED (3)
PICALM (3)
MS4A6A (6)
MS4A4E (4)
MS4A4A (8)
MS4A2 (2)
SORL1 (4)
SPI1 (2)
MS4A6E (7)
SLC39A13 (3)
RAB11FIP2 (7)
NELL2 (12)
DBX2 (12)
GNPNAT1 (2)
APH1B (1)
ADAM10 (5)
RIN3 (4)
MINDY2 (3)
SCIMP (5)
ARHGAP45 (2)
PRSS8 (1)
OR3A2 (6)
BCL3 (2)
APOC4 (2)
PPP1R37 (2)
NKPD1 (2)
APOC2 (4)
CLPTM1 (4)
ABCA7 (7)
CASS4 (4)
RELB (1)
RABEP1 (1)
TSPOAP1 (3)
MIF4GD (8)
APOE (6)
BTBD2 (10)
APOC1 (3)

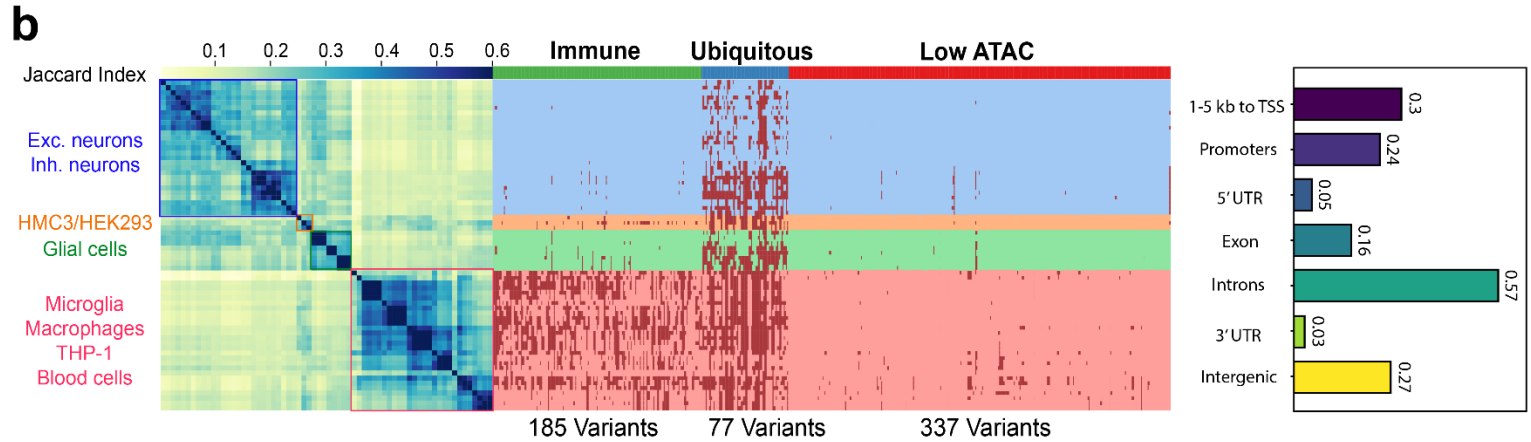
b
Jaccard Index
Immune
Ubiquitous
Low ATAC
Exc. neurons
Inh. neurons
HMC3/HEK293
Glial cells
Microglia
Macrophages
THP-1
Blood cells
185 Variants
77 Variants
337 Variants
1-5 kb to TSS
Promoters
5′UTR
Exon
Introns
3′UTR
Intergenic
0.3
0.24
0.05
0.16
0.57
0.03
0.27

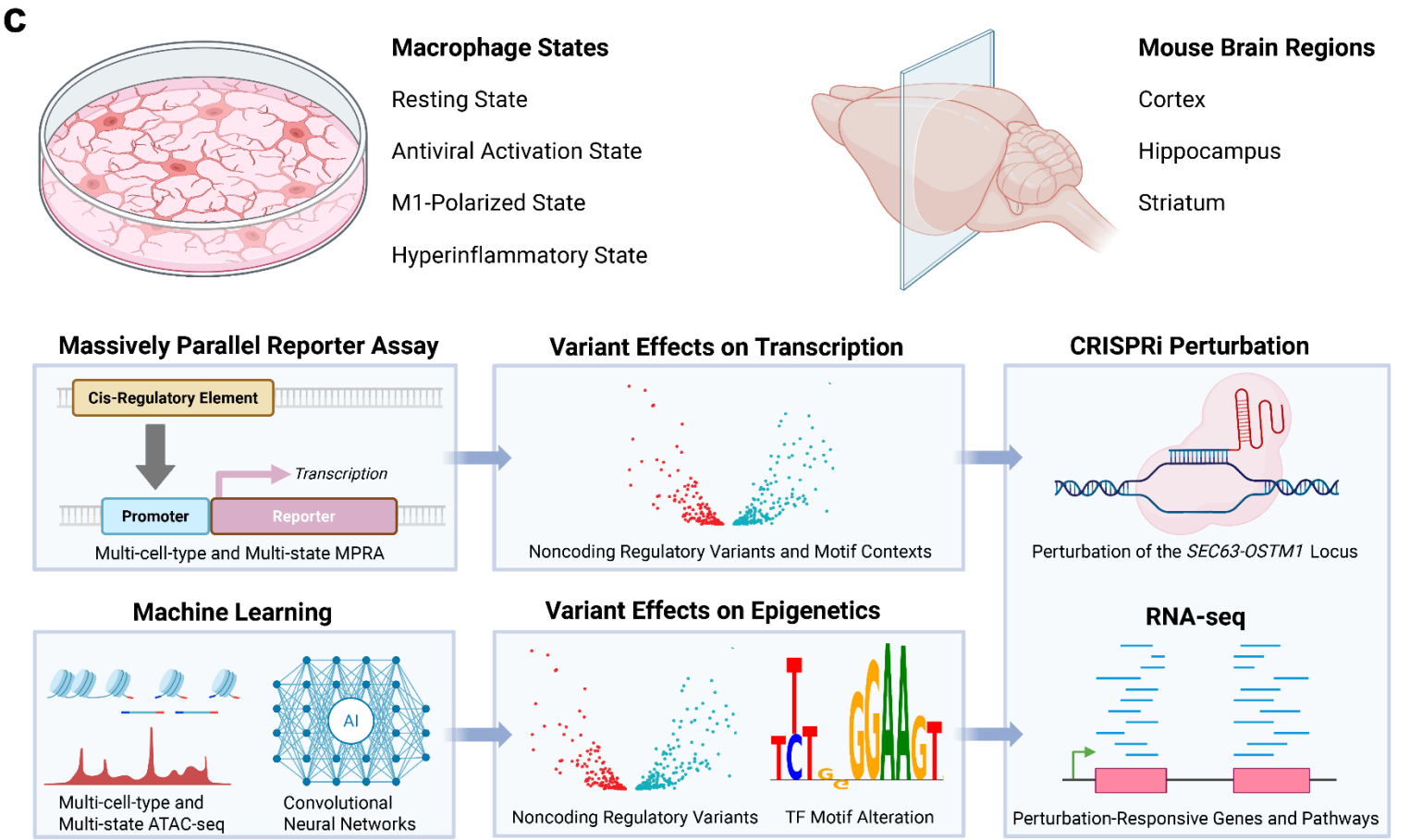
c
Macrophage States
Resting State
Antiviral Activation State
M1-Polarized State
Hyperinflammatory State
Mouse Brain Regions
Cortex
Hippocampus
Striatum
Massively Parallel Reporter Assay
Cis-Regulatory Element
Transcription
Promoter
Reporter
Multi-cell-type and Multi-state MPRA
Variant Effects on Transcription
Noncoding Regulatory Variants and Motif Contexts
CRISPRi Perturbation
Perturbation of the SEC63-OSTM1 Locus
Machine Learning
AI
Multi-cell-type and Multi-state ATAC-seq
Convolutional Neural Networks
Variant Effects on Epigenetics
Noncoding Regulatory Variants
TF Motif Alteration
RNA-seq
Perturbation-Responsive Genes and Pathways

Fig. 1 | Integrative framework for identifying context-dependent regulatory effects of LOAD-associated variants.
(a) Manhattan plot of 599 prioritized late-onset Alzheimer's disease (LOAD) variants, comprising common and rare variants from genome-wide association studies (GWAS) and whole-genome sequencing (WGS) of familial LOAD cases. Variants were selected based on their statistical association strength and overlap with open chromatin regions in brain and immune cell types.
(b) Variants were mapped to regions classified by chromatin accessibility annotations across immune and neuronal cell types and states, derived from bulk and single-nucleus ATAC-seq (Supplementary Table 3), then grouped as immune-specific cis-regulatory elements (CREs), ubiquitously accessible CREs, or regions with low accessibility. The accompanying bar plot summarizes the genomic context of these variants, showing the percentage that fall within 1-5 kb to transcription start site (TSS), promoter, 5' untranslated regions (5' UTR), exons, introns, 3' untranslated regions (3' UTR), and intergenic regions.
(c) Overview of the experimental and computational pipeline for functional interpretation of noncoding variants. Massively parallel reporter assays (MPRAs) in multiple cell types and states validate regulatory activity and motif context. Convolutional neural networks trained on multi-cell-type, multi-state ATAC-seq data identify putative regulatory variants and transcription factor motifs. CRISPRi perturbation of the *SEC63-OSTM1* locus followed by RNA-seq reveals downstream gene expression and pathway changes, linking regulatory variants to LOAD-relevant molecular mechanisms.

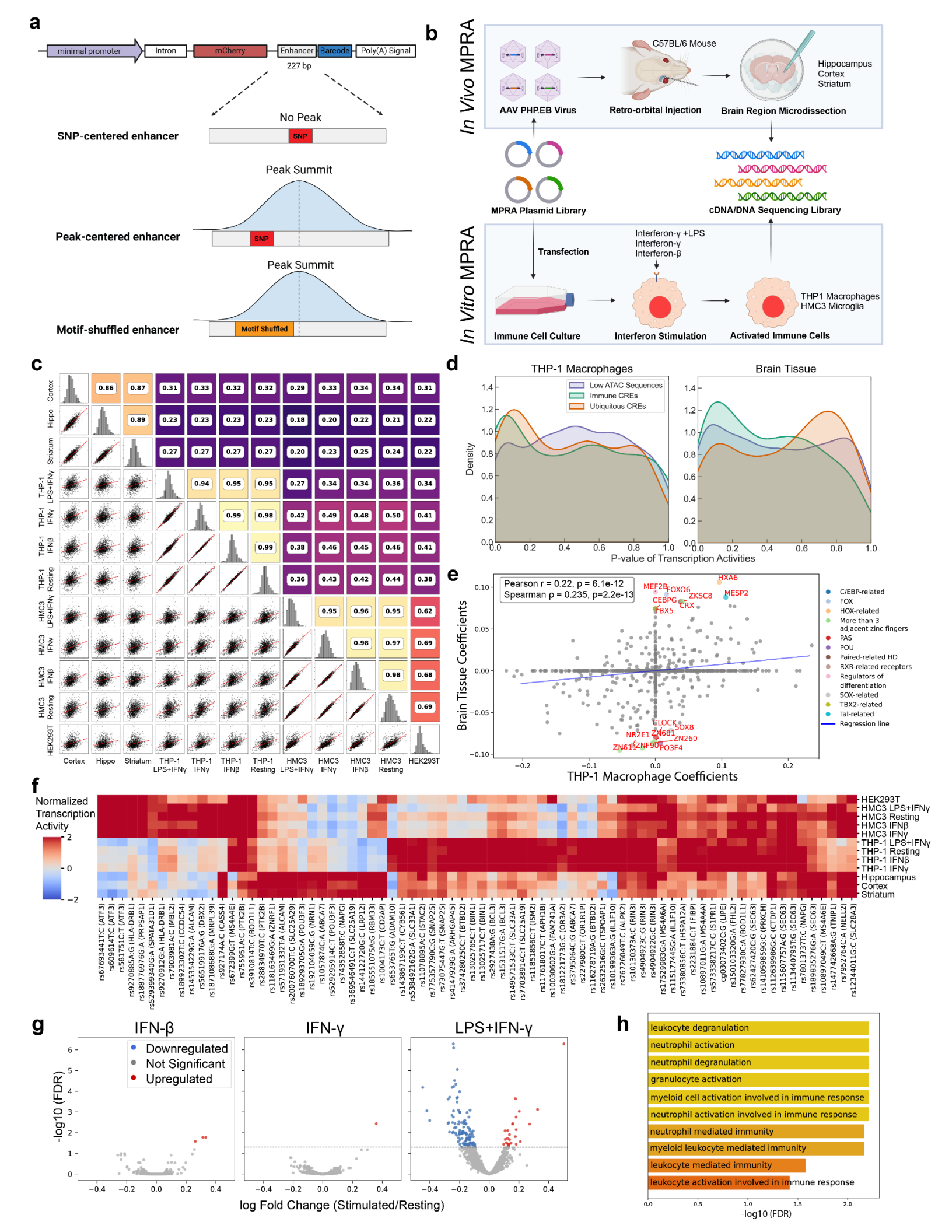
a
minimal promoter
Intron
mCherry
Enhancer
Barcode
Poly(A) Signal
227 bp
SNP-centered enhancer
No Peak
SNP
Peak-centered enhancer
Peak Summit
SNP
Motif-shuffled enhancer
Peak Summit
Motif Shuffled
b
In Vivo MRPA
AAV PHP.EB Virus
C57BL/6 Mouse
Retro-orbital Injection
Hippocampus
Cortex
Striatum
Brain Region Microdissection
MPRA Plasmid Library
cDNA/DNA Sequencing Library
In Vitro MRPA
Transfection
Interferon-γ +LPS
Interferon-γ
Interferon-β
THP1 Macrophages
HMC3 Microglia
Immune Cell Culture
Interferon Stimulation
Activated Immune Cells
c
Cortex
Hippo
Striatum
THP-1 LPS+IFNγ
THP-1 IFNγ
THP-1 IFNβ
THP-1 Resting
HMC3 LPS+IFNγ
HMC3 IFNγ
HMC3 IFNβ
HMC3 Resting
HEK293T
d
THP-1 Macrophages
Brain Tissue
Low ATAC Sequences
Immune CREs
Ubiquitous CREs
Density
P-value of Transcription Activities
e
Pearson r = 0.22, p = 6.1e-12
Spearman ρ = 0.235, p=2.2e-13
Brain Tissue Coefficients
THP-1 Macrophage Coefficients
HXA6
MEF2B
FOXO6
ZKSC8
MESP2
CEBPG
CRX
TBX5
CLOCK
SOX8
NR2E1
ZN681
ZN260
ZN611
ZNF90
PO3F4
C/EBP-related
FOX
HOX-related
More than 3 adjacent zinc fingers
PAS
POU
Paired-related HD
RXR-related receptors
Regulators of differentiation
SOX-related
TBX2-related
Tal-related
Regression line
f
Normalized Transcription Activity
HEK293T
HMC3 LPS+IFNγ
HMC3 Resting
HMC3 IFNβ
HMC3 IFNγ
THP-1 LPS+IFNγ
THP-1 Resting
THP-1 IFNβ
THP-1 IFNγ
Hippocampus
Cortex
Striatum
g
IFN-β
IFN-γ
LPS+IFN-γ
Downregulated
Not Significant
Upregulated
-log10 (FDR)
log Fold Change (Stimulated/Resting)
h
leukocyte degranulation
neutrophil activation
neutrophil degranulation
granulocyte activation
myeloid cell activation involved in immune response
neutrophil activation involved in immune response
neutrophil mediated immunity
myeloid leukocyte mediated immunity
leukocyte mediated immunity
leukocyte activation involved in immune response
-log10 (FDR)

Fig. 2 | Context-dependent MPRA identified LOAD-risk enhancers across neuronal and immune contexts.

(a) Schematic of the massively parallel reporter assay (MPRA) design. Synthetic 227-bp candidate cis-regulatory elements (CREs) downstream of a minimal promoter that drives the expression of mCherry, each tagged with unique barcodes for quantification. CREs were either open chromatin peak-centered on or variant-centered, with additional motif-disrupted constructs generated by sequence shuffling around selected variants

(b) Reporter libraries were systemically delivered *in vivo* to the mouse brain tissues (cortex, hippocampus, and striatum) via AAV.PHP.eB viral retro-orbital injection, and transfected *in vitro* into THP-1 macrophages and HMC3 microglia-like cells under resting, IFN-β, IFN-γ, and LPS+IFN-γ conditions.

(c) CRE enhancer activities show both cell-type- and immune-state-specific patterns. MPRA activity is quantified using cDNA:DNA ratios and modeled via median absolute deviation (MAD) scores (MPRAnalyze quantitative analysis, see methods). MAD scores reveal strong correlations among similar cell types and conditions (Pearson correlation), whereas LPS+IFN-γ stimulation yields more distinct activity profiles and lower correlations with other immune states. This figure mixes scatter plots, histograms of MAD scores, and a heatmap of MAD score correlations.

(d) Immune and ubiquitous CREs (defined in Fig. 1b) exhibit higher activity in THP-1 macrophages, and immune CREs also display elevated activity in brain tissue (P.MAD, MPRAnalyze quantitative analysis).

(e) Coefficients of HOCOMOCO transcription factor motifs in elastic net models that predict MAD scores of THP-1 macrophage MPRA or brain tissue MPRA. Regression outliers highlighted in red have residuals greater than 3-fold the standard deviation.

(f) Clustering of cell-type-specific and broadly active enhancers. The heatmap depicts Z-normalized reporter transcription activity for each candidate CRE (columns) across the assayed cell types/conditions (rows). For every enhancer, reporter activity was quantified as the mean MAD score of its reference and alternate-allele constructs, then standardized within each cell type by dividing by that cell type's standard deviation to yield a Z-score. Only enhancers with $|Z| \geq 1.65$ (≈ 95th percentile) in at least one context are shown, highlighting elements with strong cell-type-specific or broadly shared activity. Unsupervised hierarchical clustering (Euclidean distance, average linkage) organizes both enhancers and cell types; warmer colors indicate higher activity and cooler colors lower activity.

(g) CRE responses to LPS+IFN-γ stimulation in THP-1 macrophages; most responsive CREs exhibit repression upon stimulation (FDR < 0.05, MPRAnalyze comparative analysis, see methods). Volcano plots show the log fold change of CRE enhancer activities in stimulated THP-1 macrophages versus resting THP-1 macrophages at the X-axis and -log10 (FDR) at the Y-axis.

(h) Genes proximal to LPS+IFN-γ-responsive CREs enriched in immune activation pathways (FDR < 0.05, fast gene set enrichment analysis).

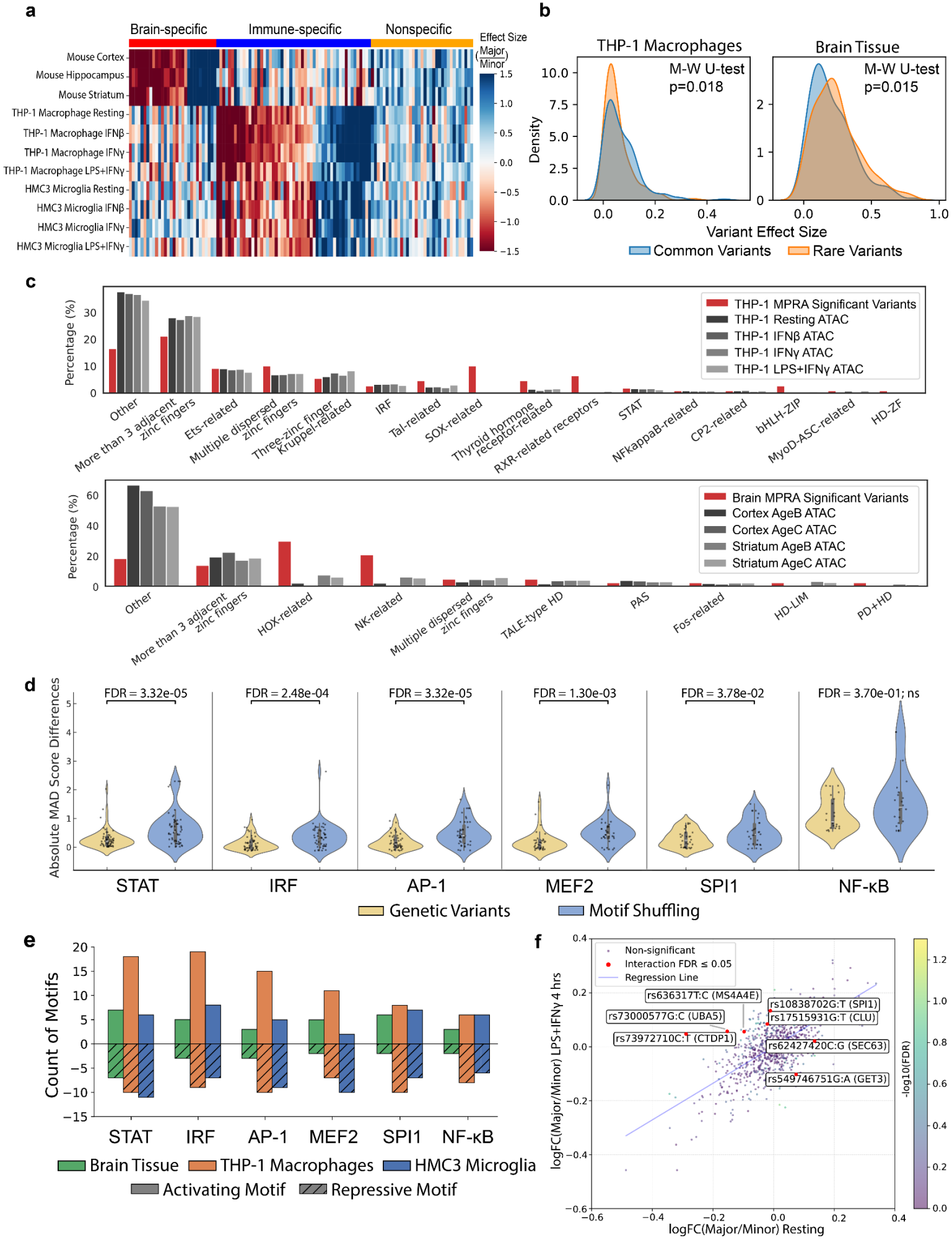
a
Brain-specific
Immune-specific
Nonspecific
Effect Size (Major/Minor)
Mouse Cortex
Mouse Hippocampus
Mouse Striatum
THP-1 Macrophage Resting
THP-1 Macrophage IFNβ
THP-1 Macrophage IFNγ
THP-1 Macrophage LPS+IFNγ
HMC3 Microglia Resting
HMC3 Microglia IFNβ
HMC3 Microglia IFNγ
HMC3 Microglia LPS+IFNγ
b
THP-1 Macrophages
M-W U-test p=0.018
Brain Tissue
M-W U-test p=0.015
Density
Variant Effect Size
Common Variants
Rare Variants
c
Percentage (%)
THP-1 MPRA Significant Variants
THP-1 Resting ATAC
THP-1 IFNβ ATAC
THP-1 IFNγ ATAC
THP-1 LPS+IFNγ ATAC
Other
More than 3 adjacent zinc fingers
Ets-related
Multiple dispersed zinc fingers
Three-zinc finger Kruppel-related
IRF
Tal-related
SOX-related
Thyroid hormone receptor-related
RXR-related receptors
STAT
NFkappaB-related
CP2-related
bHLH-ZIP
MyoD-ASC-related
HD-ZF
Brain MPRA Significant Variants
Cortex AgeB ATAC
Cortex AgeC ATAC
Striatum AgeB ATAC
Striatum AgeC ATAC
HOX-related
NK-related
TALE-type HD
PAS
Fos-related
HD-LIM
PD+HD
d
Absolute MAD Score Differences
FDR = 3.32e-05
FDR = 2.48e-04
FDR = 3.32e-05
FDR = 1.30e-03
FDR = 3.78e-02
FDR = 3.70e-01; ns
STAT
IRF
AP-1
MEF2
SPI1
NF-κB
Genetic Variants
Motif Shuffling
e
Count of Motifs
STAT
IRF
AP-1
MEF2
SPI1
NF-κB
Brain Tissue
THP-1 Macrophages
HMC3 Microglia
Activating Motif
Repressive Motif
f
Non-significant
Interaction FDR ≤ 0.05
Regression Line
rs636317T:C (MS4A4E)
rs10838702G:T (SPI1)
rs73000577G:C (UBA5)
rs17515931G:T (CLU)
rs73972710C:T (CTDP1)
rs62427420C:G (SEC63)
rs549746751G:A (GET3)
logFC(Major/Minor) LPS+IFNγ 4 hrs
logFC(Major/Minor) Resting
-log10(FDR)

Fig. 3 | Allele frequency, cellular context, and immune state modulate TF-motif-driven variant effects on enhancer activity.

(a) Clustering of LOAD variants with significant impacts (FDR < 0.05, MPRAnalyze comparative analysis) on active enhancers (P.MAD < 0.1, MPRA quantitative analysis). Brain-specific, immune-specific, and nonspecific effects were observed.

(b) Comparison of MPRA-derived effect sizes between rare (minor allele frequency [MAF] < 0.01) and common (MAF ≥ 0.29) variants in THP-1 macrophages and mouse brain tissue. Common variants exert stronger effects in macrophages, whereas rare variants show greater transcriptional consequences in the brain (P-value, one-tailed Mann-Whitney U test).

(c) TF motif-enrichment of the sequence context around significant expression-modifying variants (emVars) highlights distinct TF families in each cell type. Motif analysis was performed using AME (MEME Suite) to identify TF families enriched in the 25 bp sequence context surrounding MPRA-validated emVars (q < 0.05), separately for each cell type. Results are compared to motif enrichment in cell-type-specific ATAC-seq peaks from THP-1 macrophages and brain tissues (Cortex and Striatum). Similar TF family enrichment patterns were observed in both datasets, with cell-type-specific TFs identified in ATAC-seq showing comparable enrichment around MPRA-significant variants in the corresponding cell type.

(d) Comparison of CRE enhancer activities between constructs harboring single-nucleotide variants and those with shuffled motif sequences. Motif disruption causes significantly stronger transcriptional perturbations than SNVs in several key transcription factor (TF) families, including STAT, IRF, AP-1, MEF2, and SPI1 (FDR ≤ 0.05, one-tailed Wilcoxon signed-rank test). ns, not significant (FDR > 0.05)

(e) Disrupted motif contexts show directional regulatory effects: disruptions that decreased transcription mark the motif as an activator, whereas disruptions that increased transcription mark it as a repressor. Motifs such as IRF, SPI1, and STAT often correlate with increased transcriptional activity, suggesting their roles as activating factors.

(f) Variants exhibit distinct transcriptional responses under hyperinflammatory state (LPS+IFN-γ) (FDR < 0.05, MPRAnalyze comparative analysis). The Y and X axes represent the log fold change of CRE enhancer activities of the major allele versus the minor allele in LPS+IFN-γ-treated and resting THP-1 macrophages, respectively.

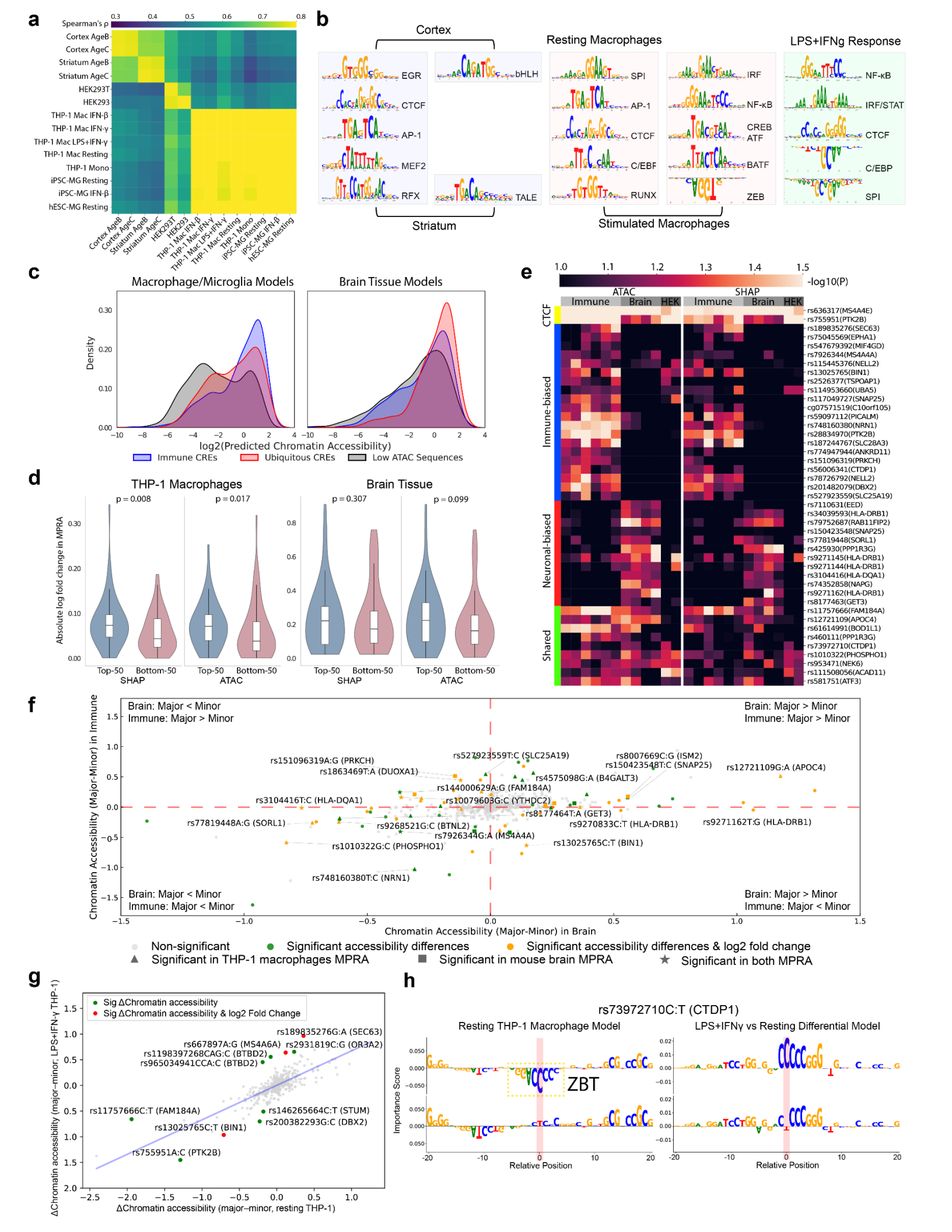
a
Spearman's ρ
0.3 0.4 0.5 0.6 0.7 0.8
Cortex AgeB
Cortex AgeC
Striatum AgeB
Striatum AgeC
HEK293T
HEK293
THP-1 Mac IFN-β
THP-1 Mac IFN-γ
THP-1 Mac LPS+IFN-γ
THP-1 Mac Resting
THP-1 Mono
iPSC-MG Resting
iPSC-MG IFN-β
hESC-MG Resting
b
Cortex
Resting Macrophages
LPS+IFNg Response
EGR
bHLH
CTCF
AP-1
MEF2
RFX
TALE
SPI
IRF
NF-κB
CREB
ATF
C/EBF
BATF
RUNX
ZEB
IRF/STAT
C/EBP
Striatum
Stimulated Macrophages
c
Macrophage/Microglia Models
Brain Tissue Models
Density
log2(Predicted Chromatin Accessibility)
Immune CREs
Ubiquitous CREs
Low ATAC Sequences
d
THP-1 Macrophages
Brain Tissue
p = 0.008
p = 0.017
p = 0.307
p = 0.099
Absolute log fold change in MPRA
Top-50
Bottom-50
SHAP
ATAC
e
-log10(P)
ATAC
SHAP
Immune
Brain
HEK
CTCF
Immune-biased
Neuronal-biased
Shared
rs636317(MS4A4E)
rs755951(PTK2B)
rs189835276(SEC63)
rs75045569(EPHA1)
rs547679392(MIF4GD)
rs7926344(MS4A4A)
rs115445376(NELL2)
rs13025765(BIN1)
rs2526377(TSPOAP1)
rs114953660(UBA5)
rs117049727(SNAP25)
cg07571519(C10orf105)
rs59097112(PICALM)
rs748160380(NRN1)
rs28834970(PTK2B)
rs187244767(SLC28A3)
rs774947944(ANKRD11)
rs151096319(PRKCH)
rs56006341(CTDP1)
rs78726792(NELL2)
rs201482079(DBX2)
rs527923559(SLC25A19)
rs7110631(EED)
rs34039593(HLA-DRB1)
rs79752687(RAB11FIP2)
rs150423548(SNAP25)
rs77819448(SORL1)
rs425930(PPP1R3G)
rs9271145(HLA-DRB1)
rs9271144(HLA-DRB1)
rs3104416(HLA-DQA1)
rs74352858(NAPG)
rs9271162(HLA-DRB1)
rs8177463(GET3)
rs11757666(FAM184A)
rs12721109(APOC4)
rs61614991(BOD1L1)
rs460111(PPP1R3G)
rs73972710(CTDP1)
rs1010322(PHOSPHO1)
rs953471(NEK6)
rs111508056(ACAD11)
rs581751(ATF3)
f
Brain: Major < Minor
Immune: Major > Minor
Brain: Major > Minor
Immune: Major > Minor
Brain: Major < Minor
Immune: Major < Minor
Brain: Major > Minor
Immune: Major < Minor
rs151096319A:G (PRKCH)
rs1863469T:A (DUOXA1)
rs527923559T:C (SLC25A19)
rs8007669C:G (ISM2)
rs150423548T:C (SNAP25)
rs12721109G:A (APOC4)
rs4575098G:A (B4GALT3)
rs1440006629A:G (FAM184A)
rs3104416T:C (HLA-DQA1)
rs10079603G:C (YTHDC2)
rs8177464T:A (GET3)
rs77819448A:G (SORL1)
rs9268521G:C (BTNL2)
rs9270833C:T (HLA-DRB1)
rs9271162T:G (HLA-DRB1)
rs7926344G:A (MS4A4A)
rs1010322G:C (PHOSPHO1)
rs13025765C:T (BIN1)
rs748160380T:C (NRN1)
Chromatin Accessibility (Major-Minor) in Immune
Chromatin Accessibility (Major-Minor) in Brain
Non-significant
Significant accessibility differences
Significant accessibility differences & log2 fold change
Significant in THP-1 macrophages MPRA
Significant in mouse brain MPRA
Significant in both MPRA
g
Sig ΔChromatin accessibility
Sig ΔChromatin accessibility & log2 Fold Change
rs189835276G:A (SEC63)
rs667897A:G (MS4A6A)
rs2931819C:G (OR3A2)
rs1198397268CAG:C (BTBD2)
rs965034941CCA:C (BTBD2)
rs11757666C:T (FAM184A)
rs146265664C:T (STUM)
rs200382293G:C (DBX2)
rs13025765C:T (BIN1)
rs755951A:C (PTK2B)
ΔChromatin accessibility (major–minor, LPS+IFN-γ THP-1)
ΔChromatin accessibility (major–minor, resting THP-1)
h
rs73972710C:T (CTDP1)
Resting THP-1 Macrophage Model
LPS+IFNγ vs Resting Differential Model
ZBT
Importance Score
Relative Position

Fig. 4 | Machine-learning models interpret cell-type- and state-specific regulatory effects of LOAD variants.

(a) Convolutional neural network (CNN) models are trained on ATAC-seq data from multiple immune and neuronal cell types and states to predict chromatin accessibility. These models achieve high accuracy on closely related cell types (Spearman's $\rho \approx 0.8$) and moderate performance across more divergent types ($\rho \approx 0.5$), indicating context specificity.

(b) TF-MoDISco motif analysis identifies cell-type- and state-specific transcription factor (TF) motifs based on SHAP importance scores from each model's predictions (q-value < 0.05). These motifs form combinatorial modules that collectively yield distinct regulatory signatures.

(c) Models trained in immune versus neuronal contexts differentially predict accessibility of LOAD variant-containing sequences, distinguishing immune-specific, ubiquitous, and low-accessibility regions. Predictions from different models are aggregated: macrophage/microglia models (THP-1 macrophages, iPSC-derived microglia, and hESC-derived microglia) and brain-region models (cortex and striatum).

(d) The 50 variants predicted to most strongly alter chromatin accessibility induce markedly larger transcriptional changes in MPRA than the 50 variants predicted to have minimal impact (one-tailed Wilcoxon rank-sum test).

(e) Integrating predicted accessibility and SHAP scores identifies top variants that disrupt CTCF motifs or exert immune-specific and neuron-specific effects. P-values calculated based on differences in predicted chromatin accessibility and SHAP values between major and minor alleles relative to cell-type-specific null distributions.

(f) Linear regression of allele-specific effect sizes across paired cell-type models pinpoints variants with significant cell-type-selective activity (FDR < 0.05). Two patterns emerge: (i) *magnitude-shift* variants exert the same directional effect in immune and neuronal cells but with different strengths, and (ii) *direction-switch* variants flip between activation and repression across the two lineages. emVars detected in THP-1 macrophage MPRA, brain MPRA, or both are annotated with triangles, squares, and asterisks, respectively.

(g) Linear regression of allelic effect sizes in immune-state-specific models shows variants with enhanced or diminished regulatory effects in the hyperinflammatory state (LPS+IFN-γ, FDR < 0.05).

(h) Condition-specific regulatory variants. rs73972710 (C:T) at *CTDP1*—the major C allele forms a repressive ZBTB-family motif that dampens transcription in resting cells, whereas the T allele disrupts the motif and lifts repression. Under hyperinflammatory conditions, chromatin opening around the major allele masks its resting-state repression, reducing allelic differences. SHAP logos visualize the motif gains and losses that drive these state-specific effects.

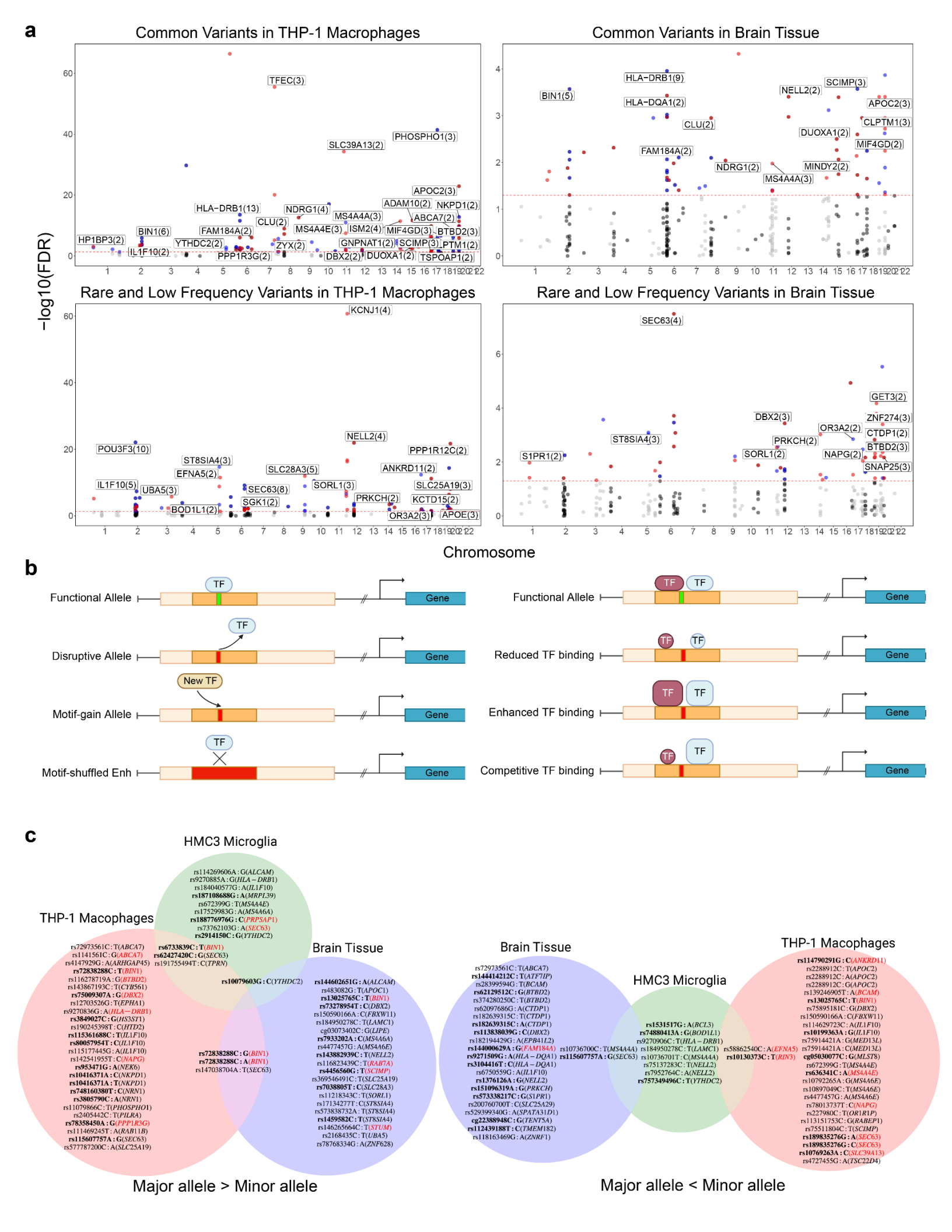
a
Common Variants in THP-1 Macrophages
Common Variants in Brain Tissue
Rare and Low Frequency Variants in THP-1 Macrophages
Rare and Low Frequency Variants in Brain Tissue
−log10(FDR)
Chromosome
TFEC(3)
PHOSPHO1(3)
SLC39A13(2)
APOC2(3)
ADAM10(2)
NKPD1(2)
HLA−DRB1(13)
NDRG1(4)
MS4A4A(3)
ABCA7(2)
CLU(2)
MS4A4E(3)
ISM2(4)
MIF4GD(3)
BTBD2(3)
BIN1(6)
FAM184A(2)
HP1BP3(2)
YTHDC2(2)
GNPNAT1(2)
SCIMP(3)
PTM1(2)
IL1F10(2)
ZYX(2)
PPP1R3G(2)
DBX2(2)
DUOXA1(2)
TSPOAP1(2)
HLA−DRB1(9)
SCIMP(3)
NELL2(2)
BIN1(5)
HLA−DQA1(2)
APOC2(3)
CLU(2)
CLPTM1(3)
DUOXA1(2)
MIF4GD(2)
FAM184A(2)
NDRG1(2)
MINDY2(2)
MS4A4A(3)
KCNJ1(4)
NELL2(4)
POU3F3(10)
PPP1R12C(2)
ST8SIA4(3)
EFNA5(2)
SLC28A3(5)
ANKRD11(2)
IL1F10(5)
UBA5(3)
SEC63(8)
SORL1(3)
SLC25A19(3)
SGK1(2)
PRKCH(2)
KCTD15(2)
BOD1L1(2)
OR3A2(3)
APOE(3)
SEC63(4)
GET3(2)
DBX2(3)
ZNF274(3)
OR3A2(2)
CTDP1(2)
ST8SIA4(3)
PRKCH(2)
BTBD2(3)
S1PR1(2)
SORL1(2)
NAPG(2)
SNAP25(3)
b
Functional Allele
Disruptive Allele
Motif-gain Allele
Motif-shuffled Enh
Reduced TF binding
Enhanced TF binding
Competitive TF binding
TF
New TF
Gene
c
HMC3 Microglia
THP-1 Macophages
Brain Tissue
rs114269606A : G(ALCAM)
rs9270885A : G(HLA − DRB1)
rs184040577G : A(IL1F10)
rs187108688G : A(MRPL39)
rs672399G : T(MS4A4E)
rs17529983G : A(MS4A6A)
rs188776976G : C(PRPSAP1)
rs73762103G : A(SEC63)
rs2914150C : G(YTHDC2)
rs72973561C : T(ABCA7)
rs1141561C : G(ABCA7)
rs4147929G : A(ARHGAP45)
rs72838288C : T(BIN1)
rs116278719A : G(BTBD2)
rs143867193C : T(CYB561)
rs75009307A : G(DBX2)
rs12703526G : T(EPHA1)
rs9270836G : A(HLA−DRB1)
rs3849027C : G(HS3ST1)
rs190245398T : C(HTD2)
rs115361688C : T(IL1F10)
rs80057954T : C(IL1F10)
rs115177445G : A(IL1F10)
rs142541955T : C(NAPG)
rs953471G : A(NEK6)
rs10416371A : C(NKPD1)
rs10416371A : T(NKPD1)
rs748160380T : C(NRN1)
rs3805790C : A(NRN1)
rs11079866C : T(PHOSPHO1)
rs2405442C : T(PILRA)
rs78358450A : G(PPP1R3G)
rs111469245T : A(RAB11B)
rs115607757A : G(SEC63)
rs577787200C : A(SLC25A19)
rs6733839C : T(BIN1)
rs62427420C : G(SEC63)
rs191755494T : C(TPRN)
rs10079603G : C(YTHDC2)
rs72838288C : G(BIN1)
rs72838288C : A(BIN1)
rs147038704A : T(SEC63)
rs144602651G : A(ALCAM)
rs483082G : T(APOC1)
rs13025765C : T(BIN1)
rs73278954T : C(DBX2)
rs150590166A : C(FBXW11)
rs184950278C : T(LAMC1)
cg03073402C : G(LIPE)
rs7933202A : C(MS4A6A)
rs4477457G : A(MS4A6E)
rs143882939C : T(NELL2)
rs116823439C : T(RAB7A)
rs4456560G : T(SCIMP)
rs369546491C : T(SLC25A19)
rs7038805T : C(SLC28A3)
rs11218343C : T(SORL1)
rs17134277T : C(ST8SIA4)
rs573838732A : T(ST8SIA4)
rs1459582C : T(ST8SIA4)
rs146265664C : T(STUM)
rs2168435C : T(UBA5)
rs78768334G : A(ZNF628)
rs72973561C : T(ABCA7)
rs144414212C : T(ATF7IP)
rs283399594G : T(BCAM)
rs62129512C : G(BTBD2)
rs374280250C : T(BTBD2)
rs62097686G : A(CTDP1)
rs182639315C : T(CTDP1)
rs182639315C : A(CTDP1)
rs113838039G : C(DBX2)
rs182194429G : A(EPB41L2)
rs144000629A : G(FAM184A)
rs9271509G : A(HLA − DQA1)
rs3104416T : C(HLA − DQA1)
rs6750559G : A(IL1F10)
rs1376126A : G(NELL2)
rs151096319A : G(PRKCH)
rs573338217C : G(S1PR1)
rs200760700T : C(SLC25A29)
rs529399340G : A(SPATA31D1)
cg22388948C : G(TEN7SA)
rs112439188T : C(TMEM182)
rs118163469G : A(ZNRF1)
rs10736700C : T(MS4A4A)
rs115607757A : G(SEC63)
rs1531517G : A(BCL3)
rs74880413A : G(BOD1L1)
rs9270906C : T(HLA − DRB1)
rs184950278C : T(LAMC1)
rs10736701T : C(MS4A4A)
rs75137283C : T(NELL2)
rs7952764C : A(NELL2)
rs757349496C : T(YTHDC2)
rs58862540C : A(EFNA5)
rs10130373C : T(RIN3)
rs114790291G : C(ANKRD11)
rs2288912C : T(APOC2)
rs2288912C : A(APOC2)
rs2288912C : G(APOC2)
rs139246905T : A(BCAM)
rs13025765C : T(BIN1)
rs75895181C : G(DBX2)
rs150590166A : C(FBXW11)
rs114629723C : A(IL1F10)
rs10199363A : G(IL1F10)
rs75914421A : G(MED13L)
rs75914421A : C(MED13L)
cg05030077C : G(MLST8)
rs672399G : T(MS4A4E)
rs636341C : A(MS4A4E)
rs10792265A : G(MS4A6E)
rs10897049C : T(MS4A6E)
rs4477457G : A(MS4A6E)
rs78013737T : C(NAPG)
rs227980C : T(OR1R1P)
rs113151753C : G(RABEP1)
rs75511804C : T(SCIMP)
rs189835276G : A(SEC63)
rs189835276G : C(SEC63)
rs10769263A : C(SLC39A13)
rs4727455G : A(TSC22D4)
Major allele > Minor allele
Major allele < Minor allele

Fig. 5 | Functional regulatory variants.
(a) Genome-wide map of rare, low-frequency, and common expression-modifying variants (emVars) that simultaneously perturb transcription (MPRA) and chromatin accessibility (model predictions). Spatial clustering of these dual-effect alleles marks convergent regulatory hotspots, loci harboring multiple functionally active variants. Dots are colored by the direction of the transcriptional effect (red, minor < major; blue, minor > major). Variants shown satisfy FDR < 0.05 in the MPRA allelic comparison, and $|\log_2 FC| > 0.1$ and FDR < 0.01 in predicted accessibility differences.
(b) Proposed mechanistic model illustrating how genetic variants modulate transcription via multiple mechanisms. Variants can disrupt or create transcription factor (TF) motifs, alter local TF binding affinity, or influence competitive interactions among TFs, collectively shaping transcriptional output. Motif shuffling abolishes local TF binding, clarifying variant mechanisms.
(c) Criteria-based selection of functional causal variants from MPRA data, categorized by higher or lower transcriptional activity of the major allele relative to the minor allele in THP-1 macrophages, HMC3 microglia-like cells, and mouse brain. Red: variants supported by motif shuffling. Bold: variants predicted to significantly alter chromatin accessibility (FDR < 0.01, two-tailed Wilcoxon signed-rank test on Bayesian predictions using Monte Carlo dropout; logFC accessibility difference magnitude > 0.1).

a

Variant	Locus	THP-1 Macrophages	Brain Tissue	HMC3 Microglia
rs6733839	BIN1	C>T		C>T
rs13025717	BIN1	C>T		
rs13025765	BIN1	C<T	C>T	
rs72838288	BIN1	C>D	C<D	C>D
rs10897049	MS4A6E	C<T		C<T
rs4477457	MS4A6E	G>A	G<A	
rs10792265	MS4A6E	A<G		
rs147038704	SEC63-OSTM1	A>T	A>T	
rs115607757	SEC63-OSTM1	A>G	A<G	A<G
rs189835276	SEC63-OSTM1	G<M	G<M	G<C
rs62427420	SEC63-OSTM1	C>G		C>G

b

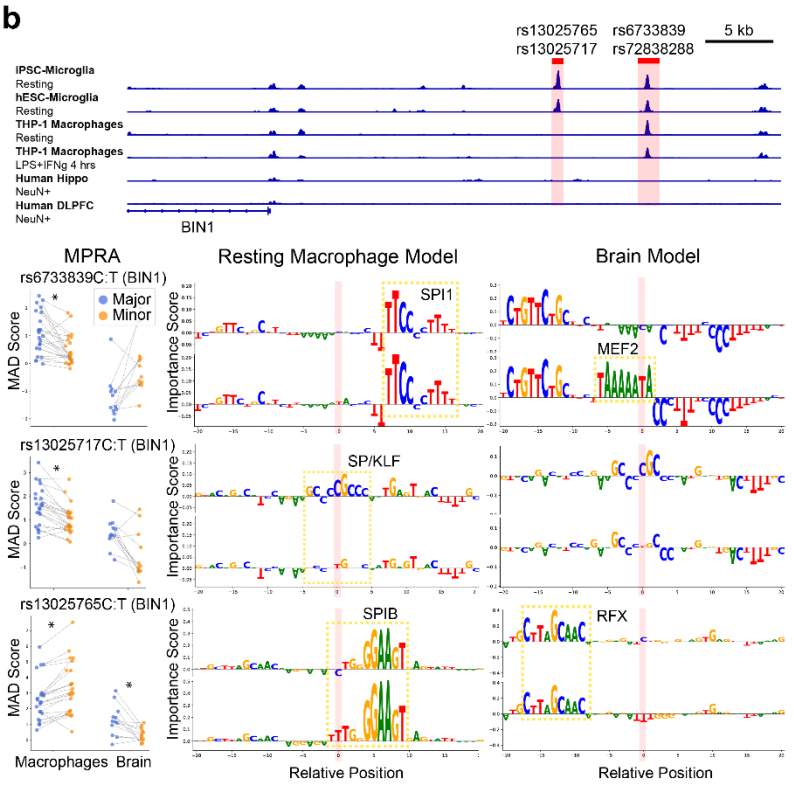

c

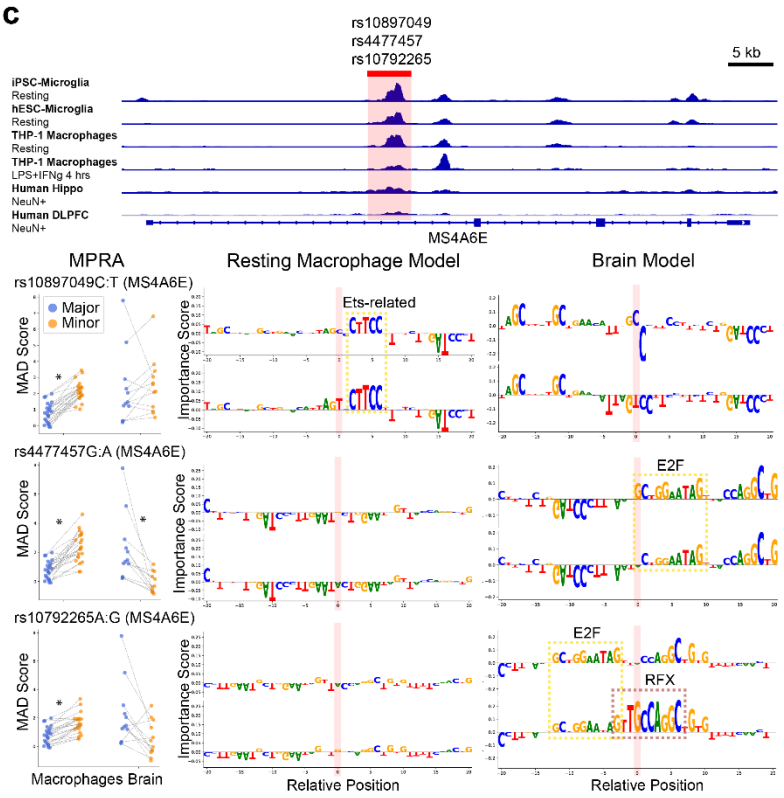

d

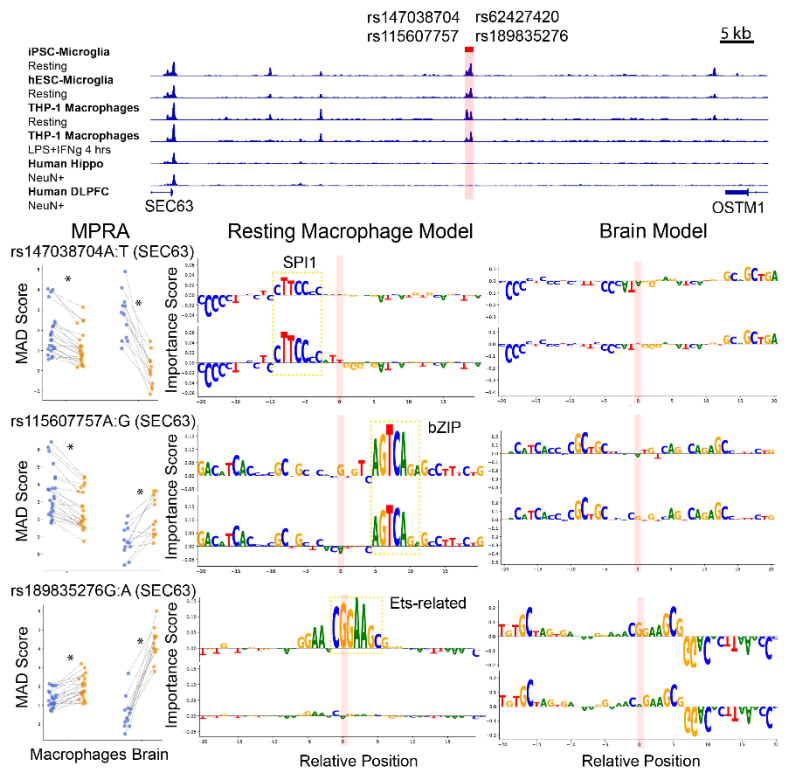

e

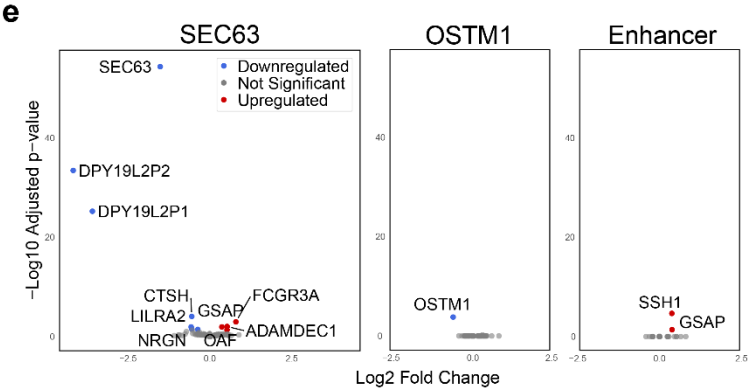

f

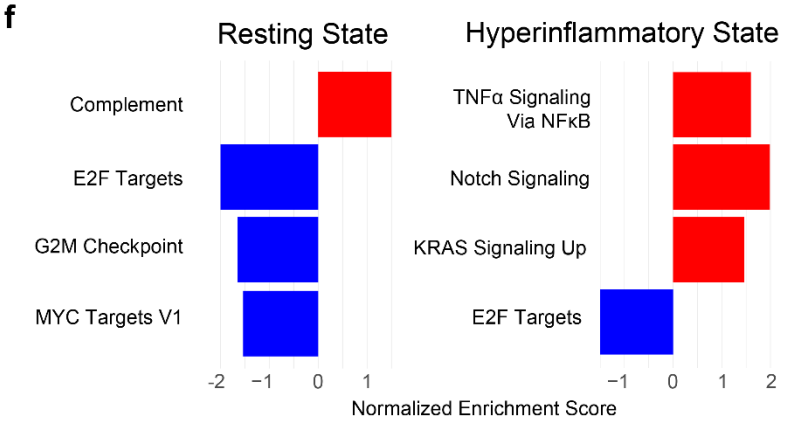

Fig. 6 | Mechanistic interpretation of causal variants at *BIN1*, *MS4A*, and *SEC63-OSTM1* loci.

(a) Selected functionally causal variants at *BIN1*, *MS4A,* and *SEC63-OSTM1* loci and their regulatory effects across cell types. Cells are colored only when the allelic effect is significant within a significantly active enhancer (MPRAnalyze, FDR < 0.05, |P.MAD| > 0.1): red indicates reduced transcription from the minor allele, green indicates increased transcription. Uncolored cells reflect significant allelic effects observed in enhancers that do not meet the activity threshold.

(b) *BIN1* locus. Four microglia-active variants cluster in two adjacent enhancers. In enhancer 1, rs6733839 is predicted to strengthen an SPI1 site in immune cells or create an MEF2 site in neurons, yet the minor allele T represses transcription in THP-1 macrophage MPRA, implying SPI1-induced silencing in THP-1 macrophages. Enhancer 2 contains rs13025765 and rs13025717: rs13025765 flips direction between THP-1 macrophage (repression) and brain tissue (activation), reflecting SPIB- versus RFX-driven regulation, whereas rs13025717 disrupts a SP/KLF motif, lowering both transcription and predicted chromatin accessibility in THP-1 macrophages.

(c) *MS4A6E* intron. An enhancer harbors three functional variants. The minor T allele of rs10897049 strengthens an ETS motif and elevates transcription in macrophages. Conversely, in brain tissue, rs4477457-A disrupts an E2F motif, lowering activity, while rs10792265-G creates an RFX site that likely competes with E2F, further repressing expression. In THP-1 macrophages, these two alleles increased transcription activity, but models did not reveal TF motif differences.

(d) *SEC63/OSTM1* enhancer. Four rare variants produced distinct MPRA readouts. The minor A allele of rs147038704 strengthens an SPI1 motif in THP-1 macrophages yet suppresses transcription in both THP-1 macrophages and mouse brain. The minor T allele of rs115607757 weakens a bZIP motif in THP-1 macrophages, lowering transcription in macrophages but elevating it in the brain. The minor C allele of rs189835276 disrupts an ETS-related motif and consistently increases transcription in both cell types.

(e) CRISPR interference experiments highlight the functional enhancer from panel d. Targeting this enhancer with dCas9-KRAB in resting THP-1 macrophages leaves *SEC63* and *OSTM1* transcripts unchanged yet significantly up-regulates *GSAP* and *SSH1* (DESeq2, adj. P < 0.05). In contrast, silencing the *SEC63* promoter provokes a broader secondary response, also elevating *GSAP*.

(f) Pathway enrichment of the CRISPRi RNA-seq data (fGSEA, FDR < 0.05) reveals state-specific effects of enhancer silencing: in the resting state, it elevates complement signaling and suppresses proliferative programs (E2F, G2M checkpoint, MYC), whereas under LPS+IFN-γ stimulation, it strengthens TNFα–NF–κB, Notch, and KRAS-up signatures and further represses E2F targets.

Asterisks in panels b-d denote variants whose allelic MPRA comparison is significant at FDR < 0.05.

Brain model prediction represents the averaged SHAP values from cortex and striatum models.

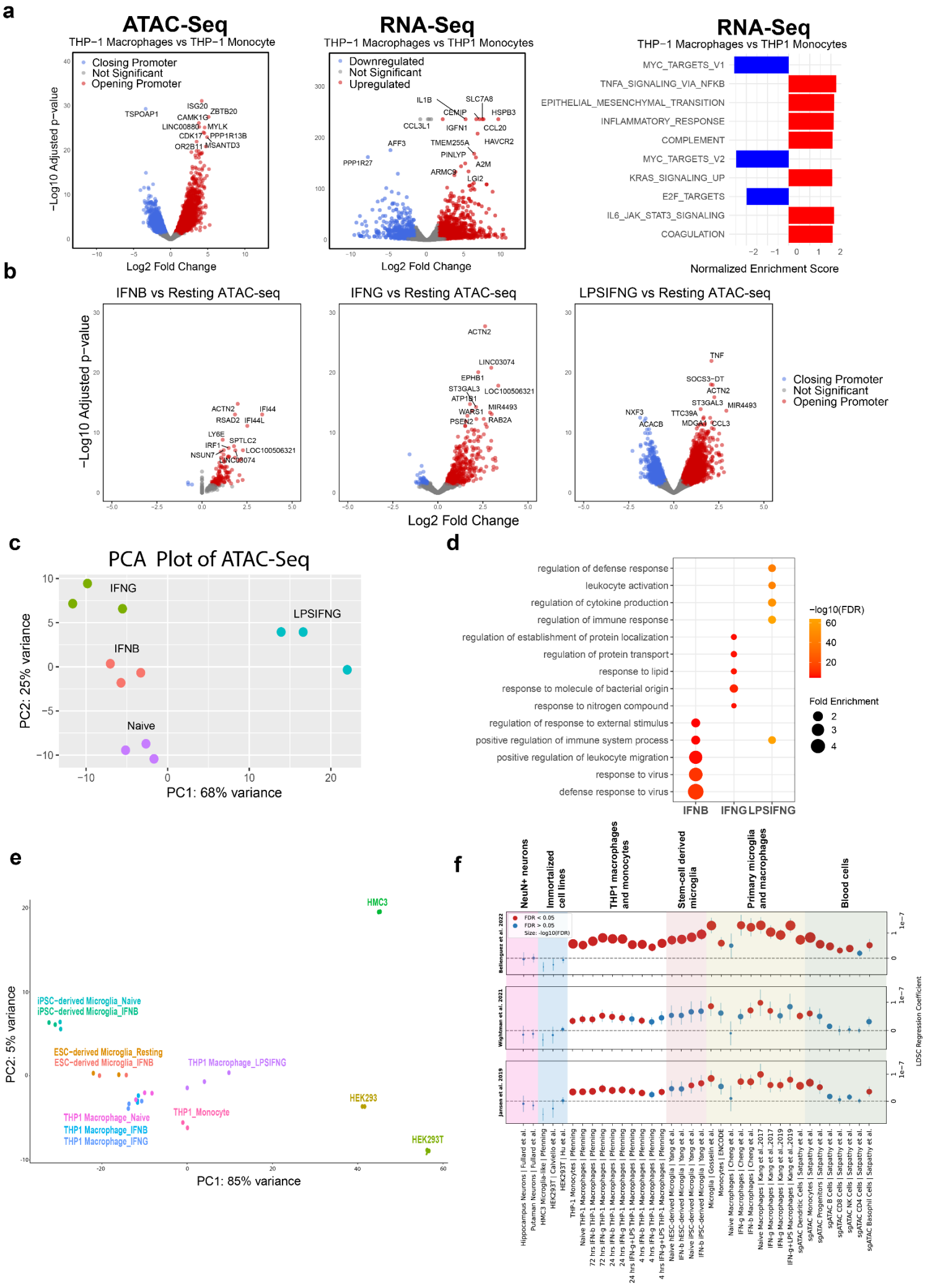
a
ATAC-Seq
THP−1 Macrophages vs THP−1 Monocyte
Closing Promoter
Not Significant
Opening Promoter
−Log10 Adjusted p−value
Log2 Fold Change
RNA-Seq
THP−1 Macrophages vs THP1 Monocytes
Downregulated
Not Significant
Upregulated
Log2 Fold Change
RNA-Seq
THP−1 Macrophages vs THP1 Monocytes
MYC_TARGETS_V1
TNFA_SIGNALING_VIA_NFKB
EPITHELIAL_MESENCHYMAL_TRANSITION
INFLAMMATORY_RESPONSE
COMPLEMENT
MYC_TARGETS_V2
KRAS_SIGNALING_UP
E2F_TARGETS
IL6_JAK_STAT3_SIGNALING
COAGULATION
Normalized Enrichment Score
b
IFNB vs Resting ATAC-seq
IFNG vs Resting ATAC-seq
LPSIFNG vs Resting ATAC-seq
−Log10 Adjusted p−value
Log2 Fold Change
Closing Promoter
Not Significant
Opening Promoter
c
PCA Plot of ATAC-Seq
IFNG
LPSIFNG
IFNB
Naive
PC2: 25% variance
PC1: 68% variance
d
regulation of defense response
leukocyte activation
regulation of cytokine production
regulation of immune response
regulation of establishment of protein localization
regulation of protein transport
response to lipid
response to molecule of bacterial origin
response to nitrogen compound
regulation of response to external stimulus
positive regulation of immune system process
positive regulation of leukocyte migration
response to virus
defense response to virus
IFNB
IFNG
LPSIFNG
−log10(FDR)
Fold Enrichment
e
HMC3
iPSC−derived Microglia_Naive
iPSC−derived Microglia_IFNB
ESC−derived Microglia_Resting
ESC−derived Microglia_IFNB
THP1 Macrophage_LPSIFNG
HEK293
THP1 Macrophage_Naive
THP1 Macrophage_IFNB
THP1 Macrophage_IFNG
THP1_Monocyte
HEK293T
PC2: 5% variance
PC1: 85% variance
f
NeuN+ neurons
Immortalized cell lines
THP1 macrophages and monocytes
Stem-cell derived microglia
Primary microglia and macrophages
Blood cells
FDR < 0.05
FDR > 0.05
Size: -log10(FDR)
Bellenguez et al. 2022
Wightman et al. 2021
Jansen et al. 2019
LDSC Regression Coefficient
Hippocampus Neurons | Fullard et al.
Putaman Neurons | Fullard et al.
HMC3 Microglia-like | Pfenning
HEK293T | Calvello et al.
HEK293T | Hu et al.
THP-1 Monocytes | Pfenning
Naive THP-1 Macrophages | Pfenning
72 hrs IFN-b THP-1 Macrophages | Pfenning
72 hrs IFN-g THP-1 Macrophages | Pfenning
24 hrs IFN-b THP-1 Macrophages | Pfenning
24 hrs IFN-g THP-1 Macrophages | Pfenning
24 hrs IFN-g+LPS THP-1 Macrophages | Pfenning
4 hrs IFN-b THP-1 Macrophages | Pfenning
4 hrs IFN-g THP-1 Macrophages | Pfenning
4 hrs IFN-g+LPS THP-1 Macrophages | Pfenning
Naive hESC-derived Microglia | Yang et al.
IFN-b hESC-derived Microglia | Yang et al.
Naive iPSC-derived Microglia | Yang et al.
IFN-b iPSC-derived Microglia | Yang et al.
Microglia | Gosselin et al.
Monocytes | ENCODE
Naive Macrophages | Cheng et al.
IFN-g Macrophages | Cheng et al.
IFN-b Macrophages | Cheng et al.
Naive Macrophages | Kang et al.,2017
IFN-g Macrophages | Kang et al.,2017
IFN-g Macrophages | Kang et al.,2019
IFN-g+LPS Macrophages | Kang et al.,2019
sgATAC Dendritic Cells | Satpathy et al.
sgATAC Monocytes | Satpathy et al.
sgATAC Progenitors | Satpathy et al.
sgATAC B Cells | Satpathy et al.
sgATAC CD8 Cells | Satpathy et al.
sgATAC NK Cells | Satpathy et al.
sgATAC CD4 Cells | Satpathy et al.
sgATAC Basophil Cells | Satpathy et al.

Extended Data Fig. 1 | Epigenomic characterization of stimulated THP-1 macrophages as a microglial model.

(a) Differentiation of THP-1 monocytes into macrophages, confirmed by reduced cell cycle-related pathways and elevated immune response pathways in ATAC-seq and RNA-seq(FDR < 0.05, DESeq2, fast gene set enrichment analysis).

(b) ATAC-seq of THP-1 macrophages stimulated with IFN-β, IFN-γ, or LPS+IFN-γ shows distinct regulatory responses, including promoter opening and closing (padj < 0.05, DESeq2).

(c) Principal component analysis (PCA) of open chromatin profiles of THP-1 macrophages stimulated with IFN-β, IFN-γ, or LPS+IFN-γ.

(d) Pathway analyses of promoters with gained accessibility under each stimulation highlight antiviral (IFN-β) and M1 polarization pathways (IFN-γ) and defense responses (LPS+IFN-γ) (FDR < 0.05, fast gene set enrichment analysis).

(e) Stratified LD-score regression (S-LDSC) reveals significant enrichment of LOAD risk variants in chromatin accessible in THP-1 macrophages, comparable to primary or hESC/iPSC-derived microglia, but not in neurons or HMC3/HEK293T cells.

(f) PCA of open chromatin profiles confirms that THP-1 macrophages resemble iPSC/hESC-derived microglia, whereas HMC3 is closer to immortalized cell lines. These findings validate THP-1 macrophages as a practical model for dissecting LOAD-associated immune mechanisms.

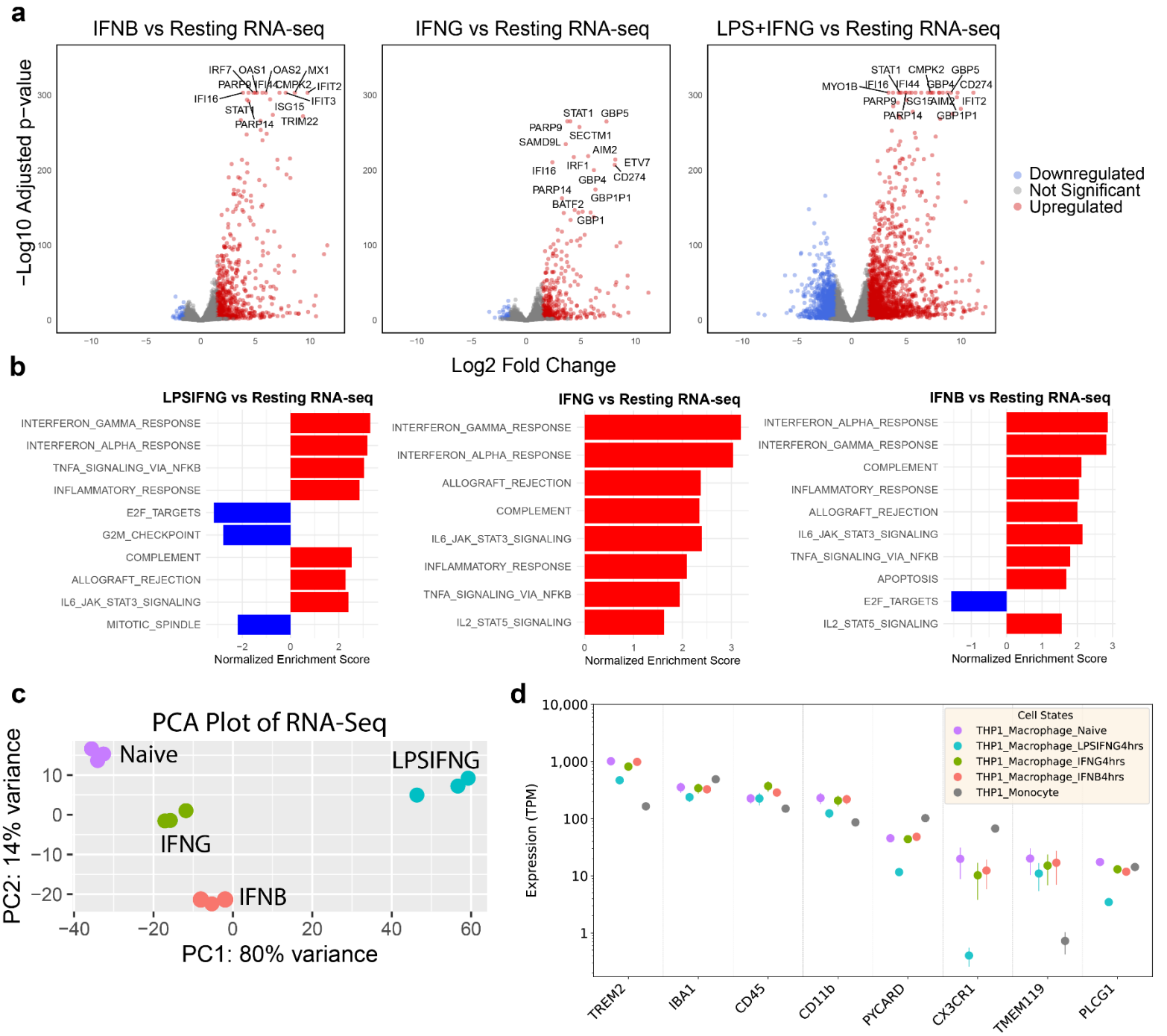
a
IFNB vs Resting RNA-seq
IFNG vs Resting RNA-seq
LPS+IFNG vs Resting RNA-seq
−Log10 Adjusted p−value
Log2 Fold Change
Downregulated
Not Significant
Upregulated
b
LPSIFNG vs Resting RNA-seq
IFNG vs Resting RNA-seq
IFNB vs Resting RNA-seq
INTERFERON_GAMMA_RESPONSE
INTERFERON_ALPHA_RESPONSE
TNFA_SIGNALING_VIA_NFKB
INFLAMMATORY_RESPONSE
E2F_TARGETS
G2M_CHECKPOINT
COMPLEMENT
ALLOGRAFT_REJECTION
IL6_JAK_STAT3_SIGNALING
MITOTIC_SPINDLE
IL2_STAT5_SIGNALING
APOPTOSIS
Normalized Enrichment Score
c
PCA Plot of RNA-Seq
Naive
LPSIFNG
IFNG
IFNB
PC2: 14% variance
PC1: 80% variance
d
Cell States
THP1_Macrophage_Naive
THP1_Macrophage_LPSIFNG4hrs
THP1_Macrophage_IFNG4hrs
THP1_Macrophage_IFNB4hrs
THP1_Monocyte
Expression (TPM)
TREM2
IBA1
CD45
CD11b
PYCARD
CX3CR1
TMEM119
PLCG1
e
Treatment
IFNβ
IFNγ
LPSIFNγ
log2(Activated/Resting)
MG0
MG1
MG2
MG3
MG4
MG5
MG6
MG7
MG8
MG10
MG11
MG12
Homeostatic
Neuronal Surveillance
Inflammatory I
Ribosome Biogenesis
Lipid Processing
Phagocytic
Stress Signature
Glycolytic
Inflammatory II
Inflammatory III
Antiviral
Cycling
f
THP-1 Macrophages
Amyloid fibril-treated iPSC-MG
Pearson' r
THP-1 LPSIFNg 4hrs
THP-1 Resting
THP-1 IFNb 4hrs
THP-1 IFNg 4 hrs
iPSC-MG Amyloid fibril 24 hrs
iPSC-MG Amyloid fibril 96 hrs
iPSC-MG Amyloid fibril 4 hrs
iPSC-MG Resting

Extended Data Fig. 2 | Transcriptomic profiling and microglial marker validation in THP-1 macrophages.

(a) Differential expression analyses confirm significant up- or downregulated genes under various stimulation conditions (FDR < 0.05, DESeq2).

(b) Gene set enrichment analyses of resting and stimulated THP-1 macrophages reveal immune-related shifts (IFN-β, IFN-γ, LPS+IFN-γ) that mirror ATAC-seq changes in Extended Data Fig. 1. (FDR < 0.05, fast gene set enrichment analysis).

(c) PCA of RNA-seq data shows distinct transcriptomic clusters for each state, reflecting diverse immune states.

(d) Microglial and macrophage markers were expressed in all conditions.

(e) Differential expression of microglial-state marker genes (Sun et al.[25]) in stimulated THP-1 macrophages versus non-marker genes (two-sided Mann-Whitney U, Benjamini-Hochberg correction). Significance codes, Benjamini-Hochberg FDR: **** < 1×10^{-4}; *** < 1×10^{-3}; ** < 1×10^{-2}; * < 0.05; NS, not significant.

(f) Transcriptomic concordance between LPS + IFN-γ-stimulated THP-1 macrophages and amyloid-fibril-treated iPSC-microglia. Pearson's *r* is calculated on the expression levels of genes that are differentially expressed in the amyloid-fibril model (Sun et al.[25]).

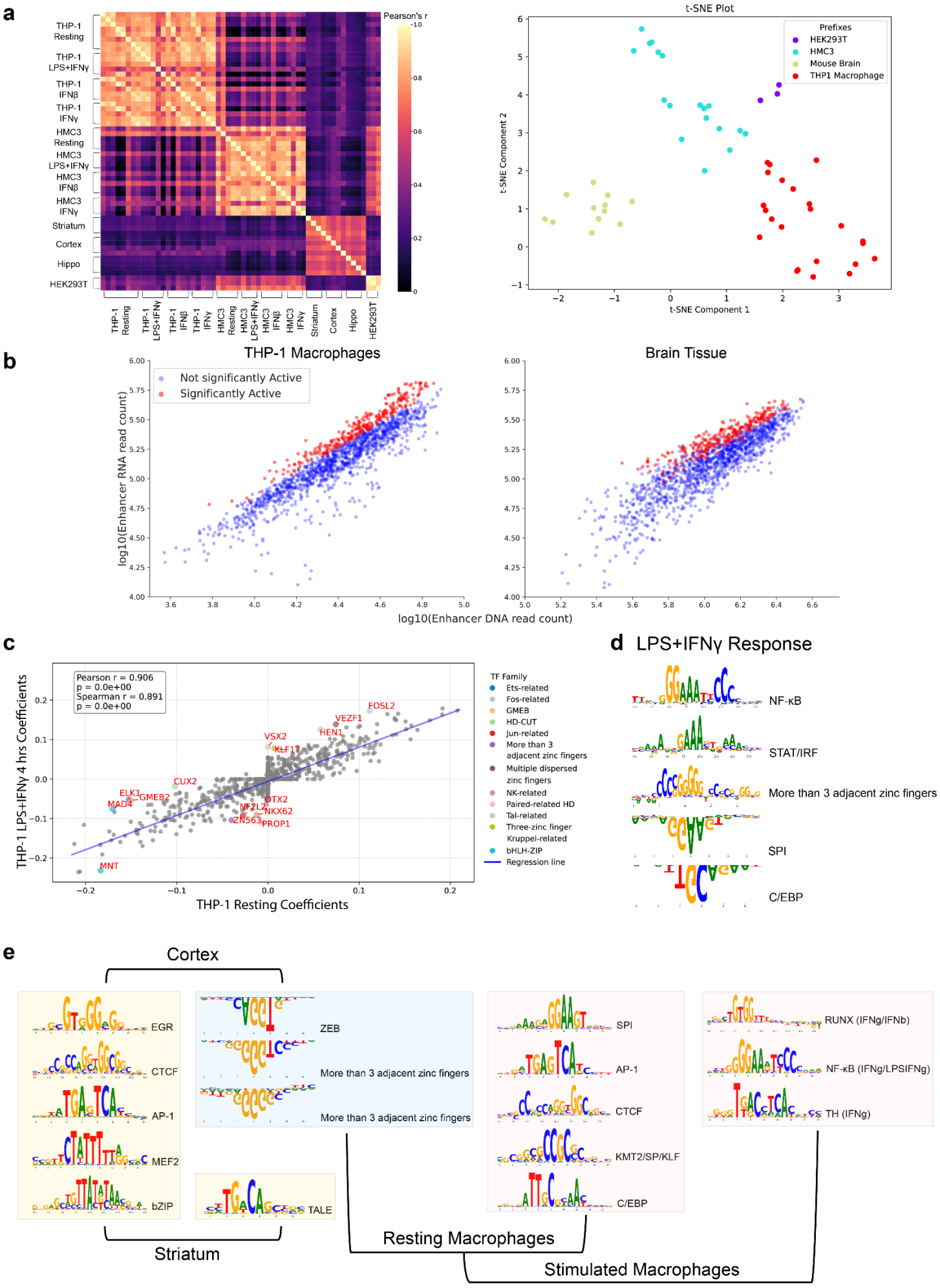
a
Pearson's r
THP-1 Resting
THP-1 LPS+IFNγ
THP-1 IFNβ
THP-1 IFNγ
HMC3 Resting
HMC3 LPS+IFNγ
HMC3 IFNβ
HMC3 IFNγ
Striatum
Cortex
Hippo
HEK293T
t-SNE Plot
Prefixes
HEK293T
HMC3
Mouse Brain
THP1 Macrophage
t-SNE Component 1
t-SNE Component 2
b
THP-1 Macrophages
Brain Tissue
Not significantly Active
Significantly Active
log10(Enhancer RNA read count)
log10(Enhancer DNA read count)
c
Pearson r = 0.906
p = 0.0e+00
Spearman r = 0.891
p = 0.0e+00
THP-1 LPS+IFNγ 4 hrs Coefficients
THP-1 Resting Coefficients
FOSL2
VEZF1
HEN1
VSX2
KLF17
CUX2
ELK1
GMEB2
MAD4
OTX2
NF2L2
NKX62
ZN563
PROP1
MNT
TF Family
Ets-related
Fos-related
GMEB
HD-CUT
Jun-related
More than 3 adjacent zinc fingers
Multiple dispersed zinc fingers
NK-related
Paired-related HD
Tal-related
Three-zinc finger Kruppel-related
bHLH-ZIP
Regression line
d LPS+IFNγ Response
NF-κB
STAT/IRF
More than 3 adjacent zinc fingers
SPI
C/EBP
e
Cortex
EGR
CTCF
AP-1
MEF2
bZIP
ZEB
More than 3 adjacent zinc fingers
More than 3 adjacent zinc fingers
TALE
SPI
AP-1
CTCF
KMT2/SP/KLF
C/EBP
RUNX (IFNg/IFNb)
NF-κB (IFNg/LPSIFNg)
TH (IFNg)
Striatum
Resting Macrophages
Stimulated Macrophages

Extended Data Fig. 3 | MPRA reproducibility, cell-type clustering, and motif contributions to LPS+IFN-γ-responsive enhancers.

(a) Biological replicates show high concordance in MPRA activity (Pearson's r ≈ 0.8-0.9 *in vitro*, r ≈ 0.6-0.7). t-SNE analysis of CRE enhancer activities reveals distinct clustering by cell type.

(b) Approximately 12.5% of the tested candidate cis-regulatory elements (CREs) are active (MPRAnalyze quantitative analysis, P.MAD.Score < 0.1) in both macrophages and mouse brain regions.

(c) Coefficients of HOCOMOCO transcription factor motifs in elastic net models that predict MAD scores of LPS+IFN-γ-treated THP-1 macrophages and resting THP-1 macrophages. Regression outliers highlighted in red have residuals greater than 3-fold the standard deviation.

(d) Deep-learning models trained on LPS+IFN-γ responsive ATAC-seq peaks (DESeq2, padj < 0.05) identify TF motifs positively and negatively enriched among LPS+IFN-γ responsive MPRA enhancers. NF-κB, IRF/STAT, and CG-rich motifs contribute to increased accessibility, whereas SPI1 and C/EBP motifs correlate with decreased accessibility (TF-MoDISco, motif q-value < 0.05).

(e) Deep-learning models trained on ATAC-seq data identify cell-type-specific TF motifs enriched among active MPRA enhancers, confirming motif-driven transcriptional regulation (TF-MoDISco, motif q-value < 0.05).

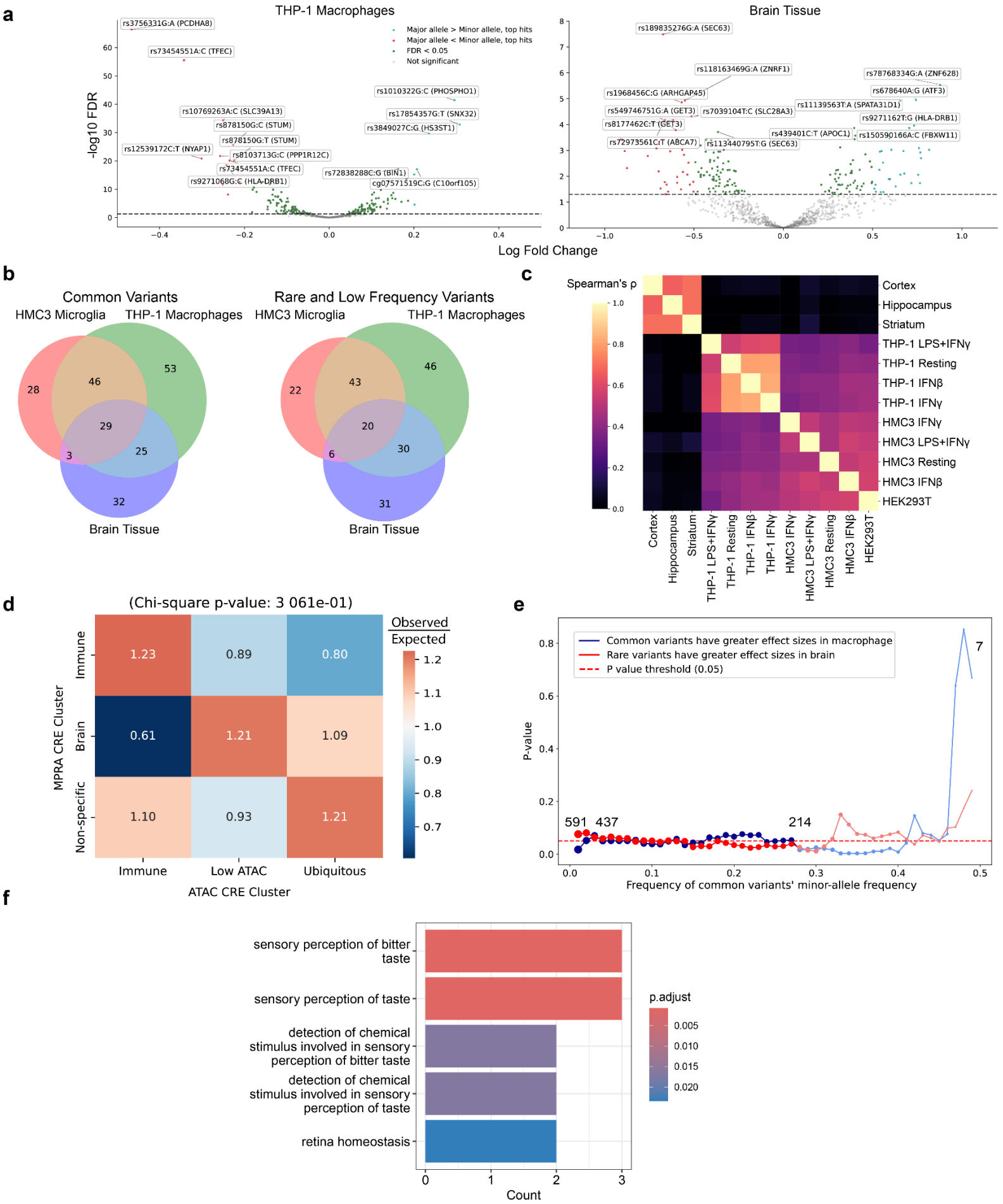
a
THP-1 Macrophages
Brain Tissue
Major allele > Minor allele, top hits
Major allele < Minor allele, top hits
FDR < 0.05
Not significant
-log10 FDR
Log Fold Change
rs3756331G:A (PCDHA8)
rs73454551A:C (TFEC)
rs1010322G:C (PHOSPHO1)
rs10769263A:C (SLC39A13)
rs878150G:C (STUM)
rs17854357G:T (SNX32)
rs3849027C:G (HS3ST1)
rs878150G:T (STUM)
rs12539172C:T (NYAP1)
rs8103713G:C (PPP1R12C)
rs73454551A:C (TFEC)
rs72838288C:G (BIN1)
rs9271068G:C (HLA-DRB1)
cg07571519C:G (C10orf105)
rs189835276G:A (SEC63)
rs118163469G:A (ZNRF1)
rs78768334G:A (ZNF628)
rs1968456C:G (ARHGAP45)
rs678640A:G (ATF3)
rs11139563T:A (SPATA31D1)
rs549746751G:A (GET3)
rs7039104T:C (SLC28A3)
rs8177462C:T (GET3)
rs92711162T:G (HLA-DRB1)
rs439401C:T (APOC1)
rs150590166A:C (FBXW11)
rs72973561C:T (ABCA7)
rs113440795T:G (SEC63)
b
Common Variants
HMC3 Microglia
THP-1 Macrophages
Brain Tissue
28
46
53
29
3
25
32
Rare and Low Frequency Variants
HMC3 Microglia
THP-1 Macrophages
Brain Tissue
22
43
46
20
6
30
31
c
Spearman's ρ
Cortex
Hippocampus
Striatum
THP-1 LPS+IFNγ
THP-1 Resting
THP-1 IFNβ
THP-1 IFNγ
HMC3 IFNγ
HMC3 LPS+IFNγ
HMC3 Resting
HMC3 IFNβ
HEK293T
d
(Chi-square p-value: 3 061e-01)
Observed
Expected
MPRA CRE Cluster
Immune
Brain
Non-specific
ATAC CRE Cluster
Immune
Low ATAC
Ubiquitous
1.23
0.89
0.80
0.61
1.21
1.09
1.10
0.93
1.21
e
Common variants have greater effect sizes in macrophage
Rare variants have greater effect sizes in brain
P value threshold (0.05)
P-value
Frequency of common variants' minor-allele frequency
591
437
214
7
f
sensory perception of bitter taste
sensory perception of taste
detection of chemical stimulus involved in sensory perception of bitter taste
detection of chemical stimulus involved in sensory perception of taste
retina homeostasis
Count
p.adjust
0.005
0.010
0.015
0.020

Extended Data Fig. 4 | Context-dependent functional impacts of LOAD-associated genetic variants.

(a) Volcano plots of significantly functional common and rare LOAD variants identified by MPRA in THP-1 macrophages and mouse brain tissue (MPRAnalyze comparative analysis, FDR < 0.05). Variants highlight cell-type specificity and effect-size distributions of regulatory effects.

(b) Venn diagram illustrating overlaps of functional LOAD variants identified across THP-1 macrophages, HMC3 microglia, and mouse brain.

(c) Variant effects quantified by MPRA reveal cell-type-specific impacts. Spearman correlation coefficients (P < 0.05) are higher between similar cell types and lower between distinct cell types, emphasizing cell-type specificity.

(d) Variants show a visible trend of segregating into immune-, brain-, or nonspecific categories consistent with their CRE annotations, but this distribution does not reach statistical significance (Chi-squared test, p > 0.05).

(e) Common versus rare variant effects on transcriptional regulation in MPRA. Rare variants (minor allele frequency [MAF] < 0.01) have stronger effects in brain tissue; common variants (including low frequency variants, MAF ≥ 0.01) exhibit greater effects in THP-1 macrophages. Highly frequent variants (MAF ≥ 0.1) reinforce this pattern, highlighting distinct roles for rare versus common LOAD variants. Each dot represents an independent one-tailed Mann-Whitney U test; y-axis indicates the test P-value. Dot size represents the ratio of common to rare variants, and the number of common variants at critical points is displayed. Dark blue/red: more common than rare variants (rare MAF ≤ 0.2); light blue/red: fewer common than rare variants (rare MAF > 0.2).

(f) Genes regulated by distal enhancers that contain functionally causal variants are enriched in sensory-related pathways (fGSEA, FDR < 0.05).

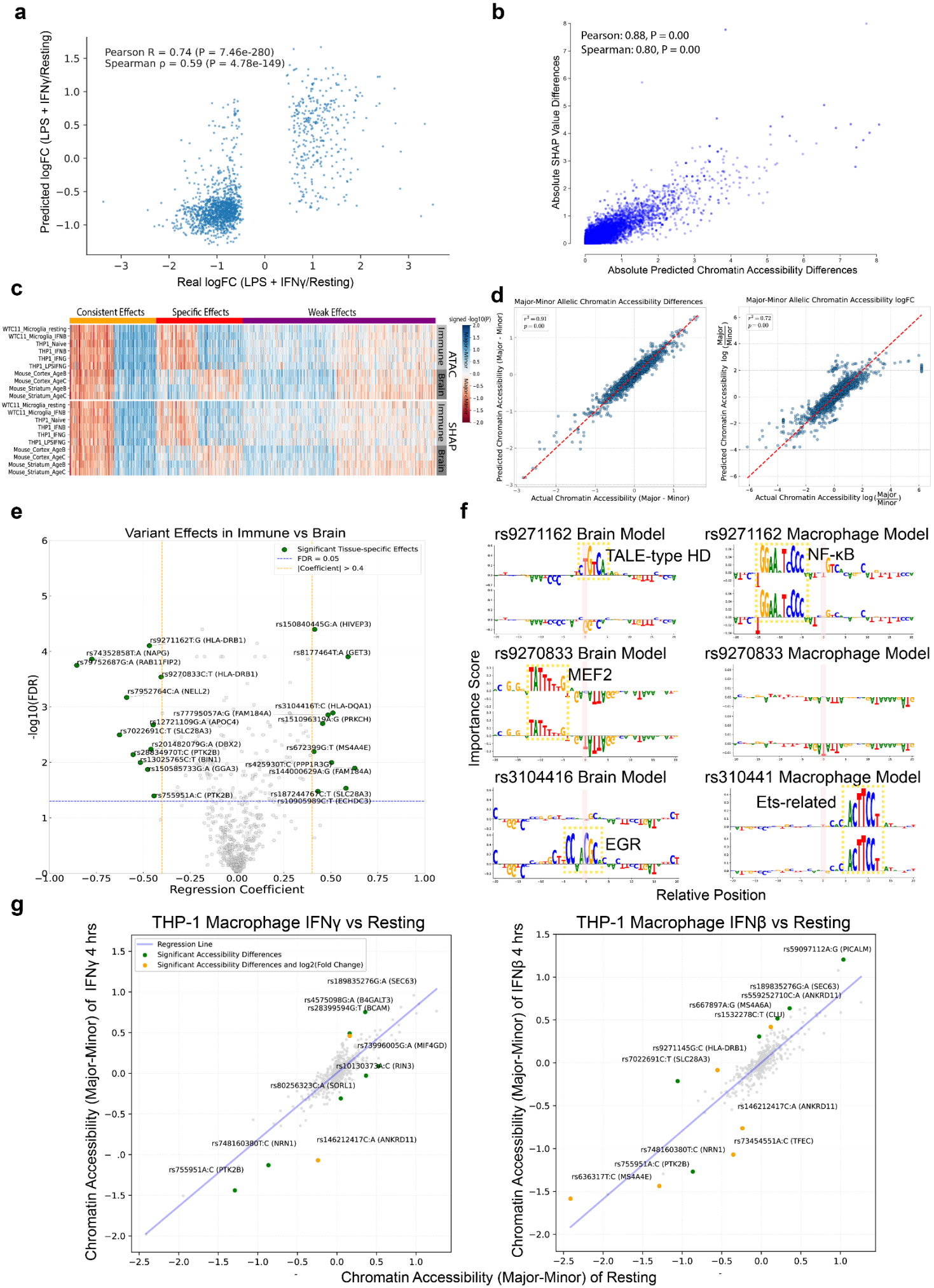
a
Pearson R = 0.74 (P = 7.46e-280)
Spearman ρ = 0.59 (P = 4.78e-149)
Predicted logFC (LPS + IFNγ/Resting)
Real logFC (LPS + IFNγ/Resting)
b
Pearson: 0.88, P = 0.00
Spearman: 0.80, P = 0.00
Absolute SHAP Value Differences
Absolute Predicted Chromatin Accessibility Differences
c
Consistent Effects
Specific Effects
Weak Effects
signed -log10(P)
Immune
Brain
ATAC
SHAP
d
Major-Minor Allelic Chromatin Accessibility Differences
Predicted Chromatin Accessibility (Major - Minor)
Actual Chromatin Accessibility (Major - Minor)
Major-Minor Allelic Chromatin Accessibility logFC
e
Variant Effects in Immune vs Brain
Significant Tissue-specific Effects
FDR = 0.05
|Coefficient| > 0.4
-log10(FDR)
Regression Coefficient
rs150840445G:A (HIVEP3)
rs9271162T:G (HLA-DRB1)
rs74352858T:A (NAPG)
rs8177464T:A (GET3)
rs79752687G:A (RAB11FIP2)
rs9270833C:T (HLA-DRB1)
rs7952764C:A (NELL2)
rs3104416T:C (HLA-DQA1)
rs77795057A:G (FAM184A)
rs12721109G:A (APOC4)
rs151096319A:G (PRKCH)
rs7022691C:T (SLC28A3)
rs201482079G:A (DBX2)
rs672399G:T (MS4A4E)
rs28034970T:C (PTK2B)
rs13025765C:T (BIN1)
rs425930T:C (PPP1R3G)
rs150585733G:A (GGA3)
rs144000629A:G (FAM184A)
rs755951A:C (PTK2B)
rs187244767C:T (SLC28A3)
rs10905989C:T (ECHDC3)
f
rs9271162 Brain Model
TALE-type HD
rs9271162 Macrophage Model
NF-κB
rs9270833 Brain Model
MEF2
rs9270833 Macrophage Model
rs3104416 Brain Model
EGR
rs310441 Macrophage Model
Ets-related
Importance Score
Relative Position
g
THP-1 Macrophage IFNγ vs Resting
Regression Line
Significant Accessibility Differences
Significant Accessibility Differences and log2(Fold Change)
rs189835276G:A (SEC63)
rs4575098G:A (B4GALT3)
rs28399594G:T (BCAM)
rs73996005G:A (MIF4GD)
rs10130373A:C (RIN3)
rs80256323C:A (SORL1)
rs748160380T:C (NRN1)
rs146212417C:A (ANKRD11)
rs755951A:C (PTK2B)
Chromatin Accessibility (Major-Minor) of IFNγ 4 hrs
Chromatin Accessibility (Major-Minor) of Resting
THP-1 Macrophage IFNβ vs Resting
rs59097112A:G (PICALM)
rs189835276G:A (SEC63)
rs559252710C:A (ANKRD11)
rs667897A:G (MS4A6A)
rs1532278C:T (CLU)
rs9271145G:C (HLA-DRB1)
rs7022691C:T (SLC28A3)
rs146212417C:A (ANKRD11)
rs73454551A:C (TFEC)
rs748160380T:C (NRN1)
rs755951A:C (PTK2B)
rs636317T:C (MS4A4E)
Chromatin Accessibility (Major-Minor) of IFNβ 4 hrs

Extended Data Fig. 5 | Machine-learning models identify cell-type- and immune-state-specific variant effects.

(a) Convolutional neural network (CNN) models trained on LPS+IFN-γ-responsive peaks (differentially accessible regions in ATAC-seq, DEseq2, FDR < 0.05) in THP-1 macrophages. The model showed good performance on the validation dataset (Pearson's r, 0.74).

(b) Model-derived accessibility changes significantly correlate with SHAP importance scores (Pearson's r, 0.88), validating the approach for identifying regulatory variants.

(c) *In silico* mutagenesis reveals allelic effects of LOAD variants, including consistent, specific, and weak effects. P-values calculated based on differences in predicted chromatin accessibility and SHAP values between major and minor alleles relative to cell-type-specific null distributions.

(d,e) Linear regression across multiple machine learning predictions of chromatin accessibility differences and log fold changes captures immune-versus neuronal-specific variant effects.

(f) Examples of variants in *HLA-DRB1* and *HLA-DQA1* show unexpectedly strong neuronal effects (SHAP values visualized by logomaker).

(g) Independent linear regressions of model-predicted effect sizes across two immune states (resting, IFN-γ, IFN-β) show variants with state-specific activity. Variants whose standardized residuals exceed 3-fold standard deviation (two-tailed P < 0.01) are classified as IFN-γ-specific, IFN-β-specific, or brain-region-specific.

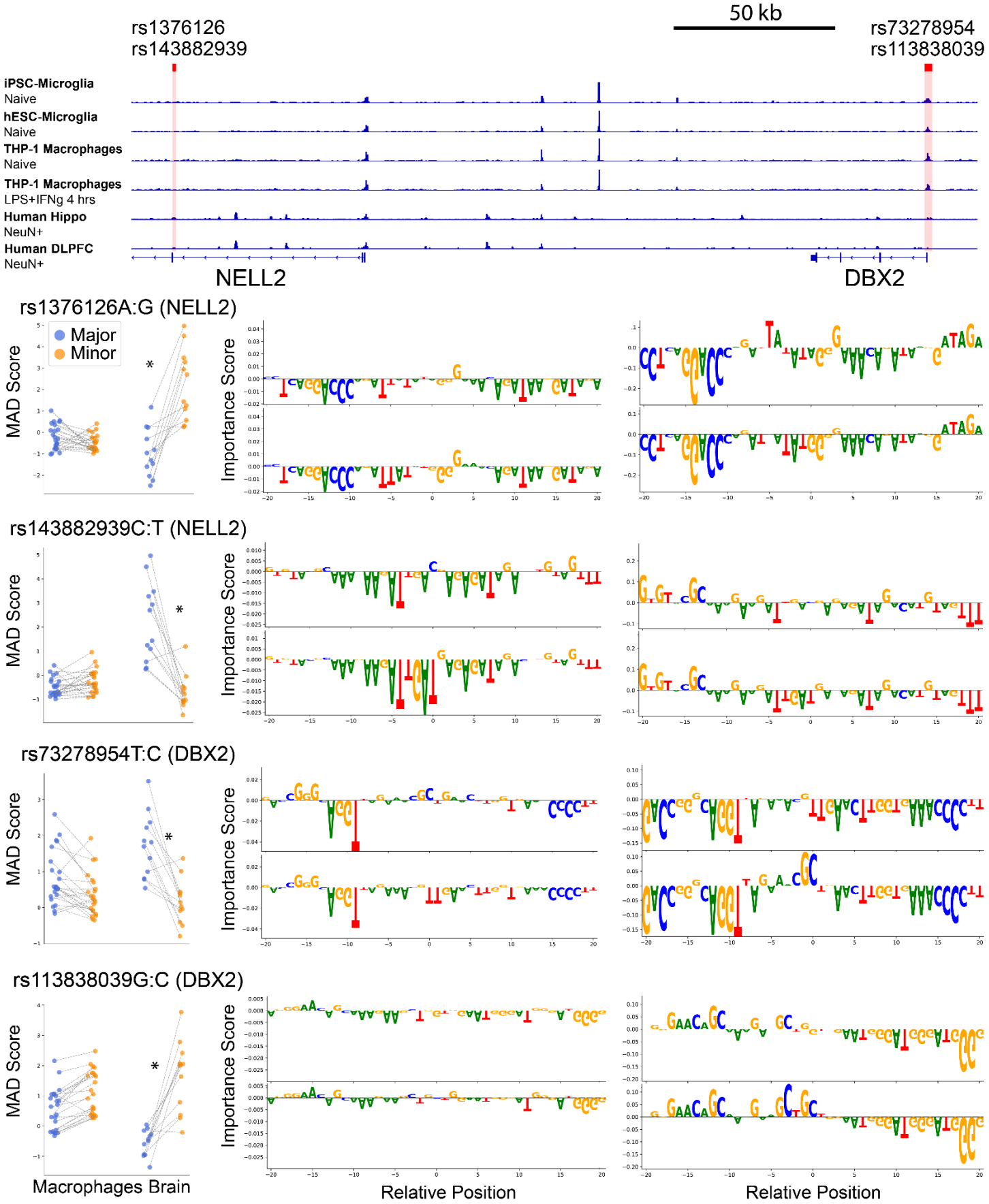
50 kb
rs1376126
rs143882939
rs73278954
rs113838039
iPSC-Microglia
Naive
hESC-Microglia
Naive
THP-1 Macrophages
Naive
THP-1 Macrophages
LPS+IFNg 4 hrs
Human Hippo
NeuN+
Human DLPFC
NeuN+
NELL2
DBX2
rs1376126A:G (NELL2)
rs143882939C:T (NELL2)
rs73278954T:C (DBX2)
rs113838039G:C (DBX2)
Major
Minor
MAD Score
Importance Score
Macrophages Brain
Relative Position
Relative Position

Extended Data Fig. 6 | Rare variants in *NELL2* and *DBX2* highlight neuronal-specific regulatory outcomes. Two rare variants in the *NELL2* locus (rs1376126, rs143882939) display no significant effect in THP-1 macrophages but show contrasting allelic activity in mouse hippocampus, cortex, and striatum, demonstrating neuronal-context specificity (*FDR<0.05, MPRAnalyze comparative analysis). Machine learning models do not capture motifs that positively contribute to chromatin accessibility (SHAP scores by TF-MoDISco). Nearby variants in the *DBX2* promoter (rs73278954, rs113838039) have measurable effects in both macrophages and brain tissue. Collectively, these findings emphasize how rare LOAD variants can selectively affect neuronal enhancers while also exerting cross-cell-type regulatory functions in certain contexts.

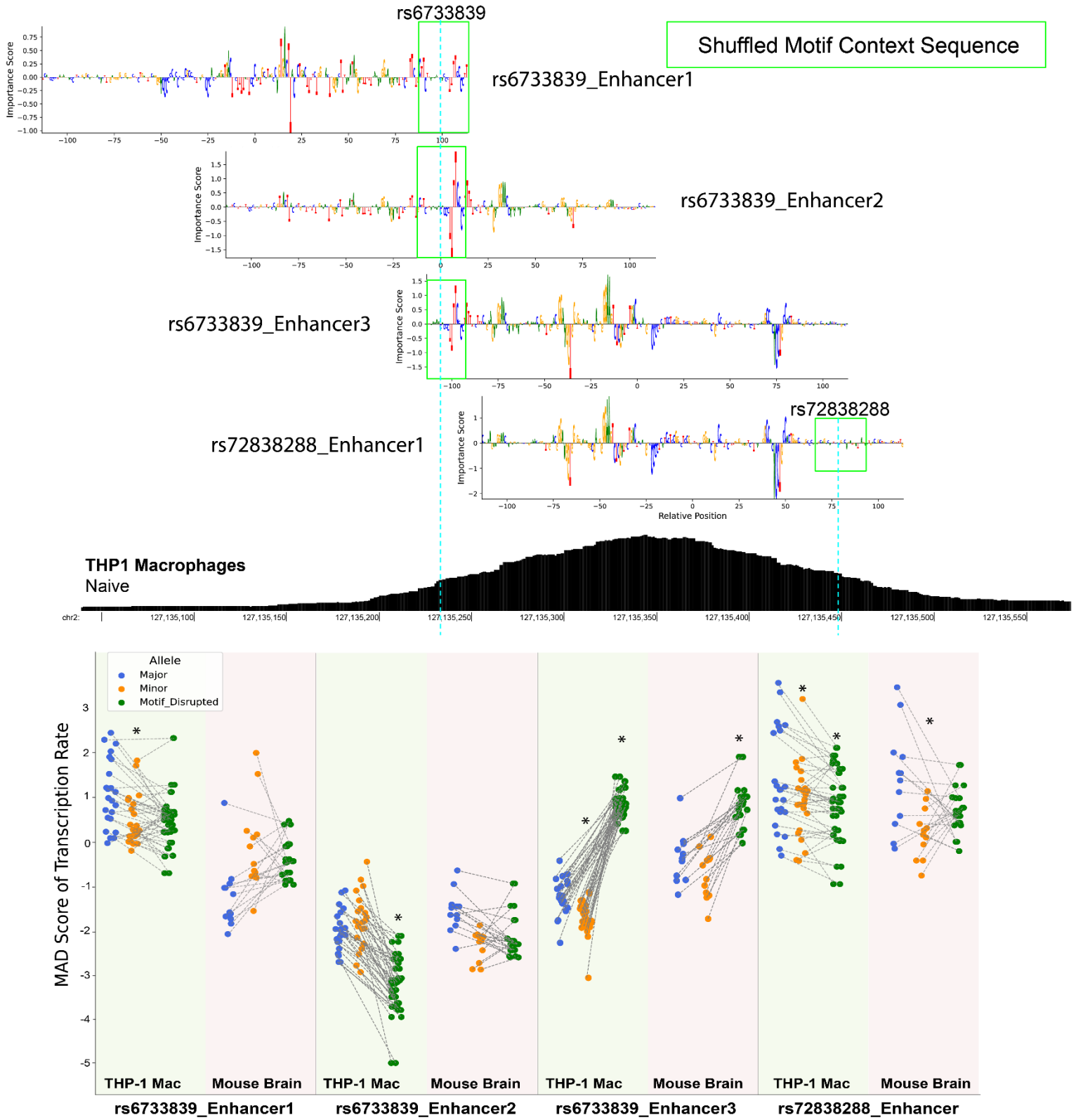
rs6733839
Shuffled Motif Context Sequence
rs6733839_Enhancer1
rs6733839_Enhancer2
rs6733839_Enhancer3
rs72838288_Enhancer1
rs72838288
Importance Score
Relative Position
THP1 Macrophages
Naive
chr2:
127,135,100
127,135,150
127,135,200
127,135,250
127,135,300
127,135,350
127,135,400
127,135,450
127,135,500
127,135,550
Allele
Major
Minor
Motif_Disrupted
MAD Score of Transcription Rate
THP-1 Mac
Mouse Brain
rs6733839_Enhancer1
rs6733839_Enhancer2
rs6733839_Enhancer3
rs72838288_Enhancer

Extended Data Fig. 7 | Synthetic enhancer tiling and motif shuffling for *BIN1* in THP-1 macrophage MPRA.

Synthetic enhancer tiling and 25 bp motif shuffling around rs6733839 at the *BIN1* locus illustrate how combinatorial interactions determine whether the motif context around exerts an activating or repressive effect. MAD scores quantify transcriptional activity (MPRAnalyze quantitative analysis), and motif-allele differences are evaluated by MPRAnalyze comparative analyses, respectively (*FDR<0.05, MPRAnalyze comparative analysis). When the motif context pairs only with upstream motifs (Enhancer_1), the CRE behaves as an enhancer. When paired with both upstream and downstream motifs (Enhancer_2), it is embedded in a repressive CRE but still confers partial activation. When paired only with downstream motifs (Enhancer_3), it acts repressively within a repressive CRE. Removing the rs6733839 motif context while retaining downstream motifs (Enhancer_4) produces a net activating enhancer. These observations suggest that the rs6733839 motif context provides a repressive function in combination with downstream motifs but becomes activating when upstream motifs are present, with the net effect ultimately dominated by its combination with downstream sequences.

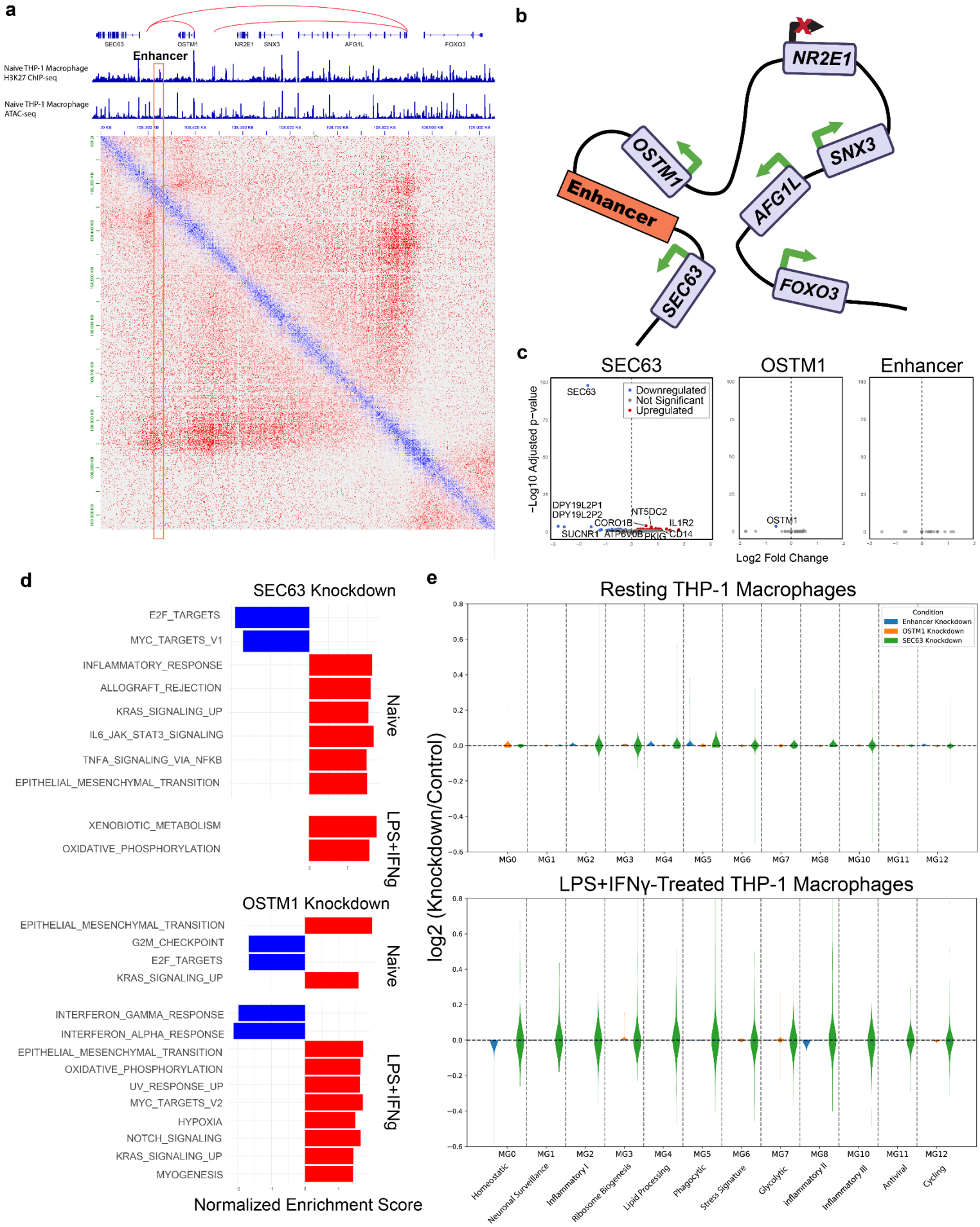
a
SEC63
OSTM1
NR2E1
SNX3
AFG1L
FOXO3
Enhancer
Naive THP-1 Macrophage H3K27 ChIP-seq
Naive THP-1 Macrophage ATAC-seq
b
NR2E1
OSTM1
SNX3
Enhancer
AFG1L
SEC63
FOXO3
c
SEC63
OSTM1
Enhancer
Downregulated
Not Significant
Upregulated
−Log10 Adjusted p−value
Log2 Fold Change
DPY19L2P1
DPY19L2P2
NT5DC2
CORO1B
IL1R2
SUCNR1
ATP6V0B
PKIG
CD14
d
SEC63 Knockdown
E2F_TARGETS
MYC_TARGETS_V1
INFLAMMATORY_RESPONSE
ALLOGRAFT_REJECTION
KRAS_SIGNALING_UP
IL6_JAK_STAT3_SIGNALING
TNFA_SIGNALING_VIA_NFKB
EPITHELIAL_MESENCHYMAL_TRANSITION
XENOBIOTIC_METABOLISM
OXIDATIVE_PHOSPHORYLATION
Naive
LPS+IFNg
OSTM1 Knockdown
EPITHELIAL_MESENCHYMAL_TRANSITION
G2M_CHECKPOINT
E2F_TARGETS
KRAS_SIGNALING_UP
INTERFERON_GAMMA_RESPONSE
INTERFERON_ALPHA_RESPONSE
EPITHELIAL_MESENCHYMAL_TRANSITION
OXIDATIVE_PHOSPHORYLATION
UV_RESPONSE_UP
MYC_TARGETS_V2
HYPOXIA
NOTCH_SIGNALING
KRAS_SIGNALING_UP
MYOGENESIS
Normalized Enrichment Score
e
Resting THP-1 Macrophages
LPS+IFNγ-Treated THP-1 Macrophages
Condition
Enhancer Knockdown
OSTM1 Knockdown
SEC63 Knockdown
log2 (Knockdown/Control)
MG0
MG1
MG2
MG3
MG4
MG5
MG6
MG7
MG8
MG10
MG11
MG12
Homeostatic
Neuronal Surveillance
Inflammatory I
Ribosome Biogenesis
Lipid Processing
Phagocytic
Stress Signature
Glycolytic
Inflammatory II
Inflammatory III
Antiviral
Cycling

Extended Data Fig. 8 | Chromatin architecture and functional consequences of CRISPRi targeting the *SEC63-OSTM1* enhancer.

(a) Hi-C in THP-1 macrophages (<5-kb resolution) places the enhancer (black bar) in the same contact domain as the *SEC63* promoter and shows a looping interaction with the *OSTM1* promoter and a CTCF anchor in the intronic regions of *AFG1L*.

(b) Three-dimensional chromatin model of the *SEC63-OSTM1* enhancer and nearby genes.

(c) *SEC63*, the enhancer, and *OSTM1* knockdown in hyperinflammatory (LPS + IFN-γ-treated) THP-1 macrophages.

(d) CRISPRi knockdown of the *SEC63* and *OSTM1* promoters perturbs distinct transcriptional pathways in resting and hyperinflammatory (LPS + IFN-γ-treated) THP-1 macrophages (fgsea, FDR<0.05).

(e) Expression of the microglial-state marker genes defined by Sun et al.[25] after CRISPRi. Silencing *SEC63* shifts multiple microglial programs, and these shifts are amplified under LPS + IFN-γ-highlighting a central role for *SEC63* in state transitions and immune responses.